AFIT/GE/ENG/97D-09

ATMOSPHERIC INDUCED ERRORS IN SPACE-TIME ADAPTIVE PROCESSING

THESIS

Vinod Durgam Naga
Second Lieutentant, USAF

AFIT/GE/ENG/97D-09

Approved for public release; distribution unlimited

The views expressed in this thesis are those of the author and do not reflect the official policy or position of the Department of Defense or the United States Government.

AFIT/GE/ENG/97D-09

ATMOSPHERIC INDUCED ERRORS IN SPACE-TIME ADAPTIVE PROCESSING

THESIS

Presented to the Faculty of the School of Engineering

of the Air Force Institute of Technology

Air University

In Partial Fulfillment of the

Requirements for the Degree of

Master of Science in Electrical Engineering

Vinod Durgam Naga, B.S.

Second Lieutentant, USAF

December, 1997

AFIT/GE/ENG/97D-09

ATMOSPHERIC INDUCED ERRORS IN SPACE-TIME ADAPTIVE PROCESSING

Vinod Durgam Naga, B.S.

Second Lieutentant, USAF

Approved:

Byron M Welsh	29 Oct 97
Dr. Byron M. Welsh Thesis Advisor	Date
Vittal P. Pyati	29 Oct 97
Dr. Vittal P. Pyati Committee Member	Date
	29 Oct 97
Dr. Robert W. McMillan Committee Member	Date
Michael C. Temple	29 Oct 97
Maj. Michael A. Temple Committee Member	Date
William Larkin Melvin Jr.	29 Oct 97
Capt. William L. Melvin Committee Member	Date

Acknowledgements

I would like to give my thanks to the individuals who helped me complete this thesis effort. I owe a great deal to my thesis advisor, Dr. Byron Welsh. His guidance and perspective kept me on track and his insight into solving some of the problems which I encountered was invaluable. As the situation at AFIT changed, Dr. Welsh made an extended effort to continue to support my research, for that I am very appreciative.

I would also like to thank Dr. Robert McMillan and Captain William Melvin of Rome Labs for their sponsorship of this thesis. The problem concept was theirs and their assistance and advice were crucial parts of my success. My committee members, Dr. Vittal Pyati and Major Michael Temple, are also deserving of my thanks. The hours of consult they lent helped to add to the depth of my analysis and solution.

I also owe my thanks to my family for the support they gave me throughout my academic life. I especially owe a great deal to my parents, Manohar and Lokeshwari Naga. Throughout my life, they have provided to me the opportunities and the tools which have made my accomplishments attainable.

My last thanks go to my good friends Lt Bruce Hunt and Lt Julie Burdelak. Completing the AFIT program has been one of the most challenging tasks I've ever attempted. The friendship, understanding, and support provided by my close friends has made this a more fulfilling and manageable experience.

To all these individuals, please accept my warmest thanks. I hold you all in the highest regard.

Vinod Durgam Naga

Table of Contents

List of Figures

List of Tables

Abstract

Space Time Adaptive Processing (STAP) exhibits a significant capability for nulling interferers such as clutter and jamming. This capability depends on the accuracy of the radar phase received by each of the antenna elements over the coherent processing interval. Atmospheric turbulence introduces phase perturbations on the propagating radar wave over space, and to a lesser degree, time. This thesis examines the effects of atmospheric turbulence-induced phase perturbations on the performance of ground-based STAP systems using Fully Adaptive Joint Domain Optimum and Partially Adaptive Factored-Time Space processing methods.

The magnitude of the turbulent condition may be expressed in terms of the index of refraction structure constant, C_n^2. This parameter is a statistical representation of the strength of the turbulence and typically ranges from 5.0×10^{-17} $m^{-2/3}$ for extremely light turbulence to 5.0×10^{-10} $m^{-2/3}$ for heavy turbulence.

Significant atmospheric turbulence is a near-to-ground phenomenon and is a matter of concern in ground-based array systems. This thesis concentrates on the turbulence effects on STAP applied to ground-based arrays. Since turbulent conditions disappear rapidly with altitude, this thesis further focuses on the capability of STAP to resolve targets at low elevation angles in the presence of turbulence. To focus on the problem of turbulence effects, only clutter interference and receiver noise are considered. Turbulence effects on the EM phase-front are calculated for C_n^2 values ranging from 5.0×10^{-14} $m^{-2/3}$ to 5.0×10^{-10} $m^{-2/3}$ in the S and X frequency bands. A similar analysis is presented, but with more pronounced effects, for Ka-band radar. The analysis is carried out for array lengths of 32, 64, and 200 antenna elements at each frequency. The performance losses caused by the phase perturbations are explained and summarized in terms of the signal-to-interference-plus-noise ratio (SINR) and the SINR Loss (L_{SINR}).

Fully adaptive performance losses due to atmospheric turbulence are less than 1 dB for most array sizes, frequencies, and typical turbulence strengths. The 200 element array faces a 6 dB performance loss at 30 GHz under turbulence of $C_n^2 = 5 \times 10^{-12}$ $m^{-2/3}$. Similar

losses are recorded for Factored Time-Space and for all experiments where sampling of the interference through turbulence is simulated.

ATMOSPHERIC INDUCED ERRORS
IN
SPACE-TIME ADAPTIVE PROCESSING

I. Introduction

1.1 Overview

Ground-based radar systems use electromagnetic (EM) waves to detect targets in a predefined space and track their position, range, velocity, and many other characteristics. EM waves employed in radars systems are subject to disruptive atmospheric effects. Among these effects are the perturbations introduced by atmospheric turbulence. Turbulence begins with the radiative solar heating of the earth. Thermal energy radiated to the earth from the sun passes through convection to the near-to-ground atmosphere. The additional effects of water vapor molecules in the air and atmospheric pressure variations increase the turbulent conditions. These thermal, vapor, and pressure factors induce random motion in the air particles of the atmosphere. This random motion may be modeled as many shifting air pockets with randomly varying shapes, sizes, and refractive indices. These conditions of atmospheric turbulence are most pronounced near to the ground. Just as in optical systems, turbulent atmosphere induces amplitude scintillations and phase perturbations in propagating EM waves. However, the more critical effects occur in the phase of the EM wave. These fluctuations in the phase of an EM wave hinder the performance of ground-based antennas. Antenna arrays which use phasing for beamsteering and nulling are especially prone to the effects of turbulence. Space-Time Adaptive Processing (STAP) techniques are also vulnerable to atmospheric turbulence effects. This thesis examines the effects of atmospheric turbulence on the performance of STAP systems.

1.2 Supporting work

The effects of atmospheric turbulence are most pronounced at optical wavelengths. At longer wavelengths, the effects are less severe but perturbations nonetheless occur.

Phase perturbation effects are more extreme in systems with shorter wavelengths, longer propagation path lengths, and larger receiver separations. Hill, Bohlander, Clifford, and McMillan have measured phase difference variances in millimeter waves propagating near to the ground under light turbulent conditions. Light turbulent conditions may be expressed by a typical index of refraction structure constant (C_n^2) value on the order of 10^{-14} $m^{-2/3}$. Over more than a kilometer of propagation and under these light turbulent conditions, antenna receivers separated by 10 meters measured phase difference variances as high as 0.5 rad^2 [11],[12].

Radar normally operates in the range of millimeter to centimeter wavelengths. While this portion of the spectrum is typically less prone than higher wavelengths to turbulence effects, the propagation distances in radar applications are usually much greater than those examined in the Hill experiment. Consequently, the turbulence induced phase perturbations on propagating EM waves are an overriding concern for large radar antenna arrays. The concern is especially relevant for those radars operating near to the ground.

1.3 Relevance

Accurate radar beamsteering is made possible by phasing in antenna arrays. The phase of a signal may be translated into a precise direction of arrival (DOA) for that signal. By detecting the phase of a received signal, an antenna array may determine the signal's DOA. The Air Force is motivated to improve the performance of both airborne and ground-based arrays. In the case of ground-based antenna arrays, locally occurring turbulence can contribute to the disruption of the EM wave and degrade the performance of the array antenna system. This performance degradation is especially true in situations involving low target elevation angles. The low target elevation leads to long propagation distances through the turbulence, thereby increasing the turbulence effect.

Strong turbulence causes phase aberrations which result in random phase shifts over the length of the array. These phase shifts mar the true phase, making the array receiver less effective in placing the mainbeam and nulls. For temporally shifting turbulence, phase variations in the signal will occur over the duration of the transmitted waveform, from pulse to pulse within a coherent processing interval (CPI). In addition, temporally shifting

turbulence may fully or partially obsolete an adaptive solution before it is applied. These signal fluctuations over distances and time produce errors in the computed DOA and target doppler frequency, respectively. Consequently, an adaptive weighting scheme for the array, calculated based on knowledge of the target location and applied under turbulent conditions, does not perform optimally. Similarly, a weighting scheme developed using information perturbed by the turbulent conditions also offers sub-optimal performance. STAP systems which employ partially adaptive techniques are even more prone to atmospheric induced errors. These systems sacrifice degrees of freedom (DOF) and performance to improve computation time. By sacrificing DOF these partially adaptive STAP systems are using fewer than the full complement of elements and CPI pulses available. The phase errors induced by atmospheric turbulence degrade the accuracy of the adaptive solutions developed in fully and partially adaptive STAP systems.

Developing improvements to antenna systems for better target detection and DOA estimation is a major thrust of the Air Force Research Laboratories (AFRL). One focus area of the AFRL is in the development of STAP techniques. STAP techniques, originally envisioned for use in airborne radar arrays, are designed to improve target beamforming while improving nulling of clutter and barrage jammers. These techniques may also be applied to ground-based arrays which are often larger in size and more prone to phase variations caused by atmospheric turbulence. Radar arrays typically operate in the L, S, C, or X-band region of the spectrum (1-12 GHz). Even at such low operating frequencies, there are some phase variations introduced by the turbulence in the atmosphere. Atmospheric conditions affecting the phase of EM waves will degrade STAP performance. However, since they incorporates adaptivity, STAP techniques may also be used to compensate for turbulent conditions in much the same way adaptive optics techniques improve imaging through the atmosphere [12]. So STAP has a lot of potential for use in ground-based radar arrays.

1.4 Approach

The overall effect of atmospheric turbulence on STAP performance in ground-based radar is unknown. This thesis provides some understanding of these effects. To establish this understanding, the following steps are taken

- Develop spatial phase perturbation statistics for combinations of
  - arrays with geometries (defining spatial DOF) of 200 antenna elements, 64 antenna elements, and 32 antenna elements spaced at half-wavelength intervals
  - 3GHz, 10GHz, and 30GHz radar systems
  - C_n^2 values of 5×10^{-14}, 5×10^{-13}, 5×10^{-12}, 5×10^{-11}, 5×10^{-10} $\mathrm{m}^{-2/3}$
- Carry out simulations of STAP in a turbulent environment
  - Joint Domain Optimum (JDO) method - fully adaptive
  - Factored Time-Space (FTS) method - partially adaptive
- Document the extent of the STAP performance degradation

This study concentrates on the nulling and beamsteering performance of systems using STAP algorithms under turbulence. To focus on the errors caused by phase perturbations, this study assumes the only interference in the environment is caused by clutter returns. Jammers are assumed absent from the problem.

1.5 Summary

This thesis establishes a measure of the effects of atmospheric turbulence on radar arrays and STAP performance.

Chapter II introduces some key statistical concepts in atmospheric turbulence theory. These concepts include the index of refraction model, index of refraction structure constant, and the phase structure constant. Chapter II also includes an orientation to the primary STAP algorithms and the appropriate performance metrics. Chapter III discusses the effects of turbulence on STAP techniques using the tools described in Chapter II. This

chapter also includes an analytical development of the effects on STAP performance. Chapter IV describes the organization of the experiment and the simulation tools used. This chapter includes procedures used for simulating turbulence effects and the settings used for the parameters of the experiment. Chapter V describes the results of the experiment. Chapter VI summarizes the experimental results and includes suggestions for future areas of study.

II. Background

Since atmospheric turbulence effects are the focus of this thesis, this chapter opens with a development of some important statistical quantities for characterizing turbulence. These statistical quantities help to characterize the degree and extent of atmospheric turbulence.

The index of refraction model represents the variations in the atmospheric refractive index under turbulent conditions. Hill, Clifford, and Lawrence developed a method by which to calculate the index of refraction structure function from data on temperature, humidity, and pressure variations [10],[8]. They went on to calculate the typical fluctuations of these meteorological quantities at different wavelengths [8],[9]. In addition, Hill *et al.* amassed experimental data on phase perturbations for millimeter waves propagating over the ground [11],[12] as well as phase perturbation data at lower frequencies [13].

The index of refraction structure constant C_n^2 is a measure of the degree of refractive index fluctuations. It provides an effective scalar measure of the strength of the turbulence. The index of refraction structure function D_n and the phase structure function D_S are derived from C_n^2 and directly impact the statistics of the EM wave variations between points separated in space. A measure of the spatial and temporal variations in the EM wave transverse to its propagation direction is the mutual coherence function (MCF) [16],[3],[14]. A method of simulating the turbulence induced phase perturbation comes from the correlation properties of the phase structure function and the MCF. This method is known as phase screen generation and can simulate the relative phase perturbation at any point in space [18]. Experimental data highlighting turbulence statistics for optical, millimeter, and centimeter wavelengths are presented in addition to the statistical developments mentioned.

The second portion of this chapter includes a brief orientation to STAP. In this orientation, similar to that presented by Ward [17], the STAP algorithms are developed for:

- Joint Domain Optimum (JDO) - a fully adaptive STAP method
- Factored Time-Space (FTS) - an element space post-Doppler partially adaptive STAP method

In addition to these STAP algorithms, two important STAP metrics are introduced. These metrics are the signal-to-interference-plus-noise ratio (SINR) and SINR Loss (L_{SINR}).

2.1 Notation and Definitions

In this section, the most common symbols and notation are introduced. Much of the notation used in this thesis is common to the atmospheric turbulence and radar adaptive signal processing research communities. A good part of this document uses linear algebra and matrix conventions.

2.1.1 Linear algebra conventions. Matrix and vector notation is used heavily in this document. Vectors are represented by boldface lowercase letters and greek symbols such as $\mathbf{s}$ and $\boldsymbol{\mu}$. Vectors are assumed to be column vectors unless otherwise specified. Another type of vector is written in the form $\vec{r}$. This notation refers mainly to spatial quantities and denotes a vector pointing in space as

$$\vec{r} = r_x\vec{x} + r_y\vec{y} + r_z\vec{z}$$

with components in each of the three orthogonal directions. These directions are represented by the unit vectors $\vec{x}$, $\vec{y}$, and $\vec{z}$. The vector $\vec{r}$ may also be represented as a 3×1 column vector

$$\mathbf{r} = [r_x \; r_y \; r_z]^T.$$

Matrices are denoted by boldface, capital letters and greek symbols. Examples of matrix notation include $\mathbf{A}$ and $\boldsymbol{\Xi}$. Matrices may also be denoted as a vector of vectors. Examples of this notation are

$$\mathbf{A} = [\mathbf{a}\ \mathbf{b}\ \mathbf{c}] \qquad \mathbf{B} = \begin{bmatrix} \mathbf{c}^T \\ \mathbf{b}^T \\ \mathbf{a}^T \end{bmatrix}.$$

The superscript T, $(\cdot)^T$, denotes the transpose operation. A superscript H, $(\cdot)^H$, denotes transposition combined with substitution of each element by its complex conjugate. The complex conjugate is represented by $(\cdot)^*$.

The linear algebra product of two or more matrices may be expressed as $\mathbf{AB}$ and $\boldsymbol{A \Xi B}$. Two other relevant multiplication operations are the Hadamard product,

$$\mathbf{A} \odot \mathbf{B} = \begin{bmatrix} a_{11}b_{11} & a_{12}b_{12} & a_{13}b_{13} \\ a_{21}b_{21} & a_{22}b_{22} & a_{23}b_{23} \\ a_{31}b_{31} & a_{32}b_{32} & a_{33}b_{33} \end{bmatrix},$$

and the Kronecker product,

$$\mathbf{A} \otimes \mathbf{B} = \begin{bmatrix} a_{11}\mathbf{B} & a_{12}\mathbf{B} & a_{13}\mathbf{B} \\ a_{21}\mathbf{B} & a_{22}\mathbf{B} & a_{23}\mathbf{B} \\ a_{31}\mathbf{B} & a_{32}\mathbf{B} & a_{33}\mathbf{B} \end{bmatrix}.$$

Either operation may be performed on vectors or matrices.

2.1.2 Statistical conventions. Much of the work in the fields of atmospheric turbulence and adaptive processing involve statistical quantities. The following conventions are useful in representing statistical concepts.

The ensemble average or expected value of a random variable X, written as $E[X]$, is defined as

$$E[X(z)] = \int X(z) f_X(z) dz.$$

This expression is written in the general form for the random process, X, with respect to the random variable, z. In this expression, $f_X(z)$ is the probability density function of the random process. The expected value is often known as the mean or the ensemble average and may also be denoted as $\langle X \rangle$. If X is a single random variable, then $E[X]$ is a scalar value. If $\mathbf{X}$ is a matrix (vector) of random variables, then $E[\mathbf{X}]$ is also a matrix (vector) of ensemble averages.

The second order statistics include the variance and covariance of random processes. The variance is a measure of a random variable's deviation from it's expected value,

$$\begin{aligned} \mathrm{Var}(X) &= E[(X - E[X])^2] \\ &= E[X^2] - E^2[X]. \end{aligned}$$

For zero-mean random variables, the variance may be simplified to

$$\mathrm{Var}(X) = E[X^2],$$

where $E[X^2]$ is also known as the mean square value. The covariance of two random variables, X and Y, is defined as

$$\mathrm{Cov}(X,Y) = E[(X - E[X])(Y - E[Y])]$$

and also simplifies to

$$\mathrm{Cov}(X,Y) = E[XY] - E[X]E[Y].$$

Once again, the variance or covariance of a single random variable is a scalar quantity while that of a matrix (vector) is a matrix (vector) of variances or covariances. In addition, the radar adaptive processing portion of this document often denotes the covariance matrix as **R**.

If a random variable is known to have a Gaussian distribution, a great deal is known about that random quantity. If the mean μ and the variance σ^2 of the distribution are known, the characterization of the random variable is complete. All the necessary information about the random variable X with such a distribution may be conveyed by

$$X \sim \mathcal{N}(\mu, \sigma^2),$$

where the notation $\mathcal{N}$ denotes the distribution of a Gaussian random variable.

2.1.3 Other conventions. For a complex quantity, X, the magnitude of the number is given by $\text{amp}(X)$ or by $|X|$. The angle or phase of the quantity is given by $\text{ang}(X)$ or by $\angle X$. The real portion of the quantity is given by $\text{Re}(X)$ and the imaginary portion is given by $\text{Im}(X)$.

2.2 Atmospheric Turbulence

This section summarizes the research done to understand atmospheric turbulence effects on EM wave propagation. Many models exist for the EM wave propagating through the atmosphere. These models were largely developed by Tatarski and were presented by Fante and Strohbehn. Each of the models are most accurate under their own specifically defined conditions. One the most important of these conditions concerns the frequency of the EM wave.

In general, the effects of atmospheric turbulence are more acute in EM waves with shorter wavelengths. General effects of atmospheric turbulence in the troposphere (altitude < 10 km) [16] include

- absorption leading to signal attenuation
- wave direction changes (bending) proportional to altitude due to dielectric constants changing with height
- random dielectric constant variations causing random wave scattering which result in
  - (a) amplitude variance
  - (b) phase variance
  - (c) direction of arrival (DOA) variance
  - (d) polarization variance

Since higher frequencies suffer more from atmospheric turbulence effects, much of this field of research focuses on the optical spectrum (outside the millimeter wave band, >300 GHz). In fact, quite a bit of progress has been made in the field of adaptive optics and

atmospheric turbulence compensation with adaptive mirrors [14]. In the interests of array antenna radar systems, this thesis focuses on the primary radar frequencies (3-30 GHz, 1 cm $\leq \lambda \leq$ 10 cm).

As mentioned in Sec. 1.3, randomness introduced into the phase of a propagating wave can have debilitating effects on STAP performance. Models of atmospheric turbulence effects on EM waves yield some valuable insight into the EM wave phase statistics. Amplitude variations in the propagating EM wave are reported to be log-normal and similarly, phase variations are shown to follow a Gaussian distribution [16],[11]. Therefore, knowing the first and second order statistics of these phase perturbations can provide a precise description of the turbulent effect. A number of important relations are derived in this chapter to provide information on the statistics of the phase variations. These relations are the index of refraction structure constant C_n^2; the index of refraction structure function $D_n(\boldsymbol{\rho}, t)$; the wave structure function function $D(\boldsymbol{\rho}, t)$; and the phase structure function $D_S(\boldsymbol{\rho}, t)$. Using these tools, the turbulence effects on STAP may be fully understood.

2.2.1 Index of refraction model. Fante, Roggemann and Welsh, and others point out that temperature variations cause random fluctuations in the index of refraction [6],[14] with respect to position $\vec{r}$ and time t. This random quantity is

$$n(\vec{r}, t) = 1 + n_1(\vec{r}, t). \tag{2.1}$$

The zero-mean, randomly fluctuating term in the index of refraction, $n_1(\vec{r}, t)$, is caused by temperature differences between the various regions of air. The thermal effects mentioned in Sec. 1.1 cause these temperature gradients. The subsequent randomly varying regions, or pockets, of air are further diversified by spatial humidity characteristics and pressure fluctuations in the atmosphere.

2.2.2 Index of refraction structure constant, C_n^2, and Kolmogorov spectrum, $\Phi_n(\kappa)$. The pockets of air, also known as turbulent eddies, have randomly varying shape, size and index of refraction. The randomly fluctuating refractive index term, $n_1(\vec{r}, t)$, is shown to be Gaussian distributed with zero mean and covariance exhibiting stationarity in local regions

[6]. This means that the covariance of the random index of refraction, instead of being a function of position, is a function of the distance between points in three dimensional space, $\rho = \vec{r} - \vec{r}'$. The scale of the turbulence characterizes the strength of the turbulence and may be expressed as a function of the statistical distribution of the eddy sizes $[l_x, l_y, l_z]$. This distribution may be written from Kolmogorov Theory, which characterizes the statistics of index of refraction variations in terms of mathematical formulas. These mathematical formulas are written in terms of the eddy spatial frequency $\kappa = \sqrt{\kappa_x^2 + \kappa_y^2 + \kappa_z^2}$. The eddy spatial frequency is given in terms of the eddy sizes by

$$\kappa = \begin{bmatrix} \kappa_x \\ \kappa_y \\ \kappa_z \end{bmatrix} = \begin{bmatrix} 2\pi/l_x \\ 2\pi/l_y \\ 2\pi/l_z \end{bmatrix}.$$

Kolmogorov Theory describes the distribution of the turbulence strength among various sized κ. A simplified expression of the power spectral density (PSD) is the von Karman spectrum $\Phi_n(\kappa, \rho)$. The mathematical form of the PSD is

$$\Phi_n(\kappa, \rho) = \frac{0.033 C_n^2(\rho) \exp[-(\frac{\kappa l_0}{2\pi})^2]}{[\kappa^2 + L_0^{-2}]^{11/6}}, \tag{2.2}$$

and is known as the von Karman spectrum. In the expression for the von Karman spectrum, L_0 is the outer scale of the turbulence and l_0 is the inner scale of the turbulence. These values represent the largest and smallest theoretical eddy sizes and represent boundaries which describe the extent of the spread of Φ_n. The index of refraction structure function is defined as

$$D_n(\rho) = E[(n_1(\vec{r}, t) - n_1(\vec{r} - \vec{r}', t))^2]. \tag{2.3}$$

In many cases, the index of refraction structure function exhibits minimal change with reference to ρ and simply appears as C_n^2. The value of C_n^2 is often used to express the strength of turbulence. In this study, C_n^2 is often referred to characterize the turbulence

strength. The expression for the von Karman spectrum then becomes

$$\Phi_n(\kappa) = \frac{0.033 C_n^2 \exp[-(\frac{\kappa l_0}{2\pi})^2]}{[\kappa^2 + L_0^{-2}]^{11/6}}. \tag{2.4}$$

Tatarski and others [10],[14],[4] have shown that a sufficiently accurate representation of the von Karman spectrum is

$$\Phi_n(\kappa) = 0.033 C_n^2 \kappa^{-11/3}. \tag{2.5}$$

2.2.3 Phase structure function. Just as Eqn. (2.3) describes the index of refraction structure function, a similar expression describes the EM wave strucure function. The EM wave is given by Clifford and Lataitis [3] as

$$\begin{aligned} e(\vec{r},t) &= A_0(\vec{r},t)\phi(\vec{r},t) \\ &= A_0(\vec{r},t)e^{\psi(\vec{r},t)}. \end{aligned} \tag{2.6}$$

Here, $A_0(\vec{r},t)$ is the unperturbed electric field. The turbulence perturbation is contained in the exponential quantity which is written as

$$\begin{aligned} \phi(\vec{r},t) &= \exp(\psi(\vec{r},t)) \\ &= \exp(\chi(\vec{r},t) + jS(\vec{r},t)). \end{aligned} \tag{2.7}$$

In this expression, the log amplitude term, $\chi(\vec{r},t)$ is related to the amplitude perturbation by

$$\chi(\vec{x},t) = \ln \frac{A(\vec{x},t)}{|A_0(\vec{x},t)|}. \tag{2.8}$$

The zero-mean turbulence effect on the amplitude of the EM wave is given by $A(\vec{x},t)$. The log amplitude perturbation term is small in comparison to the phase perturbation term given by $S(\vec{r},t)$. In this phase term, $S(\vec{r},t)$ is the zero-mean perturbation of the phase of the EM wave due to turbulence.

The wave structure function represents the statistics of the amplitude and phase changes due to turbulence. The wave structure function is

$$\begin{aligned} D(\boldsymbol{\rho},t) &= E[(\psi(\vec{r},t)-\psi(\vec{r}-\vec{r}',t))^2] \\ &= 2E[\psi^2(0,t)]-2E[\psi(\vec{r},t)\psi^*(\vec{r}-\vec{r}',t)]. \end{aligned} \tag{2.9}$$

The wave structure function may be divided into two parts,

$$D(\boldsymbol{\rho},t) = D_\chi(\boldsymbol{\rho},t) + D_S(\boldsymbol{\rho},t). \tag{2.10}$$

The first term represents the amplitude structure function and the second is the phase structure function. The phase structure function,

$$D_S(\boldsymbol{\rho},t) = E[(S(\vec{r},t)-S(\vec{r}-\vec{r}',t))^2], \tag{2.11}$$

provides a statistic by which the effects of turbulence on the EM wave phase may be measured. The phase structure function is a second order statistic representing the variance of the spatial phase difference due to the turbulence induced perturbation.

2.2.4 Experimental Results. Section 2.2.2 highlights the importance of the index of refraction structure constant as a parameter characterizing the strength of turbulence. A number of researchers have compiled C_n^2 values under varying conditions and at different frequencies.

In calculations reported by Hill, Clifford, and Lawrence [9],[10],[8], it is evident that both temperature and humidity factors affect the turbulence at all frequencies. While the turbulence effects are more pronounced at higher frequencies, the proportion of the effect on C_n^2 due to humidity is significantly higher at radar frequencies than at higher frequencies. It is this humidity factor which contributes significantly to turbulence effects in radar waves propagating near the ground.

Hill, Bohlander, Clifford, and McMillan [11],[12] measured phase difference and associated statistics for 173 GHz waves propagating over flat ground for a distance of 1374

m at a height of 3.68 m. Comparing the values of C_n^2 derived from measured data to values calculated from measured micrometeorological data using methods presented in Sec. 2.2.1 resulted in good agreement. These millimeter-wave C_n^2 values were on the order of 10^{-12} $m^{-2/3}$. Data from propogating optical frequencies also agreed with theoretical predictions calculated via micrometeorological measurements. In Chapter IV, this data is used to validate the phase screen generator used to calculate $D_S(\rho)$ under different C_n^2 values.

Fante [7] also points out a number of C_n^2 measurements taken under different conditions. The Bufton, Hufnagel structure constant model for optical wavelengths is

$$C_n^2 = 2.7 \times 10^{-16} \left[3\langle v^2 \rangle \left(\frac{h}{10} \right)^{10} e^{-h} + e^{-(h/1.5)} \right], \tag{2.12}$$

where turbulence is approximated at height h for a mean square wind velocity $\langle v^2 \rangle$. Vernin *et al.* measured C_n^2 values at optical wavelengths ranging from 3.9×10^{-17} $m^{-2/3}$ at $h = 3$ km to 7×10^{-18} $m^{-2/3}$ at $h = 16$ km. The Hufnagel model calculations yield values on the same order as Vernin's measurements for all heights and equals Vernin's measured values for heights above 16 km. Barletti also measured optical wavelength C_n^2 values for varying heights and arrived at similar results.

Kallistratova measured optical wavelength C_n^2 values at a height of 2.5 m in the range of 5.4×10^{-14} $m^{-2/3}$ and 5.4×10^{-13} $m^{-2/3}$ with high probability. Rome Air Development Center (RADC) measurements of C_n^2 in the optical spectrum at a height of 3 m also show values on the order of 10^{-13} $m^{-2/3}$ to 10^{-14} $m^{-2/3}$. The RADC measurements during the day varied from those taken at night. The measured RADC relationship of C_n^2 to height h was found to be

$$C_n^2(h) \simeq C_n^2(1) h^{-4/3}, \tag{2.13}$$

while the nighttime relationship was

$$C_n^2(h) \simeq C_n^2(1) h^{-2/3}. \tag{2.14}$$

Hall measured an average $C_n^2(1) = 6 \times 10^{-13}$ m$^{-2/3}$ and reports similar relationships as those reported by RADC.

Thompson *et al.* measured C_n^2 at 9.4 GHz frequency for heights from 0.15 km to 7.6 km. Here also, the peak C_n^2 value was on the order of 10^{-13} m$^{-2/3}$. Thompson also gathered C_n^2 measurements at 3 GHz frequency and heights from 0.8 km to 1.5 km. These measurements also found C_n^2 to be on the order of 10^{-13} m$^{-2/3}$. Fante claims that water vapor effects near the ground cause C_n^2 values at low frequencies to be one to two orders of magnitude higher than in the optical frequency range. Fante goes on to cite thoeretical work by Brown which confirms this statement for 10 GHz waves at heights up to 3 m.

Strohbehn and Fante [16],[6] among others acknowledge that temporal phase fluctuations induced by turbulence in the EM wave are of much smaller magnitude and frequency than spatial phase fluctuations. Taylor's frozen flow hypothesis attributes temporal phase perturbations to spatial perturbations which are moved due the effect of winds with velocity $\vec{v}$ [6],[14]. Where there is some significant wind velocity, the index of refraction after some time Δt is

$$\begin{aligned} n(\vec{r}, t + \Delta t) &= n(\vec{r} + \vec{v}\Delta t, t) \\ &= 1 + n_1(\vec{r} + \vec{v}\Delta t, t). \end{aligned} \tag{2.15}$$

In this study, it is assumed that there is no significant wind velocity present. Therefore, the simulations described in Chapter IV concentrate only on the spatial phase perturbations induced by the turbulence.

From the research summarized in this section, it is clear that atmospheric turbulence perturbations are effective at radar frequencies near to the ground. These perturbation effects are of significant magnitude and their effect on STAP is presented in Chapter V.

2.3 Space-Time Adaptive Processing (STAP) Orientation

This section first introduces the basic concepts involved in array beamforming. It goes on to highlight the important symbols and relationships in STAP. Having introduced these concepts, this section provides an explanation of the key algorithms in the STAP

Figure 2.1 Antenna array in operational environment. A typical ground-based antenna array must resolve airborne targets while dealing with airborne and ground-based jammers. Another major obstacle to overcome is ground clutter. Ground clutter becomes increasingly disruptive in the case of resolving targets at low elevation angles. Graphic taken from Jane's Weapons Systems [2].

development. Many of the concepts presented in this section are adapted from Ward's Technical Report [17].

2.3.1 Antenna array beamforming basics. The purpose of the radar antenna is to transmit EM energy and then receive the resulting reflections of this energy from the surrounding space. In this way, the antenna may be used to detect and track targets in this space. Antenna arrays offer the advantage of being able to transmit EM energy in the form of a signal in a precise direction. This form of directional selectivity is known as beamforming or beam-steering in the far-field [5]. The far-field refers to ranges over which propagating EM wavefronts appear as plane waves. Antenna arrays are also capable of preventing EM transmission in specific directions. This is known as antenna nulling. Just as the antenna array can "steer" and "null" for transmission, it can also "steer" and "null" for reception. This means that the antenna array can capture EM signals with a specific direction-of-arrival (DOA) and using similar methods, reject EM signals impinging with a specific DOA. Figure 2.1 depicts the situation under study. Beamsteering and nulling proves very useful in complex environments full of targets, jammers, and clutter such as that depicted in Figure 2.1.

The ability of an antenna array to steer and null are tied to two important concepts. These concepts are the phasor form of the EM wave and the relative spacing and phasing of the antenna elements.

2.3.1.1 EM phasor form. The phasor form of the EM plane wave is

$$e(\mathbf{r},t) = E_o e^{j(\omega t \pm \mathbf{k}^T \mathbf{r})}. \tag{2.16}$$

In this form, the amplitude of the EM wave is E_0 and t represents its temporal dependance. Since the phasor notation denotes a sinusoid, ω is known to be the temporal frequency of the EM wave. The temporal frequency describes the number of periodic cycles through which the EM wave traverses in each unit of time. As a plane wave traveling in space and oscillating in time, the EM wave also demonstrates spatial dependences through

$$\mathbf{r} = [r_x \; r_y \; r_z]^T \tag{2.17}$$

where each element of the vector represents a distance in an orthogonal direction. The three-dimensional unit vector is

$$\mathbf{r}_{unit} = \frac{1}{\sqrt{3}}[1 \; 1 \; 1]^T.$$

Just as t and ω describe the temporal dependence of the EM wave, $\mathbf{r}$ and $\mathbf{k}$ describe the relationship, in space, between EM wave periods and distance. The three-dimensional spatial frequency is given by

$$\mathbf{k} = 2\pi \left[\frac{1}{\lambda_x} \; \frac{1}{\lambda_y} \; \frac{1}{\lambda_z}\right]^T. \tag{2.18}$$

The three-dimensional wavelength may be written in similar terms as

$$\boldsymbol{\lambda} = 2\pi \left[\frac{1}{k_x} \; \frac{1}{k_y} \; \frac{1}{k_z}\right]^T. \tag{2.19}$$

The spatial frequency is written in terms of the element-by-element inverse of the EM wavelength $\boldsymbol{\lambda}$ in each of the three orthogonal directions. The spatial frequency describes the number of EM wave periods contained in a given three-dimensional spatial distance.

2.3.1.2 Element spacing and phasing. The second important concept in beamsteering and nulling involves the antenna element spacing and phasing. The velocity at which an EM wave propagates through space is given by

$$v_p = \frac{1}{\sqrt{\mu\epsilon}}, \tag{2.20}$$

and is tied to the intrinsic properties of the medium. These properties are the permittivity, ϵ, and the permeability, μ. The direction of propagation, is directly related to the spatial frequency and consequently, to the component of the wavelength in each orthogonal direction. The direction of propagation is given by

$$\mathbf{r}_{v_p} = \frac{\boldsymbol{\lambda}_{v_p}}{||\boldsymbol{\lambda}_{v_p}||} = \frac{[\lambda_{v_{px}}\ \lambda_{v_{py}}\ \lambda_{v_{pz}}]^T}{\sqrt{\lambda_{v_{px}}^2 + \lambda_{v_{py}}^2 + \lambda_{v_{pz}}^2}}. \tag{2.21}$$

The EM wave velocity, an expression of distance traveled per unit time, may be expressed in terms of both the temporal and spatial frequencies as

$$\mathbf{v}_p = \frac{\omega_p}{2\pi}\boldsymbol{\lambda}_{v_p}. \tag{2.22}$$

The antenna element spacing is normally fixed based upon $\boldsymbol{\lambda}_{v_p}$. A linear antenna array consists of a series of N antenna elements spaced at distance

$$\mathbf{d} = \frac{1}{2}\boldsymbol{\lambda}_{v_p} = [d_x\ d_y\ d_z]^T. \tag{2.23}$$

The spacing of the elements in the the three orthogonal directions id given by d_x, d_y, and d_z. The relationship between $\mathbf{d}$ and $\boldsymbol{\lambda}_{v_p}$ prevents grating lobe interference. The half-wavelength spacing ensures that the spatial sampling rate $\mathbf{k}_{samp}$ is twice that of the signal

spatial frequency $\mathbf{k}_{v_p}$. This relationship is summarized by

$$\begin{aligned} \mathbf{k}_{samp} &= 2\pi \left[\frac{1}{d_x} \; \frac{1}{d_y} \; \frac{1}{d_z} \right]^T \\ &= 2\pi \left[\frac{2}{\lambda_{px}} \; \frac{2}{\lambda_{py}} \; \frac{2}{\lambda_{pz}} \right]^T \\ &= 2\mathbf{k}_{v_p}. \end{aligned} \tag{2.24}$$

The linear antenna array pictured in Fig. 2.2 is located in the vicinity of the propagating EM wave $e_{1r}(\mathbf{r}, t)$ having velocity $\mathbf{v}_{p_{1r}}$ and direction given by $\mathbf{k}_{p_{1r}}$. An EM wave propagating in this way will impinge on antenna element #0 first. It will then contact element #1, then #2, and so on.

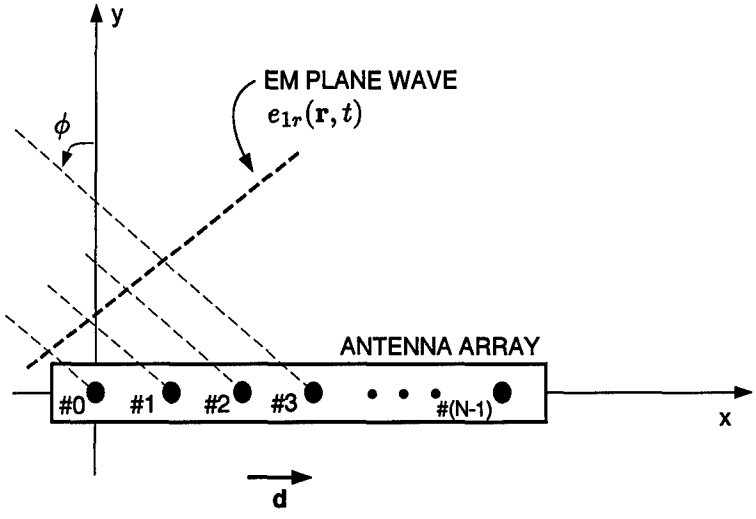

Figure 2.2 EM wave impinging on linear antenna array.

The antenna array pattern for the array steered to $\mathbf{k}_s$ is given by

$$W(\mathbf{k}_s) = \frac{1}{N} \sum_{n=0}^{N-1} w_n e^{-j(\mathbf{k}_{p_{1r}} - \mathbf{k}_s)^T \mathbf{r}_n}, \tag{2.25}$$

where w_n is the weight on the n^{th} antenna element and the vector $\mathbf{r}_n$ represents the spatial distances to the n^{th} antenna element. The phase on the n^{th} element must be

$$\psi_{1r}(n) = \mathbf{k}_{p_{1r}}^T \mathbf{r}_n \tag{2.26}$$

in order to receive the signal $e_{1r}(\mathbf{r}, t)$ [5].

2.3.2 STAP geometry and radar equations. This section introduces the orientation of the STAP platform in space as well as the orientation of the target and interference. The section ends with an analytic description of the radar signal received by the antenna array.

2.3.2.1 Platform Geometery. The primary goals of STAP are

- to steer the antenna mainbeam in the direction of the target
- to suppress interference resulting from reflected radar energy from the ground and other clutter,
- to suppress interference caused by airborne jammers.

To steer and null the antenna pattern based on these conditions, a geometry must exist to map targets, clutter, and jammers in space. The unit vector

$$\hat{p}(\phi, \theta) = \cos\theta \sin\phi \hat{x} + \cos\theta \cos\phi \hat{y} + \sin\theta \hat{z}. \tag{2.27}$$

points to the region in space at ϕ azimuth and θ elevation with respect to the antenna platform. The vector $\hat{p}$ represents a spherical to rectangular coordinate transformation and may also be written as the column vector

$$\mathbf{p} = [\cos\theta \sin\phi \;\; \cos\theta \cos\phi \;\; \sin\theta]^T. \tag{2.28}$$

Figure 2.2 depicts the antenna array in reference to the impinging EM wave. Notice that in this definition, $\hat{\phi}$ points in the direction of the curve from the y-axis to the x-axis. Azimuth, however, is still defined in terms of $\hat{\phi}$ and elevation corresponds to $\hat{\theta}$. This is a similar geometry to that used by Ward [17]. Table 2.1 lists the symbols used in this document. Many of these symbols are defined in the following sections.

2.3.2.2 Array geometry. The STAP algorithms developed in this document revolve around a one-dimensional antenna array. Keeping in mind the geometry introduced

Table 2.1 STAP Symbiology

STAP Symbols	
L	number of range bins in each PRI
M	number of pulses in each CPI
N	number of array antenna elements
d	distance between antenna elements
$\hat{p}$	radar return element direction
$\mathbf{X}_l$	space-time returns for the l^{th} range
χ_l	space-time snapshot
$\mathbf{x}_{s_m}$	vector of antenna samples for pulse m
$\mathbf{x}_{t_n}$	vector of pulse samples for antenna elemnt n
$x_{n,m,l}$	single complex valued CPI datacube sample
ω_0,$2\pi f_0$	radar standard frequency
λ_0	radar standard wavelength
$G_t(\theta,\phi)$	antenna array transmit power pattern
$g(\theta,\phi)$	antenna element transmit power pattern
N_0	array element receive noise power spectral density
L_t	transmission losses
L_r	reception losses

in Sec. 2.3.2.1, the antenna array is oriented in the $\hat{x}$ direction and has N antenna elements. These antenna elements are numbered as $[0, 1, \ldots, N-1]$ and have a spacing, $\mathbf{d}$, based on the operating frequency, f_0, and Eqn. (2.23). The vector pointing to the n^{th} antenna element is

$$\mathbf{r}_n = n\mathbf{d} = \left[\frac{n\lambda_0}{2}\ 0\ 0\right]^T. \tag{2.29}$$

Figure 2.2 depicts the antenna array and the relevant direction vector.

2.3.2.3 Antenna pattern. Balanis points out that the beamsteering performance of the antenna array is tied to two primary components [1]. The two components are the antenna array pattern as well as the antenna element power pattern. The overall pattern is given by

$$[\text{Pattern}]_{total} = [\text{Array Pattern}] \times [\text{Element Pattern}] \tag{2.30}$$

$$= G_t(\theta,\phi) \times g_t(\theta,\phi). \tag{2.31}$$

Sec. 2.3.1 presents the development of achieving the desired array pattern through element phasing. From Eqn. (2.25), the array pattern is given by

$$G_t(\theta, \phi) = W(\mathbf{k}_s). \tag{2.32}$$

In this document, the element pattern is given as

$$f(\phi, \theta) = \begin{cases} \cos\phi & -90^\circ \leq \phi < 90^\circ \\ b_g \cos\phi & 90^\circ \leq < 270^\circ \end{cases}, \tag{2.33}$$

where b_g is the backlobe gain equal to -30 dB. The resulting antenna element power pattern is given as $g_t(\phi, \theta) = |f(\phi, \theta)|^2$.

Figure 2.3 exhibits the various overall antenna patterns used in this study. The 32 element, 64 element, and 200 element patterns are shown, steered broadside, on a dB scale. Notice the improvement in the antenna pattern focus as the number of antenna elements increases.

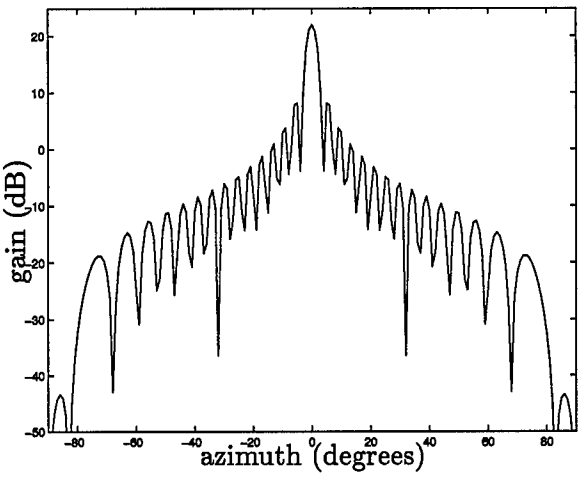

a) 32 element antenna pattern

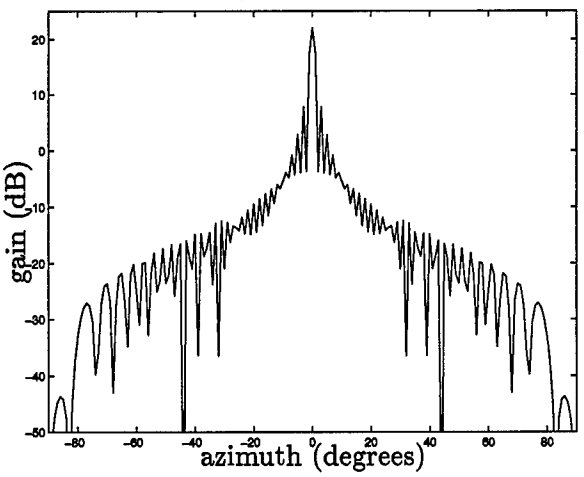

b) 64 element antenna pattern

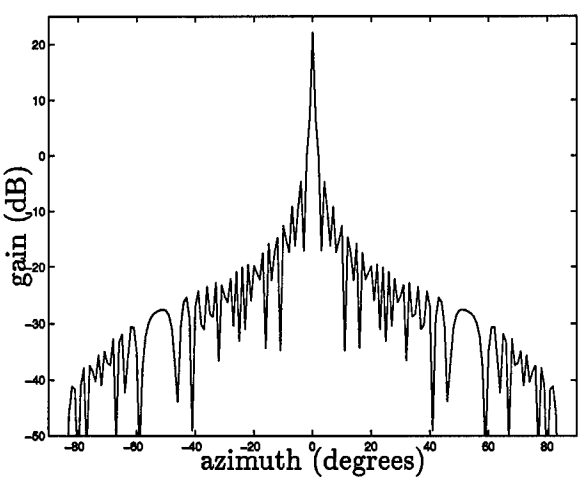

c) 200 element antenna pattern

Figure 2.3 Overall antenna pattern for various numbers of antenna elements. The antenna array is steered to broadside and has a gain of 22 dB.

2.3.2.4 Basic radar parameters. The dimensions of the coherent processing interval (CPI) define a number of important radar parameters. The radar CPI is composed of a series of M pulses transmitted by the N elements of the linear antenna array. The pulse spacing, or pulse repetition interval (PRI), is defined by

$$T_p = 1/f_r, \tag{2.34}$$

where f_r is the pulse repetition frequency (PRF). This series of pulses is modulated by a signal at the radar operating frequency f_0. The length of the CPI coherence window is

$$T_{\text{CPI}} = MT_p. \tag{2.35}$$

The range sampling rate is

$$f_s = \frac{v_p}{2R_u} \tag{2.36}$$

and is fixed based on the desired unambigious range R_u. A single radar return, sampled at f_s, is divided into L range sections or bins. All the information from,

- N antenna elements
- M pulses
- L range bins

may be organized into a datacube. Figure 2.4 depicts the CPI datacube. A slice of the cube at the l^{th} range bin yields the $N \times M$ space-time snapshot. This information may be

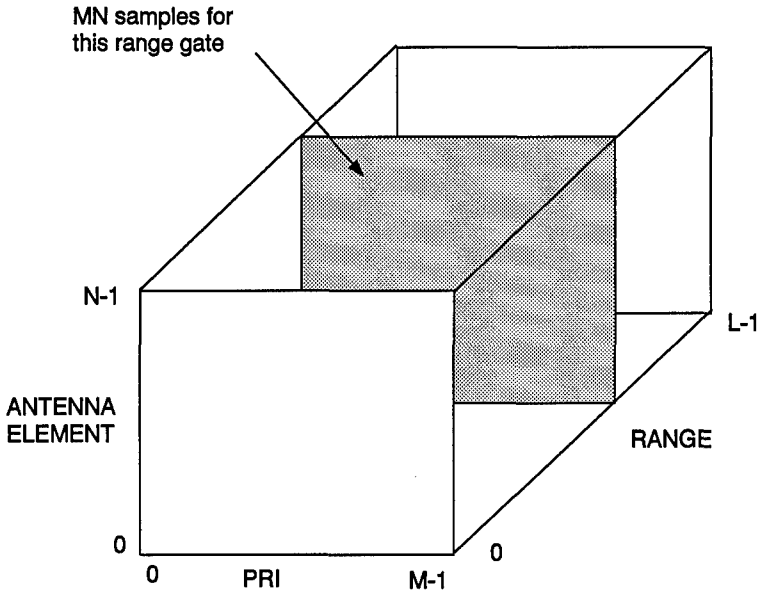

Figure 2.4 The CPI datacube structure represents the data received by the radar array on the N antenna elements over M pulses. The sampling rate gives resolution leading to L range bins. One slice of the cube represents the data from one range bin and holds MN samples of data. This slice is called the space-time snapshot.

represented in an $N \times M$ array,

$$\mathbf{X}_l = [\mathbf{x}_{s_0}\ \mathbf{x}_{s_1}\ \cdots\ \mathbf{x}_{s_{M-1}}]_l \tag{2.37}$$

$$= \begin{bmatrix} \mathbf{x}_{t_0}^T \\ \mathbf{x}_{t_1}^T \\ \vdots \\ \mathbf{x}_{t_{N-1}}^T \end{bmatrix}_l \tag{2.38}$$

$$= \begin{bmatrix} x_{0,0,l} & x_{0,1,l} & \cdots & x_{0,M-1,l} \\ x_{1,0,l} & x_{1,1,l} & \cdots & x_{1,M-1,l} \\ \vdots & & \ddots & \\ x_{N-1,0,l} & x_{N-1,1,l} & \cdots & x_{N-1,M-1,l} \end{bmatrix}, \tag{2.39}$$

composed of samples, $x_{n,m,l}$, from the n^{th} antenna element, the m^{th} pulse and the l^{th} range bin. The vector $\mathbf{x}_{t_n}$ is the set of pulse samples for the n^{th} antenna element. The vector $\mathbf{x}_{s_m}$ is the set of antenna element samples taken on the m^{th} pulse.

Working with vectors offers more flexibility than performing operations on arrays. For this reason, the array $\mathbf{X}_l$ is reconfigured to form the space-time snapshot. The space-time snapshot takes the form

$$\chi_l = \begin{bmatrix} \mathbf{x}_{s_0} \\ \mathbf{x}_{s_1} \\ \vdots \\ \mathbf{x}_{s_{M-1}} \end{bmatrix}, \tag{2.40}$$

and comes about by stacking the set of element sample vectors. The space-time snapshot is a key expression in the remainder of the STAP algorithm development.

2.3.2.5 Received power. In radar systems designed for target detection, the magnitude of signal power received has a significant effect on performance. The received signal power is a function of the received signal amplitude α_r. Since the received waveform is a reflection of that which is transmitted, the received signal power is also a function of the transmitted signal power. The energy transmitted at time t is given by

$$E_t(t) = \sum_{\substack{\text{transmitted} \\ \text{pulses}}} |s_t(t)|^2, \tag{2.41}$$

where $s_t(t)$ is the transmitted signal. The transmitted energy comes from summing the power in the pulses of the transmitted signal $s_t(t)$. The total transmitted power is a measure of the average energy transmitted over the CPI. The total transmitted power is

$$P_t = \frac{1}{MT_p} \int_0^{MT_p} E_t(t) dt. \tag{2.42}$$

The transmitted power is an important factor in calculating the received signal-to-noise ratio.

2.3.2.6 Signal-to-Noise Ratio (SNR). The received signal-to-noise ratio (SNR) for some object in space is

$$\xi_{obj} = \frac{P_{obj}}{P_N}, \tag{2.43}$$

where P_{obj} is the received signal power reflected by the object and P_N is the receiver noise power. Assuming the individual antenna element receiver noise is known to be σ^2, the individual antenna element SNR provides enough information to calculate the received power.

Equation (2.42) gives the power of the transmitted signal as P_t. Using the information about the transmitted power, the received SNR on each element for an object in the radar space is

$$\xi_{obj} = \frac{P_t T_p G_t(\theta_{obj}, \phi_{obj}) g_t(\theta_{obj}, \phi_{obj}) \lambda_0^2 \sigma_{obj}}{(4\pi)^3 N_0 L_t L_r R_{obj}^4}, \tag{2.44}$$

where σ_{obj} is the radar reflectivity, or radar cross section (RCS), of the object and R_{obj} is the distance of the object from the radar platform in meters. See Table 2.1 for definitions of other terms in the SNR equation. This SNR expression is given by the radar range equation [15]. The mean signal amplitude may be derived from ξ_{obj} as

$$\alpha_{obj} = \sqrt{\xi_{obj}\sigma^2}. \tag{2.45}$$

A number of statistical quantities presented later use the quantity α_{obj}.

Equation (2.44) demonstrates how an object's distance (R_{obj}), direction (ϕ_{obj}, θ_{obj}), and radar reflectivity (σ_{obj}), affects its SNR (ξ_{obj}). In the same way, location and reflectivity characteristics for targets affect the target SNR. The target SNR, from the radar range equation, is

$$\xi_t = \frac{P_t T_p G_t(\theta_t, \phi_t) g_t(\theta_t, \phi_t) \lambda_0^2 \sigma_t}{(4\pi)^3 N_0 L_t L_r R_t^4}. \tag{2.46}$$

Similarly, with reflectivity σ_{cp} and distance R_{obj} the clutter-to-noise ratio (CNR) for the cp^{th} patch of clutter is

$$\xi_{cp} = \frac{P_t T_p G_t(\theta_{cp}, \phi_{cp}) g_t(\theta_{cp}, \phi_{cp}) \lambda_0^2 \sigma_{cp}}{(4\pi)^3 N_0 L_t L_r R_{cp}^4}. \tag{2.47}$$

For ground-based antenna arrays, clutter is normally situated at low elevation angles. In this study, target returns which propagate through the greatest turbulent distance are of the most concern. These target returns also correspond to low elevation angles. Clutter may also be assumed to be evenly distributed in azimuth and may be modeled as a set of independent, equivalent clutter patches. The size of each clutter patch corresponds to the azimuthal resolution of the scanning antenna array. The number of patches is

$$N_c = \#\text{ of patches} = \frac{360^\circ}{\left[\begin{array}{c}\text{azimuthal}\\ \text{resolution}\\ \text{(in degrees)}\end{array}\right]}. \tag{2.48}$$

2.3.3 Steering vectors. In order for an antenna array to receive returns from targets, jammers, or clutter it must steer its mainbeam in their respective direction. Only EM energy transmitted in the direction of a reflecting object will generate a return signal from that reflector. Therefore, the antenna must first steer its transmission in a desired direction. In order to receive the return reflection signal, its receive mainbeam must also steer in that direction. This steering is accomplished in both space and time. By applying elemental phases to antenna elements (space) and waveform pulses (time), the array may steer the transmit or receive beam. In effect, the array filters the signal in space and time. The result is a beam with a relatively large gain in the desired direction at the desired Doppler frequency.

This beam steering is accomplished using steering vectors. The spatial and temporal steering vectors point the array mainbeam towards a certain azimuth and focus on a certain Doppler frequency, respectively. Combined they form the space-time steering vector which

performs both steering functions. The spatial steering vector is

$$\mathbf{a}(\vartheta_s) = \begin{bmatrix} 0 \\ e^{j2\pi(1)\vartheta_s} \\ e^{j2\pi(2)\vartheta_s} \\ \vdots \\ e^{j2\pi(N-1)\vartheta_s} \end{bmatrix}. \tag{2.49}$$

The spatial steering vector contains the phases which must be applied to each of the N antenna elements in order to steer the mainbeam in the (θ_s, ϕ_s) direction stipulated by the spatial frequency $\mathbf{k}_s$. Another form of the spatial frequency is

$$\vartheta_s = \frac{\mathbf{k}_s^T \mathbf{d}}{\lambda_0} = \frac{d}{\lambda_0} \cos\theta_s \sin\phi_s. \tag{2.50}$$

Similarly, the temporal steering vector is

$$\mathbf{b}(\varpi_s) = \begin{bmatrix} 0 \\ e^{j2\pi(1)\varpi_s} \\ e^{j2\pi(2)\varpi_s} \\ \vdots \\ e^{j2\pi(M-1)\varpi_s} \end{bmatrix}, \tag{2.51}$$

where

$$\varpi_s = \frac{f_s}{f_r} \tag{2.52}$$

is the normalized Doppler frequency corresponding to the Doppler frequency of interest f_s. The phases contained in $\mathbf{b}(\varpi_s)$ are applied to each of the M transmitted pulses.

Taken together, the spatial and temporal steering vectors form the space-time steering vector. The space-time steering vector is

$$\mathbf{v}_s(\varpi_s, \vartheta_s) = \mathbf{b}(\varpi_s) \otimes \mathbf{a}(\vartheta_s). \tag{2.53}$$

2.3.4 STAP statistical quantities: vectors and matrices. The signal processing for STAP is best done in vector and matrix form. To aid the development in this form, the expressions introduced in Sec. 2.3.2.4 are reconfigured so that the data appears in a new form. Equation (2.40) describes the space-time snapshot, a vector of sampled radar returns from a certain range bin in the radar space. This vector, χ, comes about by stacking the columns of a slice from the CPI datacube.

The vector χ represents the radar return. This vector may be rewritten as

$$\chi = \alpha_t \mathbf{v}_t + \chi_c + \chi_n. \tag{2.54}$$

Here, $\mathbf{v}_t$ is the space-time steering vector of the received target signal and α_t is the amplitude of the received signal. The other quantities are space-time snapshots for the jammers, clutter, and noise. These snapshots may be combined to form

$$\chi = \alpha_t \mathbf{v}_t + \chi_u, \tag{2.55}$$

where χ_u is the space-time snapshot for the undesired components. Each snapshot gives the signal power and phases for a particular interferer.

A statistical quantity representing the covariance of the undesired signal components in spatial angle (azimuth) and temporal angle (doppler frequency) is the space-time covariance matrix,

$$\mathbf{R}_u = E[\chi_u \chi_u^H]. \tag{2.56}$$

The space-time covariance matrix of the undesired signal components may be written as a combination of covariance matrices originating from different interference sources. The interference-plus-noise covariance matrix is given by

$$\begin{aligned} \mathbf{R}_u &= \mathbf{R}_c + \mathbf{R}_n \\ &= E[\chi_c \chi_c^H] + E[\chi_n \chi_n^H]. \end{aligned} \tag{2.57}$$

The clutter space-time snapshot, χ_c, for a single elevation angle comes about from the sum of space-time return steering vectors in the various azimuth directions. For a ground-based antenna, there is no Doppler shift for clutter returns so it is assumed that the normalized Doppler for clutter is $\varpi_s = 0$. The clutter space-time snapshot for all N_c clutter patches is

$$\chi_c = \sum_{cp=1}^{N_c} \alpha_{cp} \mathbf{v}(\vartheta_{cp}, \varpi_{cp}). \tag{2.58}$$

The signal amplitude of the cp^{th} clutter patch with spatial frequency ϑ_{cp} is α_{cp} The clutter signals are independent identically distributed (iid) so the clutter covariance matrix is written as

$$\begin{aligned} \mathbf{R}_c &= E[\chi_c \chi_c^H] \\ &= \sigma^2 \sum_{cp=1}^{N_c} \xi_{cp} \mathbf{v}_{cp} \mathbf{v}_{cp}^H \\ &= \sigma^2 \sum_{cp=1}^{N_c} \xi_{cp} (\mathbf{b}_{cp} \mathbf{b}_{cp}^H) \otimes (\mathbf{a}_{cp} \mathbf{a}_{cp}^H), \end{aligned} \tag{2.59}$$

where $\mathbf{a}_{cp}$, $\mathbf{b}_{cp}$, and $\mathbf{v}_{cp}$ are the spatial, temporal, and space-time steering vectors for the cp^{th} clutter patch. Another form for $\mathbf{R}_c$ uses the matrix of clutter patch space-time steering vectors defined by

$$\mathbf{V}_c = [\mathbf{v}_1 \ \mathbf{v}_2 \ \ldots \ \mathbf{v}_{N_c}], \tag{2.60}$$

and the diagonal matrix of N_c clutter patch return powers,

$$\Xi_c = \sigma^2 \times \begin{bmatrix} \xi_1 & & & \\ & \xi_2 & & \\ & & \ddots & \\ & & & \xi_{N_c} \end{bmatrix}. \tag{2.61}$$

Once again, assuming the clutter is iid, an equivalent expression for the clutter covariance matrix is

$$\mathbf{R}_c = \mathbf{V}_c \Xi_c \mathbf{V}_c^H. \tag{2.62}$$

The noise covariance matrix, $\mathbf{R}_n$ is the most straightforward of the three. Noise, in STAP processing, means antenna element receiver noise and is assumed to be an independent process in space and time. So the full rank noise covariance matrix is

$$\begin{aligned} \mathbf{R}_n &= \sigma^2(\mathbf{I}_N \otimes \mathbf{I}_M) \\ &= \sigma^2 \mathbf{I}_{MN}. \end{aligned} \tag{2.63}$$

The interference-plus-noise covariance matrix $\mathbf{R}_u$ is typically not well known and must be estimated from available data for use in the STAP algorithms. Since $\mathbf{R}_u$ is not always available, the best alternative is an estimate of the interference-plus-noise covariance matrix. A covariance estimate may be obtained through Monte Carlo simulation. By assembling K_r interference-plus-noise snapshots, the estimate of the covariance matrix is

$$\hat{\mathbf{R}}_u = \frac{1}{K_r} \sum^{K_r} \chi_u \chi_u^H. \tag{2.64}$$

2.3.5 Forming STAP weight vectors and measuring performance. The final goal of applying STAP algorithms is to create a vector of antenna element and pulse weights which steer the beam and null out interferers and noise. A number of methods to generate this weight vector exist. These methods vary in their robustness and subsequently, their computational intensity. The level of computational load for the various methods is directly related to the size of the problem solved in their weight generating algorithms.

Fully adaptive STAP generates the weight vector using the full dimensionality of the spatial and temporal vectors. It provides the best matched weight vector but levies the greatest computational requirements for processing. Partially adaptive STAP covers four different weight generation methods:

- Element-Space Pre-Doppler
- Element-Space Post-Doppler
- Beam-Space Pre-Doppler
- Beam-Space Post-Doppler.

These weight generation methods each employ some sub-dimensional technique. Methods which perform spatial filtering prior to adaptation (weight vector generation) are known as beam-space methods. Methods which perform temporal (Doppler) filtering prior to adaptation are known as post-Doppler methods. Either of these methods, applied separately or together, are designed to reduce the size of the weight generation problem in adaptive processing. Those methods which perform Doppler filtering using less than the full complement of M pulses after adaptation are known as pre-Doppler methods.

Regardless of their focus, STAP methods produce weight vectors through a variety of methods. The following sections examine the algorithms for developing the weight vectors in the Joint Domain Optimum (JDO) fully adaptive method and the Factored Time-Space (FTS) partially adaptive method. The vector formation algorithm is followed by a development of the signal-to-interference-plus noise ratio (SINR) performance measure.

2.3.5.1 Forming the weight vector. Adaptation results in the creation of a weight vector which steers the beam and nulls out noise and interferers. To meet this goal, the weight vector is generated, accounting for the target location and the statistics of the interference. The weight vector is calculated using

- the inteference-plus-noise covariance matrix $\mathbf{R}_u$
- the space-time steering vector $\mathbf{v}_s$.

The general concept in STAP processing is presented in the following text.

The $K \times MN$ projection matrix $\mathbf{T}$ transforms the full-dimension space-time snapshot of the interference-plus-noise into

$$\tilde{\chi}_u = \mathbf{T}^H \chi_u. \tag{2.65}$$

The resulting covariance matrix is

$$\begin{aligned}\tilde{\mathbf{R}}_u &= E[\tilde{\chi}_u \tilde{\chi}_u^H] \\ &= E[\mathbf{T}^H \chi_u \chi_u^H \mathbf{T}] \\ &= \mathbf{T}^H E[\chi_u \chi_u^H] \mathbf{T} \\ &= \mathbf{T}^H \mathbf{R}_u \mathbf{T}. \end{aligned} \tag{2.66}$$

Similarly, the covariance estimate is

$$\hat{\tilde{\mathbf{R}}}_u = \mathbf{T}^H \hat{\mathbf{R}}_u \mathbf{T}. \tag{2.67}$$

The new forms of the covariance matrices, $\tilde{\mathbf{R}}_u$ and $\hat{\tilde{\mathbf{R}}}_u$, are the results of a transformation into a lower-dimension space. In this lower-dimension space, adaptation may be performed with fewer computational steps. The K-length sub-dimensional steering vector is

$$\tilde{\mathbf{v}}_s = \mathbf{T}^H \mathbf{v}_s \tag{2.68}$$

$$= \tilde{\mathbf{b}}(\varpi_b) \otimes \tilde{\mathbf{a}}(\vartheta_s). \tag{2.69}$$

In the case of the fully adaptive STAP method known as Joint Domain Optimum (JDO), the projection matrix is simply

$$\mathbf{T} = \mathbf{I}_{MN}.$$

This projection matrix does not reduce the size of the covariance matrix or the steering vector.

The calculations to produce the full dimension weight vector $\mathbf{w}$ and the reduced dimension weight vector $\tilde{\mathbf{w}}$ are presented in detail in Sec. 2.3.5.3 and those following. However, the basic form used to generate the weight vector is

$$\tilde{\mathbf{w}} = \hat{\tilde{\mathbf{R}}}_u^{-1} \tilde{\mathbf{v}}_s. \tag{2.70}$$

The projection matrix $\mathbf{T}$ is used to transform the MN-size problem to a smaller K-size problem. The resulting weight vector $\tilde{\mathbf{w}}$ may be transformed into the MN-length vector $\mathbf{w}$ by reapplying $\mathbf{T}$. The full size weight vector is given by

$$\mathbf{w} = \mathbf{T}\tilde{\mathbf{w}}. \tag{2.71}$$

2.3.5.2 Measuring performance. The quality of the weight vector produced by any one of the STAP methods may be gauged using performance metrics. The most common performance metric is the signal-to-interference-plus-noise ratio (SINR). Just as the name states, this scalar statistical quantity represents the signal power captured with respect to the interference power and noise power captured. A measure of signal power captured to interference power and noise power captured is given by

$$\frac{P_t}{P_u} = \frac{E[|\mathbf{w}^H(\alpha_t \mathbf{v}_t)|^2]}{E[|\mathbf{w}^H \boldsymbol{\chi}_u|^2]}. \tag{2.72}$$

The general expression for the SINR of a non-random signal follows as

$$\begin{aligned}
\mathrm{SINR}(\vartheta, \varpi) &= E\left[\alpha_t^2 \frac{|\mathbf{w}^H \mathbf{v}(\vartheta, \varpi)|^2}{|\mathbf{w}^H \boldsymbol{\chi}_u|^2}\right] && (2.73)\\
&= \frac{\sigma^2 \xi_t E[|\mathbf{w}^H \mathbf{v}(\vartheta, \varpi)|^2]}{E[\mathbf{w}^H \boldsymbol{\chi}_u \boldsymbol{\chi}_u^H \mathbf{w}]} && (2.74)\\
&= \frac{\sigma^2 \xi_t |\mathbf{w}^H \mathbf{v}(\vartheta, \varpi)|^2}{\mathbf{w}^H E[\boldsymbol{\chi}_u \boldsymbol{\chi}_u^H] \mathbf{w}} && (2.75)\\
&= \frac{\sigma^2 \xi_t |\mathbf{w}^H \mathbf{v}(\vartheta, \varpi)|^2}{\mathbf{w}^H \mathbf{R}_u \mathbf{w}}. && (2.76)
\end{aligned}$$

The SINR expression may be used to establish the effectiveness of the weighting vector at pulling the signal from the return (numerator) and nulling the interference and noise (denominator). Since the target location in azimuth is usually known but its velocity is not, a common performance metric is to examine the SINR for various doppler frequencies at the target azimuth. The modified SINR expression is

$$\mathrm{SINR}(\varpi) = \frac{\sigma^2 \xi_t |\mathbf{w}^H \mathbf{v}(\vartheta_t, \varpi)|^2}{\mathbf{w}^H \mathbf{R}_u \mathbf{w}}. \tag{2.77}$$

A weight vector resulting in a large SINR implies that weight vector performs better in that interference environment than a weight vector yielding a smaller SINR. The expression for the SINR in the partially adaptive case is referenced by the output of the m^{th} Doppler composite weight vector $\mathbf{w}_m$ to give

$$\text{SINR}_m(\varpi) = \frac{\sigma^2 \xi_t |\mathbf{w}_m^H \mathbf{v}_t(\vartheta_t, \varpi)|^2}{\mathbf{w}_m^H \mathbf{R}_u \mathbf{w}_m}. \tag{2.78}$$

The total SINR for partially adaptive STAP is given by

$$\text{SINR}(\varpi) = \left[\frac{\sigma^2 \xi_t |\mathbf{w}_m^H \mathbf{v}_t(\vartheta_t, \varpi)|^2}{\mathbf{w}_m^H \mathbf{R}_u \mathbf{w}_m} \right]_{\text{max value of } m = 0, 1, \ldots, M-1}. \tag{2.79}$$

Here, the SINR at each Doppler frequency is taken as the output from the Doppler filter with the highest value at that Doppler.

Another common performance metric is the SINR Loss. The SINR Loss represents the loss in performance due to interference. The SINR Loss is given by

$$L_{SINR} = \frac{SINR(\varpi)}{SNR_0}. \tag{2.80}$$

The optimum signal-to-noise ratio (SNR) is used as a standard for comparison and is calculated by

$$SNR_0 = MN\xi_t. \tag{2.81}$$

This expression is derived from the full integration gain over space and time in full dimensional STAP. Figure 2.5 depicts the L_{SINR} plot for optimal, fully adaptive STAP. In this figure a new weight vector is formed to match the target signal at each Doppler frequency. This method is used to compute the SINR and L_{SINR} throughout this study. The result is good performance across all Doppler with heavy nulling at 0 Hz Doppler. This heavy nulling is directed at the clutter located over all azimuth at 0 Hz Doppler frequency.

2.3.5.3 Joint Domain Optimum (JDO) STAP. Joint Domain Optimum (JDO) STAP is a fully adaptive method which involves taking the product of the space-

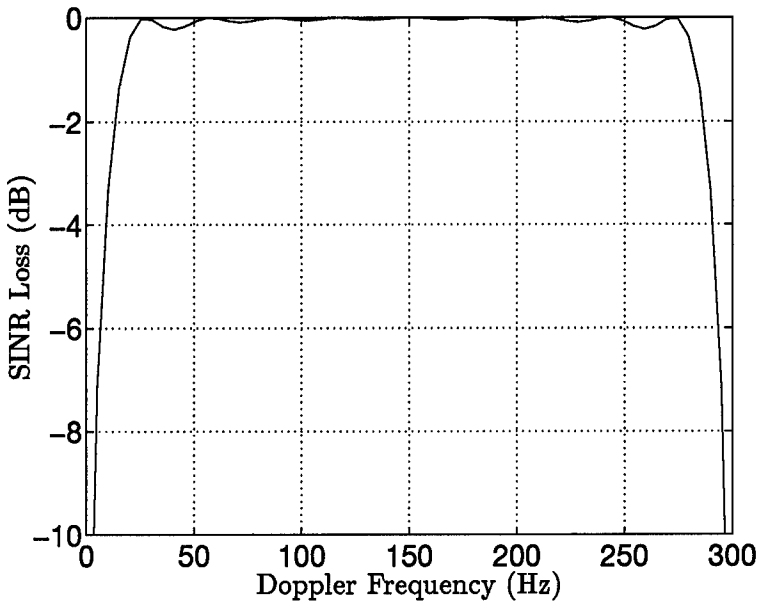

Figure 2.5 Baseline L_{SINR} for fully adaptive STAP. Processing performed on 32 antenna elements and 10 pulses.

time steering vector and the inverse of the full dimension undesired covariance matrix estimate. This product gives the MN-length weight vector,

$$\mathbf{w} = \hat{\mathbf{R}}_u^{-1}\mathbf{v}_s. \tag{2.82}$$

Figure 2.6 depicts the JDO scenario. Most antennas incorporate some sort of Doppler filter so this is shown in Fig. 2.6. The weighting scheme is created in the fully adaptive beamformer and the weights are applied to each pulse of each element in the return. It is the most computationally intensive STAP method but JDO offers the greatest accuracy in nulling and steering.

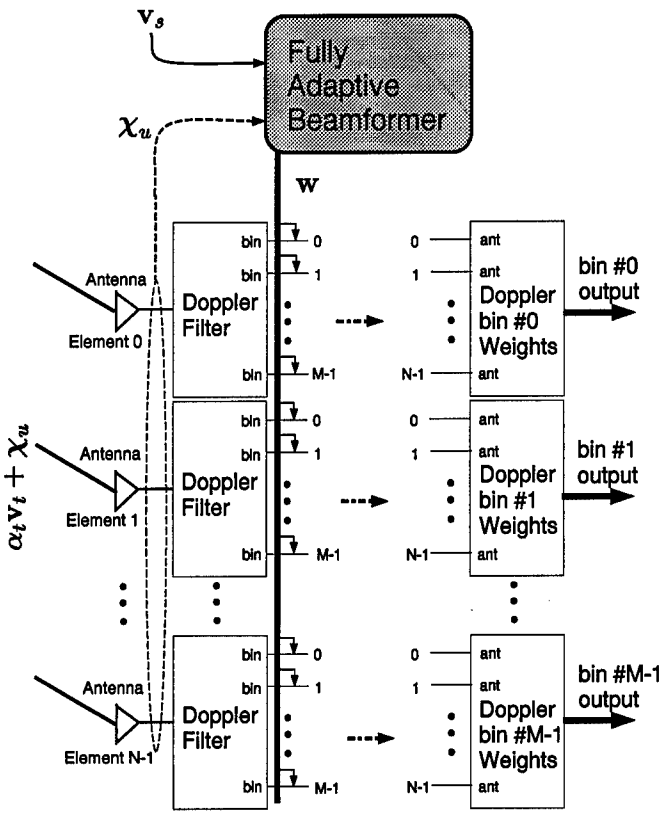

Figure 2.6 Joint Domain Optimum (JDO) system depiction. Weights are calculated for each combination of N antenna elements and M Doppler bins.

If the steering vector matches the target precisely, $\mathbf{v}_s = \mathbf{v}$, and the interference-plus-noise covariance estimate is very accurate, $\hat{\mathbf{R}}_u \simeq \mathbf{R}_u$, then the SINR simplifies to

$$\begin{aligned} \mathrm{SINR}_{opt}(\varpi) &= \frac{\sigma^2\xi_t|\mathbf{w}^H\mathbf{v}|}{\mathbf{w}^H\mathbf{R}_u\mathbf{w}} \\ &= \frac{\sigma^2\xi_t\mathbf{w}^H\mathbf{v}\mathbf{v}^H\mathbf{w}}{\mathbf{w}^H\mathbf{R}_u\mathbf{w}} \\ &= \frac{\sigma^2\xi_t\mathbf{v}^H\mathbf{R}_u^{-1}\mathbf{v}\mathbf{v}^H\mathbf{R}_u^{-1}\mathbf{v}}{\mathbf{v}^H\mathbf{R}_u^{-1}\mathbf{R}_u\mathbf{R}_u^{-1}\mathbf{v}} \\ &= \sigma^2\xi_t\mathbf{v}^H\mathbf{R}_u^{-1}\mathbf{v}. \end{aligned} \tag{2.83}$$

2.3.5.4 Factored Time-Space (FTS): element-space post-Doppler STAP. In element-space post-Doppler STAP, also known as Factored Time-Space (FTS), the Doppler filtering is performed prior to adaptation. So received signals on each antenna element are Doppler filtered independently, then the weighting scheme is applied.

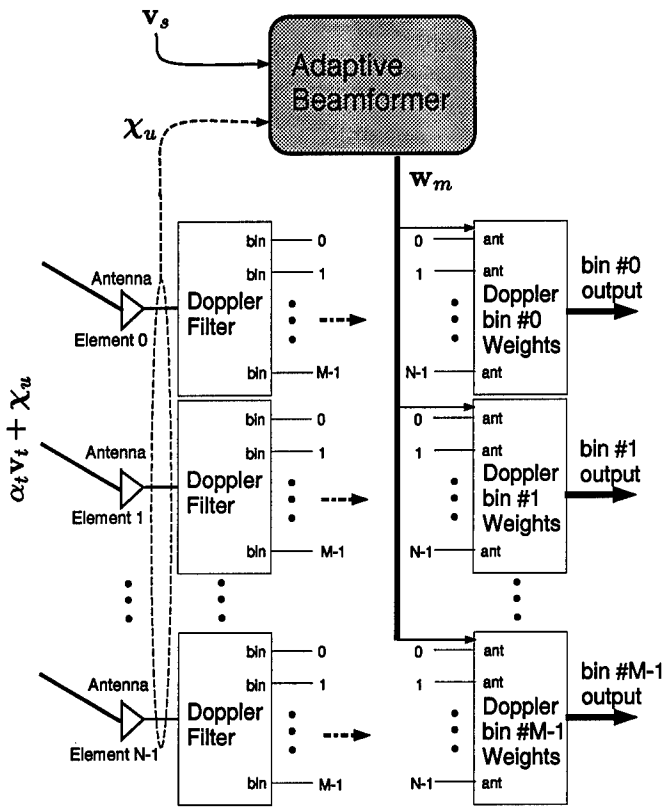

Figure 2.7 Factored Time-Space (FTS) system depiction. Weights are calculated and applied to all elements as factors applied to the output of each Doppler bin.

In FTS processing, Doppler filtering is done non-adaptively and identically on each element and then adaptive beamforming is performed. Figure 2.7 depicts the FTS algorithm. Here the partially adaptive scheme described below is used to form the weight vector. This weight vector is applied to a set of elements corresponding to each Doppler bin. The Doppler focus is no tighter than the resolution of the Doppler bins.

The $M \times M$ Doppler filter bank for FTS is

$$\begin{aligned} \mathbf{F} &= \text{diag}(\mathbf{t}_D)\mathbf{U}^* \\ &= [\mathbf{f}_0\ \mathbf{f}_1\ \ldots\ \mathbf{f}_{M-1}]. \end{aligned} \tag{2.84}$$

In this expression, $\mathbf{t}_D$ is an M-length vector taper and $\mathbf{U}^*$ is the $M \times M$ conjugate DFT matrix. From the columns of $\mathbf{F}$ the M projection matrices have the form

$$\mathbf{T}_m = (\mathbf{f}_m \otimes \mathbf{I}_N). \tag{2.85}$$

Each of these projection matrices may be used to form the components described in Eqns. (2.66) through (2.71):

- the reduced dimension space-time snapshot for the m^{th} Doppler bin is

$$\begin{aligned} \tilde{\boldsymbol{\chi}}_m &= \mathbf{T}_m^H \boldsymbol{\chi} \\ &= \mathbf{T}_m^H (\alpha_t \mathbf{v}_t) + \boldsymbol{\chi}_u \qquad (2.86) \\ &= \alpha_t \tilde{\mathbf{v}}_{tm} + \tilde{\boldsymbol{\chi}}_{um} \qquad (2.87) \end{aligned}$$

- the reduced dimension interference-plus-noise covariance matrix for the m^{th} Doppler bin is

$$\begin{aligned} \tilde{\mathbf{R}}_{um} &= \mathbf{T}_m^H \mathbf{R}_u \mathbf{T}_m \\ &= \mathbf{T}_m^H (\mathbf{R}_c + \mathbf{R}_n) \mathbf{T}_m \\ &= \mathbf{T}_m^H \mathbf{V}_c \boldsymbol{\Xi}_c \mathbf{V}_c^H \mathbf{T}_m + \sigma^2 \mathbf{f}_m^H \mathbf{f}_m \mathbf{I}_N. \qquad (2.88) \end{aligned}$$

- the m^{th} M-length weight vector is

$$\tilde{\mathbf{w}}_m = \tilde{\mathbf{R}}_{um}^{-1} \tilde{\mathbf{g}}_s, \tag{2.89}$$

  where $\tilde{\mathbf{g}}_s$ is the tapered spatial steering vector given by $\tilde{\mathbf{g}}_s = \mathbf{t}_a \odot \mathbf{a}_s$.

- the m^{th} Doppler composite weight vector is

$$\mathbf{w}_m = \mathbf{T}_m \tilde{\mathbf{w}}_m. \tag{2.90}$$

The SINR and L_{SINR} may be computed using expressions presented in Eqns. (2.79) through (2.80).

2.4 Summary

This chapter presents an overview of atmospheric turbulence principles and some important atmospheric turbulence statistical quantities. These quantities include the phase structure function D_S and the index of refraction structure constant C_n^2. Experimental C_n^2 values reported by other researchers are also presented.

The basic development of the STAP algorithms are also presented. The steering vectors and covariance matrices are derived. Two STAP methods are discussed: Joint Domain Optimum (JDO) and Factored Time-Space (FTS). The calculation of weight vectors and the measure of their performance via the SINR and L_{SINR} are also presented for JDO and FTS.

III. Theoretical Development

This chapter introduces the effects of atmospheric turbulence on STAP. The two STAP methods introduced in Sec. 2.3 are redeveloped for atmospheric turbulence effects. By examining the Joint Domain Optimum (JDO) STAP method, the overall effects of atmospheric turbulence may be investigated. By examining the Factored Time-Space (FTS) STAP method, the effects of atmospheric turbulence on a partially adaptive STAP method may also be realized.

Two forms of turbulence perturbations are considered in this chapter. The first form is known as Case I turbulence. Case I turbulence assumes the STAP processor has exact knowledge of the statistics of the interference environment. The primary statistic to represent the interference environment is the covariance matrix. Although the target radar return is affected by case I turbulence induced perturbations, the interference-plus-noise covariance matrix is unaffected beacuse it is assumed to be known and is not estimated from the data.

The second form of turbulence perturbation examines the effects of turbulence on a STAP processor at it estimates the interference environment. A processor of this type would sample the radar returns to generate statistics of the interference environment. In this situation, known as Case II turbulence, all radar returns received by the array are perturbed by similar turbulence. Consequently, both the target return (as in Case I turbulence) and the estimate of the interference environment will be skewed by the turbulence induced perturbations.

For Cases I and II turbulence in JDO and FTS processing, the same performance measures are used. These measures are the signal-to-interference-plus-noise ratio (SINR) and the SINR Loss (L_{SINR}) as introduced in Sec. 2.3. Throughout this chapter, the turbulence perturbations will lead to modifications in the SINR, representing the performance losses caused by the atmospheric turbulence induced perturbations.

3.1 Turbulence induced perturbations

This section introduces analytical expressions describing the effects of atmospheric turbulence on the primary STAP component. This component is the space-time steering vector, $\mathbf{v}_{obj}$. The subscript *obj* highlights the fact that radar energy reflected from any object in space is perturbed by these turbulence effects. The perturbations may occur on target returns, clutter returns, or it may occur on received energy from jammer sources. An understanding of the effects of turbulence on the space-time steering vector may be used to develop an understanding of the effects of turbulence on the STAP processing. These effects may be quantified by changes in the SINR and L_{SINR} quantities. As shown in Eqn. (2.80), the L_{SINR} is simply the SINR normalized by the optimal signal-to-noise ratio (SNR_o).

In Sec. 2.3.2.4 $\mathbf{v}_{obj}$ and its relationship to the space-time snapshot are introduced. The space-time snapshot $\boldsymbol{\chi}_l$ is made up of the M received signal pulses on each of the N antenna elements for the l^{th} range bin in space. The strength and direction of arrival of the radar return of an object are represented in $\boldsymbol{\chi}_l$. The strength of the radar return is given by the signal amplitude α_{obj} introduced in Sec. 2.3.2.5. The direction of arrival is given by the steering vector

$$\mathbf{v}_{obj} = \mathbf{b}_{obj} \otimes \mathbf{a}_{obj}, \tag{3.1}$$

where $\mathbf{b}_{obj}$ and $\mathbf{a}_{obj}$ are the temporal and spatial steering vectors, respectively.

If the receiving array encounters homogeneous, atmospheric turbulence, the EM wave will be perturbed as it passes through the disturbance. Just as $\mathbf{v}_{obj}$ is separable into temporal and spatial frequency components through the Kronecker product, the temporal and spatial phase perturbations are similarly separable. The perturbed steering vector is

$$\mathbf{v}'_{obj} = \mathbf{b}'_{obj} \otimes \mathbf{a}'_{obj}. \tag{3.2}$$

The perturbed steering vector is composed of the perturbed spatial steering vector $\mathbf{a}'_{obj}$, and the perturbed temporal steering vector $\mathbf{b}'_{obj}$.

3.1.1 The perturbed spatial steering vector. Atmospheric turbulence induces refractive index variations along the propagation path of the electromagnetic (EM) wave. These refractive index variations are manifested in a spatial phase perturbation. The perturbed spatial steering vector may be written as the unperturbed spatial steering vector with the phase perturbation applied. This relationship is conveyed by

$$\mathbf{a}'_{obj} = \mathbf{a}_{obj} \odot \boldsymbol{\phi}_s. \tag{3.3}$$

Here, $\boldsymbol{\phi}_s$ is the vector of complex values representing the phase perturbation of the EM wave along the length of the antenna array. This vector has N elements and appears as

$$\boldsymbol{\phi}_s = \begin{bmatrix} e^{j\psi_{s_0}} \\ e^{j\psi_{s_1}} \\ \vdots \\ e^{j\psi_{s_{N-1}}} \end{bmatrix}, \tag{3.4}$$

where ψ_{s_n} represents the instantaneous phase perturbation due to turbulence on the n^{th} antenna element. The instantaneous phase perturbation ψ_{s_n} is a random variable with second order statistics described by the phase structure function (D_S) presented in Sec. 2.2.3.

Combining the expressions given in Eqns. (3.3) and (3.4) leads to another representation of $\mathbf{a}'_{obj}$. This representation depicts the change introduced by the turbulence-induced phase perturbation on the spatial frequency and the spatial steering vector. This form of the perturbed spatial steering vector is

$$\mathbf{a}'_{obj} = \begin{bmatrix} e^{j[(0)2\pi\vartheta_{obj}+\psi_{s_0}]} \\ e^{j[(1)2\pi\vartheta_{obj}+\psi_{s_1}]} \\ \vdots \\ e^{j[(N-1)2\pi\vartheta_{obj}+\psi_{s_{N-1}}]} \end{bmatrix}, \tag{3.5}$$

where ϑ_{obj} is the spatial frequency of the object's return as defined in Eqn. (2.50).

3.1.2 The perturbed temporal steering vector. The perturbed temporal steering vector has a form similar to that of the perturbed spatial steering vector. Atmospheric turbulence may cause shifting of refractive indices as a function of time. In such cases, the perturbed temporal steering vector is

$$\mathbf{b}'_{obj} = \mathbf{b}_{obj} \odot \boldsymbol{\phi}_t. \tag{3.6}$$

In this case, the temporal steering vector, $\mathbf{b}_{obj}$, is perturbed by the vector of complex values $\boldsymbol{\phi}_t$ over the length of the CPI. This vector of values related to the phase perturbations is

$$\boldsymbol{\phi}_t = \begin{bmatrix} e^{j\psi_{t_0}} \\ e^{j\psi_{t_1}} \\ \vdots \\ e^{j\psi_{t_{M-1}}} \end{bmatrix}. \tag{3.7}$$

Here, ψ_{t_m} is a random variable representing the instantaneous phase perturbation due to turbulence on the m^{th} pulse of the CPI pulse train. The statistics of the random variable ψ_{t_m} are completely different from the statistics described by D_S which was defined for ψ_{s_n}. Since temporal perturbations are assumed to be negligible at radar frequencies, no further details are presented on $\boldsymbol{\phi}_t$.

The perturbed temporal steering vector may also be written as a vector of exponentials in much the same way as its spatial counterpart. Using the expressions given in Eqns. (3.6) and (3.7), this representation is written as

$$\mathbf{b}'_{obj} = \begin{bmatrix} e^{j[(0)2\pi\varpi_{obj}+\psi_{t_0}]} \\ e^{j[(1)2\pi\varpi_{obj}+\psi_{t_1}]} \\ \vdots \\ e^{j[(M-1)2\pi\varpi_{obj}+\psi_{t_{M-1}}]} \end{bmatrix}, \tag{3.8}$$

where ϖ_{obj} is the normalized Doppler frequency of the object's return. Once again, this form shows there is some change introduced to the measurement of the object's Doppler frequency by significant phase perturbations in $\boldsymbol{\phi}_t$.

3.1.3 The perturbed space-time steering vector. As Eqn. (3.2) shows, the perturbed space-time steering vector is a function of the perturbed spatial steering vector and the perturbed temporal steering vector. Using the above relations, the perturbed space-time steering vector becomes

$$\begin{aligned} \mathbf{v}'_{obj} &= \mathbf{b}'_{obj} \otimes \mathbf{a}'_{obj} \\ &= (\mathbf{b}_{obj} \odot \boldsymbol{\phi}_t) \otimes (\mathbf{a}_{obj} \odot \boldsymbol{\phi}_s) \\ &= (\mathbf{b} \otimes \mathbf{a}) \odot (\boldsymbol{\phi}_t \otimes \boldsymbol{\phi}_s). \end{aligned} \tag{3.9}$$

By substituting

$$\boldsymbol{\phi}_{st} = \boldsymbol{\phi}_t \otimes \boldsymbol{\phi}_s \tag{3.10}$$

as the vector of space-time phase perturbations, a new expression for the perturbed space-time steering vector is formed. This expression is

$$\mathbf{v}'_{obj} = \mathbf{v}_{obj} \odot \boldsymbol{\phi}_{st}. \tag{3.11}$$

Just as in the previously discussed cases, $\boldsymbol{\phi}_{st}$ is a vector of random variables representing instantaneous spatial and temporal phase perturbations.

3.1.4 The space-time steering vector outer product. In computations to form the interference-plus-noise covariance matrix and the SINR, it is necessary to compute the outer product of the space-time steering vector with itself. In the case of a perturbed space-time steering vector, this outer product takes a special form. The perturbed space-time steering vector outer product is

$$\begin{aligned} \mathbf{v}'_{obj}\mathbf{v}'^{H}_{obj} &= (\mathbf{v}_{obj} \odot \boldsymbol{\phi}_{st})(\mathbf{v}_{obj} \odot \boldsymbol{\phi}_{st})^H \\ &= (\mathbf{v}_{obj} \odot \boldsymbol{\phi}_{st})(\mathbf{v}^H_{obj} \odot \boldsymbol{\phi}^H_{st}) \\ &= \mathbf{v}_{obj}\mathbf{v}^H_{obj} \odot \boldsymbol{\phi}_{st}\boldsymbol{\phi}^H_{st}. \end{aligned} \tag{3.12}$$

The outer product shown here becomes the unperturbed steering vector outer product weighted by the instantaneous space-time phase perturbation outer product.

3.2 Case I: Target Return Perturbed, Known Interference Environment

This section investigates the effects of turbulence perturbations on the target return. If the weight vector is formed without accounting for these effects, the steered beam will not match the target return precisely. The SINR introduced in Sec. 2.3.5 may be used as a measure of the suitability of the weight vector to a specific target return. In this section, the effects of the turbulence perturbation on the target return are quantified in terms of the SINR. This section investigates both JDO and FTS methods.

In this development for Case I turbulence, it is assumed the covariance matrix used to form the weight vector is known. To focus on the turbulence problem at hand, it is assumed that this interference environment consists only of clutter. Therefore, the statistics of the undesired environment are described by

$$\mathbf{R}_u = \mathbf{R}_n + \mathbf{R}_c.$$

It is also assumed that the target location, (ϑ_t, ϖ_t) is known. With this knowledge, the desired steering vector is formed as $\mathbf{v}_s = \mathbf{v}_t$.

3.2.1 Case I turbulence effects on JDO. Equation (2.82) gives the expression to form the weight vector for the JDO algorithm. This expression is repeated here:

$$\mathbf{w} = \mathbf{R}_u^{-1}\mathbf{v}_t. \tag{3.13}$$

Figure 3.1 depicts the JDO algorithm under Case I turbulence.

The general statistical expression for the JDO SINR is described by Eqn. (2.73) as

$$\mathrm{SINR}_{JDO}(\varpi) = E\left[\frac{|\alpha_t|^2 \mathbf{w}^H \mathbf{v}_t(\varpi)\mathbf{v}_t^H(\varpi)\mathbf{w}}{\mathbf{w}^H \boldsymbol{\chi}_u \boldsymbol{\chi}_u^H \mathbf{w}}\right], \tag{3.14}$$

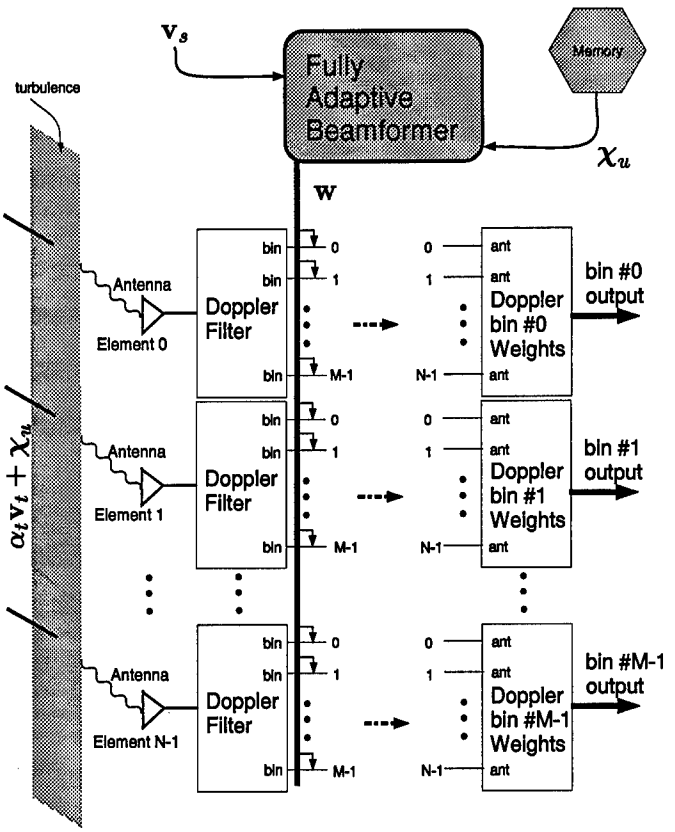

Figure 3.1 Joint Domain Optimum processor under case I turbulence: target return perturbed; interference known. $\mathbf{v}_s$ and $\mathbf{R}_u$ are known.

where α_t is the signal amplitude and χ_u is the interference-plus-noise space-time snapshot. In this expression, the form of the target space-time steering vector is $\mathbf{v}_t(\varpi) = \mathbf{v}(\vartheta_t, \varpi)$. This notation describes the return steering vector for the target located at azimuth ϑ_t as a function of normalized Doppler ϖ. If the normalized target Doppler frequency is fixed at ϖ_t, the return steering vector may also be written as $\mathbf{v}_t = \mathbf{v}(\vartheta_t, \varpi_t)$.

The performance of the receiver degrades if the phase of $\mathbf{v}_t$ is perturbed while the signal propagates over the array. Performance degradation is quantified by a decrease in the SINR value. Since STAP involves integration over both space and time, both temporal and spatial phase fluctuations can lead to a degradation in receiver performance. However, as mentioned in Sec. 2.2.2, spatial phase fluctuations are of much higher frequency and magnitude than temporal phase fluctations. Now, consider the effects of a spatial phase perturbation on the receiver performance. Recall the linear array presented in Fig. 2.2.

Such a perturbation would change the expected phase difference of the propagating wave between any two points on the array. Consider antenna elements #1 and #2 as an example. If the spatial phase difference of the propagating wave at these locations is not matched to the phase weight difference between these elements, the resulting SINR will be less than in the optimal case described by Eqn. (2.83). The sub-optimal SINR is to be expected since the integration of the signal power over these elements will be less than in the optimal case. The inner product of $\mathbf{w}$ and $\mathbf{v}_t$ in the numerator of the SINR expression summarizes the integration over the elements and pulses. The inner product may be written as

$$\mathbf{w}^H \mathbf{v}_t = \sum_{i=1}^{MN} \mathbf{w}^*(i)\mathbf{v}_t(i), \tag{3.15}$$

where $\mathbf{w}(i)$ and $\mathbf{v}_t(i)$ are the i^{th} elements of the weight and steering vectors, respectively. Figures 3.2 and 3.3 depict the resulting integration for a system where $\mathbf{w}$ and $\mathbf{v}_t$ each have two complex elements. In Fig. 3.2, the phase on the antenna element and that on the received signal sample are matched. Subsequently, the graphical summation leading to the output value is $y_0 = |\mathbf{w}^*(0)\mathbf{v}_t(0) + \mathbf{w}^*(1)\mathbf{v}_t(1)|$. In the case of the perturbed return $\mathbf{v}_t'$ the output value is $y_0' = |\mathbf{w}^*(0)\mathbf{v}_t'(0) + \mathbf{w}^*(1)\mathbf{v}_t'(1)|$. It is evident from these figures that the magnitude of y_0' will always be less than or equal to the magnitude of y_0. This result holds true for $\mathbf{v}_t$ and $\mathbf{w}$ of any length.

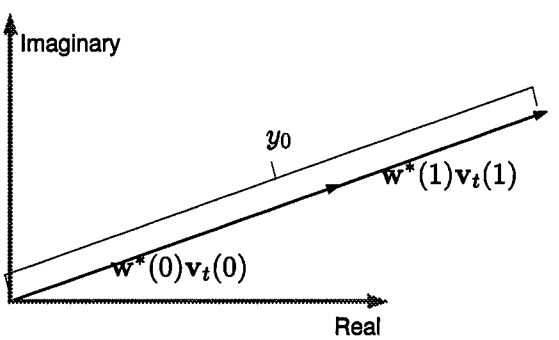

Figure 3.2 Geometric depiction in complex plane of two element inner product of weight vector with target return vector described in Eqn. (3.15). The first complex valued element of the summation is $\mathbf{w}^*(0)\mathbf{v}_t(0)$. The second complex valued element of the summation is $\mathbf{w}^*(1)\mathbf{v}_t(1)$. y_0 is the length of the resultant vector. In the unperturbed case they sum in phase, yielding y_0 a the magnitude of the output.

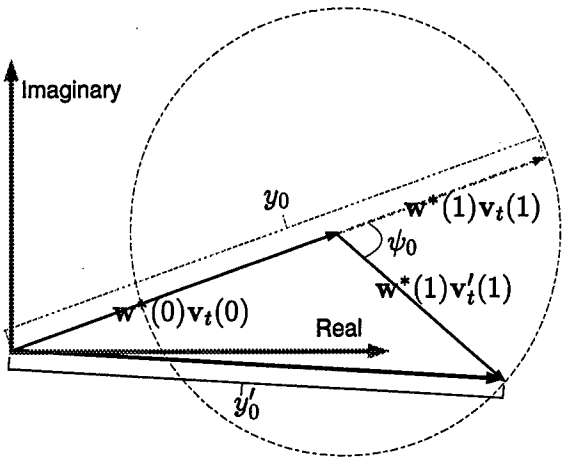

Figure 3.3 Geometric depiction in complex plane of weight vector from Fig. 3.2 and the perturbed space-time steering return. The phase difference due to the perturbation is ψ_0. The magnitude of the output value is y'_0. The dotted circle represents the possible locations of the $\mathbf{w}^H\mathbf{v}_t$ resultant given some unknown phase perturbation. For all points on the circle: $y_0 \geq y_0{}'$.

Equation (3.11) describes the turbulence perturbed space-time steering vector return as $\mathbf{v}'_t$. The effect of Case I turbulence on the receiver performance is seen by inserting $\mathbf{v}'_t$ into the expression for the SINR presented in Eqn. (3.14). This expression for the system performance, with the target return perturbation is

$$\begin{aligned} \text{SINR}'_{JDO} &= E\left[\frac{|\alpha_t|^2 \mathbf{w}^H \mathbf{v}'_t \mathbf{v}'^H_t \mathbf{w}}{\mathbf{w}^H \boldsymbol{\chi}_u \boldsymbol{\chi}_u^H \mathbf{w}}\right] \\ &= \frac{\sigma^2 \xi_t \mathbf{w}^H E[\mathbf{v}'_t \mathbf{v}'^H_t] \mathbf{w}}{\mathbf{w}^H \mathbf{R}_u \mathbf{w}}, \end{aligned} \tag{3.16}$$

where σ^2 is the noise power and ξ_t is the target signal-to-noise ratio. The SINR quantity involves the outer product of the return space-time steering vector, $\mathbf{v}'_t\mathbf{v}'^H_t$. Section 3.1.4 describes the result of taking the outer product of $\mathbf{v}'_t$. Equation (3.12) from Sec. 3.1.4 allows a simplified SINR expression. The expression for the perturbed SINR becomes

$$\text{SINR}'_{JDO} = \frac{\sigma^2 \xi_t \mathbf{w}^H E[(\mathbf{v}_t \mathbf{v}_t^H \odot \boldsymbol{\phi}_{st} \boldsymbol{\phi}_{st}^H)] \mathbf{w}}{\mathbf{w}^H \mathbf{R}_u \mathbf{w}} \tag{3.17}$$

$$= \frac{\sigma^2 \xi_t \mathbf{w}^H (\mathbf{v}_t \mathbf{v}_t^H \odot E[\boldsymbol{\phi}_{st} \boldsymbol{\phi}_{st}^H]) \mathbf{w}}{\mathbf{w}^H \mathbf{R}_u \mathbf{w}}. \tag{3.18}$$

From Figs. 3.2 and 3.3 and the corresponding discussion, it is obvious the SINR is affected by the perturbations on the target return. The inclusion of the phase perturbations on the target return disrupt the matching between the return steering and weight vectors. The greater the phase perturbations, the greater the mismatch and the smaller the output power. Keeping this in mind, Eqn. (3.18) demonstrates that the numerator of the SINR with the target return perturbation will be a smaller quantity than the numerator of the unperturbed SINR in Eqn. (3.14).

To further demonstrate the relationship between SINR_{opt} and SINR'_{JDO}, examine Eqn. (2.83). It demonstrates that the optimal SINR is

$$\begin{aligned} \text{SINR}_{opt} &= \frac{\sigma^2 \xi_t \mathbf{v}_t^H \mathbf{R}_u^{-1} \mathbf{v}_t \mathbf{v}_t^H \mathbf{R}_u^{-1} \mathbf{v}_t}{\mathbf{v}_t^H \mathbf{R}_u^{-1} \mathbf{v}_t} && (3.19) \\ &= \sigma^2 \xi_t \mathbf{v}_t^H \mathbf{R}_u^{-1} \mathbf{v}_t. && (3.20) \end{aligned}$$

$SINR_{opt}$ is achieved by applying $\mathbf{w}$ in a turbulence-free environment. Substituting the optimal weight vector into Eqn. (3.18) results in a perturbed SINR. This expression is

$$\begin{aligned} \text{SINR}'_{JDO} &= \frac{\sigma^2 \xi_t \mathbf{w}^H (\mathbf{v}_t \mathbf{v}_t^H \odot E[\boldsymbol{\phi}_{st} \boldsymbol{\phi}_{st}^H]) \mathbf{w}}{\mathbf{w}^H \mathbf{R}_u \mathbf{w}} \\ &= \frac{\sigma^2 \xi_t \mathbf{v}_t^H \mathbf{R}_u^{-1} (\mathbf{v}_t \mathbf{v}_t^H \odot E[\boldsymbol{\phi}_{st} \boldsymbol{\phi}_{st}^H]) \mathbf{R}_u^{-1} \mathbf{v}_t}{\mathbf{v}_t^H \mathbf{R}_u^{-1} \mathbf{R}_u \mathbf{R}_u^{-1} \mathbf{v}_t} \\ &= \frac{\sigma^2 \xi_t \mathbf{v}_t^H \mathbf{R}_u^{-1} (\mathbf{v}_t \mathbf{v}_t^H \odot E[\boldsymbol{\phi}_{st} \boldsymbol{\phi}_{st}^H]) \mathbf{R}_u^{-1} \mathbf{v}_t}{\mathbf{v}_t^H \mathbf{R}_u^{-1} \mathbf{v}_t}. && (3.21) \end{aligned}$$

The expressions in the denominator of Eqns. (3.19) and (3.21) are identical. There is no change expected in the denominator since in this situation, the turbulence induced perturbations do not affect the weight vector. In the case of the numerator of Eqn. (3.21), Fig. (3.3) demonstrates the result of a mismatched weight between the phases of $\mathbf{w}$ and $\mathbf{v}'_t$.

Case I turbulence has an effect under all manners of STAP processing. FTS algorithms include a sub-dimensional adaptive method. FTS also sees some degradation in performance due to atmospheric turbulence effects.

3.2.2 Case I turbulence effects on Factored Time-Space (FTS). Section 2.3.5.4 contains information on the FTS processing algorithm. Under this method, the radar returns on each antenna element are Doppler filtered prior to the formation of the adaptive weight vector. Figure 3.4 depicts the FTS system in the Case I turbulent environment. Case I turbulence does not affect the estimate of $\mathbf{R}_u$ so there is no change in the formation of the weight vectors.

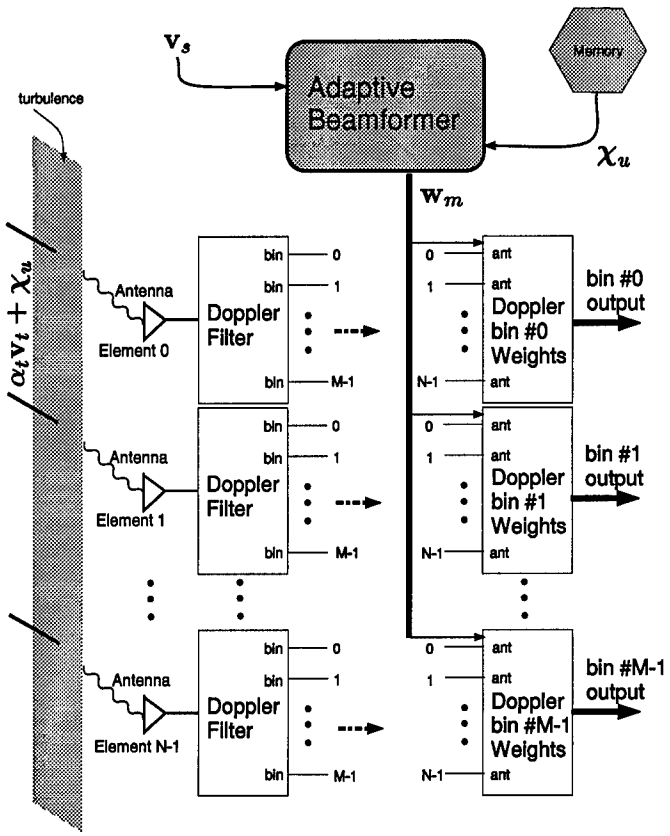

Figure 3.4 Factored Time-Space processor under case I turbulence: target return perturbed; interference known. $\mathbf{v}_s$ and $\mathbf{R}_u$ are known.

However, Case I turbulence does perturb the target return. Just as in the JDO algorithm, the effect of the turbulence perturbation on the return may be seen in the SINR. Equation (2.79) introduces the SINR for FTS as

$$\text{SINR}_{FTS} = \left[\frac{\sigma^2 \xi_t |\mathbf{w}_m^H \mathbf{v}_t|^2}{\mathbf{w}_m^H \mathbf{R}_u \mathbf{w}_m} \right]_{\text{max value of } m = 0,1,\ldots,M-1},$$

where $\mathbf{w}_m$ is the m^{th} composite weight vector formed from FTS adaption after the m^{th} Doppler filter. Expanding this expression into a form similar to Eqn. (3.18) transforms the SINR for FTS into

$$\text{SINR}'_{FTS} = \left[\frac{\sigma^2 \xi_t \mathbf{w}_m^H (\mathbf{v}_t \mathbf{v}_t^H \odot E[\boldsymbol{\phi}_{st} \boldsymbol{\phi}_{st}^H]) \mathbf{w}_m}{\mathbf{w}_m^H \mathbf{R}_u \mathbf{w}_m} \right]_{\text{max value of } m = 0, 1, \ldots, M-1} . \quad (3.22)$$

Just as in the JDO development for Case I turbulence, the denominator is unchanged by the turbulence. The numerator, however, demonstrates a similar type of degradation to that described in the JDO development. In the case of FTS, $\mathbf{w}_m$ is formed from a sub-dimensional projection of $\mathbf{R}_u$. Full spatial dimensionality is retained and the entire spatial steering vector $\mathbf{a}_s$ is tapered and used to form $\mathbf{w}_m$.

Turbulence induced EM wave phase perturbations occur mainly in reference to distances in space. As shown in Sec. 2.2.2, temporal phase perturbations are minimal. The FTS method retains full spatial adaptivity but employs Doppler filtering on each of these spatial channels. This filtering results in an acknowledged performance degradation. Therefore the SINR for unperturbed FTS is lower over all Doppler than the SINR for unperturbed JDO. The greatest turbulence-induced phase perturbations occur in the spatial domain while FTS processing does not reduce the size of the problem in the spatial dimension. Therefore, the additional degradation due to turbulence effects should be very close to that seen in JDO. FTS sacrifices SINR performance for a computational advantage through reduced dimensionality. The loss in performance due to turbulence effects should be no greater in FTS than in JDO since turbulence effects are limited to spatial fluctuations.

It is to be expected that the SINR for both JDO and FTS would be further degraded if the interference-plus-noise covariance matrix estimate, $\hat{\mathbf{R}}_u$, were formed using perturbed clutter returns. In this case, $\hat{\mathbf{R}}_u \neq \mathbf{R}_u$. Forming a weight vector using an estimate in an environment where both interference and target returns are perturbed by atmospheric turbulence has performance consequences. The next section includes an investigation into the performance consequences of Case II turbulence effects on JDO and FTS processing methods. The performance is once again quantified in the SINR.

3.3 *Case II: Target Return Perturbed, Interference Estimate Perturbed*

In the previous section, the undesired covariance matrix estimate is known but the target return is perturbed. In this section, both the target return and the estimate of the interference-plus-noise covariance matrix are perturbed. This is known as Case II turbulence. The SINR is still used as a measure of the system performance.

It is once again assumed that the target location (ϑ_t, ϖ_t) is known. Consequently, the desired steering vector is $\mathbf{v}_s = \mathbf{v}_t$. In this case, however, the interference-plus-noise covariance estimate is not necessarily accurate. The interference-plus-noise covariance estimate is formed from perturbed interference returns. From Eqn. (2.82) the JDO weight vector, without turbulence effects, is

$$\mathbf{w} = \hat{\mathbf{R}}_u^{-1}\mathbf{v}_t. \tag{3.23}$$

To understand the effects of the turbulence perturbations on the system performance, the effects on the undesired covariance matrix estimate must be understood. Since the receiver noise is assumed to be uncorrelated among pulses and elements, the form of $\mathbf{R}_n$ is known. Once again, to simplify the development, the interference is assumed to consist purely of clutter returns. The interference-plus-noise covariance estimate follows the format for $\mathbf{R}_u$ defined in Eqn. (2.57). This format is

$$\hat{\mathbf{R}}_u = \hat{\mathbf{R}}_c + \mathbf{R}_n, \tag{3.24}$$

where $\hat{\mathbf{R}}_c$ is the estimate of the clutter covariance matrix and $\mathbf{R}_n$ is the receiver noise covariance matrix. The statistics of the receiver noise are unaffected by turbulence so the only ambiguity in the estimate of the perturbed interference-plus-nois covariance matrix is due to the turbulence perturbations on the clutter returns. The estimate of the perturbed interference-plus-noise covariance matrix follows as

$$\hat{\mathbf{R}}'_u = \hat{\mathbf{R}}'_c + \mathbf{R}_n. \tag{3.25}$$

The quantity $\hat{\mathbf{R}}_c'$ may be derived from the expression for $\mathbf{R}_c$ introduced in Eqn. (2.59). This equation describes the formation of the clutter covariance matrix as

$$\mathbf{R}_c = E[\chi_c \chi_c^H].$$

Assuming that the clutter returns are independent identically distributed (iid) brings about the modified form

$$\begin{aligned} \mathbf{R}_c &= \sigma^2 \sum_{cp=1}^{N_c} \xi_{cp} \mathbf{v}_{cp} \mathbf{v}_{cp}^H \\ &= \sigma^2 \sum_{cp=1}^{N_c} \xi_{cp} (\mathbf{b}_{cp} \mathbf{b}_{cp}^H) \otimes (\mathbf{a}_{cp} \mathbf{a}_{cp}^H). \end{aligned}$$

where N_c is the number of clutter patches, ξ_{cp} is the signal-to-noise ratio for the cp^{th} clutter patch and $\mathbf{b}_{cp}$, $\mathbf{a}_{cp}$, and $\mathbf{v}_{cp}$ are the temporal, spatial, and space-time steering vectors for the cp^{th} clutter patch.

Incorporating the turbulence effects described in Sec. 3.1 produces a new form of the covariance matrix. This form is

$$\mathbf{R}_c' = E[\chi_c' \chi_c'^H]. \tag{3.26}$$

Estimating $\mathbf{R}_c'$ is a primary concern. Two methods may be used. The first uses the Monte Carlo method introduced in Eqn. (2.64). The second method relies on incorporating the statistics of the turbulence induced phase perturbation onto the clutter covariance estimate.

3.3.1 Perturbed clutter covariance estimate formed by Monte Carlo method. An estimate of the clutter covariance matrix may be formed using the Monte Carlo method introduced in Eqn. (2.64). In this expression, the estimate of the covariance matrix is formed to represent the randomness in the clutter returns. To form the covariance estimate, K_r realizations of the space-time snapshot are used. In this situation, it is assumed the significant contribution to the randomness in the clutter returns is due to

the atmospheric turbulence perturbations ϕ_{st}. Therefore, the estimate may be formed by using T realizations of the clutter return received through the turbulent atmosphere. The estimate has the form

$$\hat{\mathbf{R}}'_c = \frac{1}{T}\sum_{l=1}^{T} \chi'_{c_l}\chi'^{H}_{c_l}. \tag{3.27}$$

The l^{th} space-time snapshot of the clutter return received through the turbulent atmosphere is given by χ'_{c_l}. Once again, the accuracy of the estimate is tied directly to the size of T. For a dependable covariance estimate, T should be twice the number of degrees of freedom (DOF). For STAP, the DOF equals the product of the number of antenna elements and the number of pulses. The rank of $\mathbf{R}_u$ is MN so $2MN$ realizations may be used to form $\hat{\mathbf{R}}_u$. Similarly, the number of realizations of the perturbed clutter returns needed to form $\hat{\mathbf{R}}_c$ is

$$T = 2 \times \text{rank}[\mathbf{R}'_c]. \tag{3.28}$$

Substituting the description given in Eqn. (2.59) for χ_{c_l} gives

$$\mathbf{R}'_c = E\left[\sum_{cp1_l=1}^{N_c}\sum_{cp2_l=1}^{N_c} \alpha_{cp1_l}\mathbf{v}'_{cp1_l}\alpha_{cp2_l}\mathbf{v}'^{H}_{cp2_l}\right]. \tag{3.29}$$

Assuming the clutter returns and the turbulence induced perturbations are uncorrelated from azimuth bin to azimuth bin results in the simplified expression

$$\hat{\mathbf{R}}'_c = \frac{\sigma^2}{T}\sum_{l=1}^{T}\left\{\sum_{cp_l=1}^{N_c} \xi_{cp_l}\mathbf{v}'_{cp_l}\mathbf{v}'^{H}_{cp_l}\right\}. \tag{3.30}$$

Introducing the outer product of the perturbed space-time steering vector from Eqn. (3.12) gives the estimate the form

$$\hat{\mathbf{R}}'_c = \frac{\sigma^2}{T}\sum_{l=1}^{T}\left\{\sum_{cp_l=1}^{N_c} \xi_{cp_l}(\mathbf{v}_{cp_l}\mathbf{v}^{H}_{cp_l} \odot \phi_{st_{cp_l}}\phi^{H}_{st_{cp_l}})\right\}, \tag{3.31}$$

where $\phi_{st_{cp_l}}$ is the space-time phase perturbation for the l^{th} sample of the clutter patch in the cp^{th} azimuth bin.

Forming an accurate covariance estimate is an arduous task. Performing the operations described above T times is very processor intensive. A less intensive method is described in the following text. The method described in the following text uses a statistical representation of the turbulence to form the covariance estimate. Using a statistical representation of the turbulence renders the Monte Carlo method of estimation unnecessary. The resulting processing requirements are lessened and the resulting clutter covariance estimate is statistically accurate.

3.3.2 Perturbed clutter covariance estimate formed by statistical representations. Equation (3.26) describes the perturbed clutter covariance matrix in its statistical form. By staying mindful of the statistical properties of the elements which form the clutter covariance, an accurate clutter covariance matrix may be formed.

Substituting the expression for the clutter space-time snapshot from Eqn. (2.59) into Eqn. (3.26) gives

$$\begin{aligned} \mathbf{R}'_c &= E[\chi'_c \chi'^H_c] \\ &= E\left[\sum_{cp1=1}^{N_c}\sum_{cp2=1}^{N_c} \alpha_{cp1}\mathbf{v}'_{cp1}\alpha_{cp2}\mathbf{v}'^H_{cp2}\right]. \end{aligned} \tag{3.32}$$

Once again, the assumption is made that the clutter returns and the turbulence perturbations are independent among azimuth bins. The expression for the perturbed clutter covariance becomes

$$\mathbf{R}'_c = E\left[\sum_{cp=1}^{N_c} \xi_{cp}\mathbf{v}'_{cp}\mathbf{v}'^H_{cp}\right]. \tag{3.33}$$

Including the expression for the outer product of the perturbed space-time steering vector introduced in Eqn. (3.12) further changes the expression of the perturbed clutter covari-

ance. This new expression is

$$\mathbf{R}_c' = E\left[\sum_{cp=1}^{N_c} \xi_{cp}(\mathbf{v}_{cp}\mathbf{v}_{cp}^H \odot \boldsymbol{\phi}_{st_{cp}}\boldsymbol{\phi}_{st_{cp}}^H)\right]. \tag{3.34}$$

Assuming the unperturbed clutter returns are deterministic values allows the expected value operator to be moved within to form

$$\begin{aligned}\mathbf{R}_c' &= \sum_{cp=1}^{N_c} \xi_{cp} E[(\mathbf{v}_{cp}\mathbf{v}_{cp}^H \odot \boldsymbol{\phi}_{st_{cp}}\boldsymbol{\phi}_{st_{cp}}^H)] &(3.35)\\ &= \sum_{cp=1}^{N_c} \xi_{cp}(\mathbf{v}_{cp}\mathbf{v}_{cp}^H \odot E[\boldsymbol{\phi}_{st_{cp}}\boldsymbol{\phi}_{st_{cp}}^H]). &(3.36)\end{aligned}$$

Since the turbulence perturbations are independent from azimuth bin to azimuth bin, the expression for the clutter covariance matrix further simplifies to

$$\mathbf{R}_c' = \sum_{cp=1}^{N_c} \xi_{cp}\mathbf{v}_{cp}\mathbf{v}_{cp}^H \odot E[\boldsymbol{\phi}_{st}\boldsymbol{\phi}_{st}^H]. \tag{3.37}$$

Recall the phase structure function introduced in Eqn. (2.11). The expression

$$\mathbf{D}_{st} = E[\boldsymbol{\phi}_{st}\boldsymbol{\phi}_{st}^H] \tag{3.38}$$

is related to the phase structure function and is called the space-time perturbation matrix. The estimate of the clutter covariance matrix follows as

$$\begin{aligned}\hat{\mathbf{R}}_c' &= \sum_{cp=1}^{N_c} \xi_{cp}\mathbf{v}_{cp}\mathbf{v}_{cp}^H \odot \mathbf{D}_{st}\\ &= \mathbf{R}_c \odot \mathbf{D}_{st}. &(3.39)\end{aligned}$$

Computing the unperturbed clutter covariance matrix and deriving an accurate representation of the phase structure function for the turbulence at hand gives a statistically accurate estimate of the perturbed clutter covariance matrix. With this estimate, the effect of turbulence on system performance may be seen in the SINR. The Case II turbulence effects on JDO and FTS are presented in the following two sections.

3.3.3 Case II turbulence effects on the SINR. The expressions derived above may be applied to the calculations used to form the SINR. In this way, the effect of turbulence on the system performance may be expressed analytically.

Once $\hat{\mathbf{R}}'_c$ is formed, the estimate of the perturbed undesired covariance matrix, $\hat{\mathbf{R}}'_u$, may be formed. Equation (3.25) defines $\hat{\mathbf{R}}'_u$ as

$$\hat{\mathbf{R}}'_u = \hat{\mathbf{R}}'_c + \mathbf{R}_n.$$

For Case II turbulence, $\hat{\mathbf{R}}'_u$ becomes

$$\hat{\mathbf{R}}'_u = (\mathbf{R}_c \odot \mathbf{D}_{st}) + \mathbf{R}_n. \tag{3.40}$$

Using $\hat{\mathbf{R}}'_u$, expressions may be formed for the SINR in various STAP methods. The next two sections examine JDO and FTS under Case II turbulence conditions.

3.3.4 Case II turbulence effects on Joint Domain Optimum. The weight vector is formed using the expression in Eqn. (2.82). This expression is

$$\begin{aligned} \mathbf{w} &= \hat{\mathbf{R}}_u^{-1}\mathbf{v}_s \\ &= \hat{\mathbf{R}}_u^{-1}\mathbf{v}_t. \end{aligned}$$

The weight vector formed in the presence of Case II turbulence follows as

$$\begin{aligned} \mathbf{w}' &= \hat{\mathbf{R}}_u'^{-1}\mathbf{v}_t \\ &= \{(\mathbf{R}_c \odot \mathbf{D}_{st}) + \mathbf{R}_n\}^{-1}\mathbf{v}_t. \end{aligned} \tag{3.41}$$

Figure 3.5 depicts the JDO algorithm under Case II turbulence.

Equation (3.18) shows the effect of a perturbed target return in terms of the SINR'_{JDO}. For Case II turbulence, both the target return and the undesired covariance estimate are

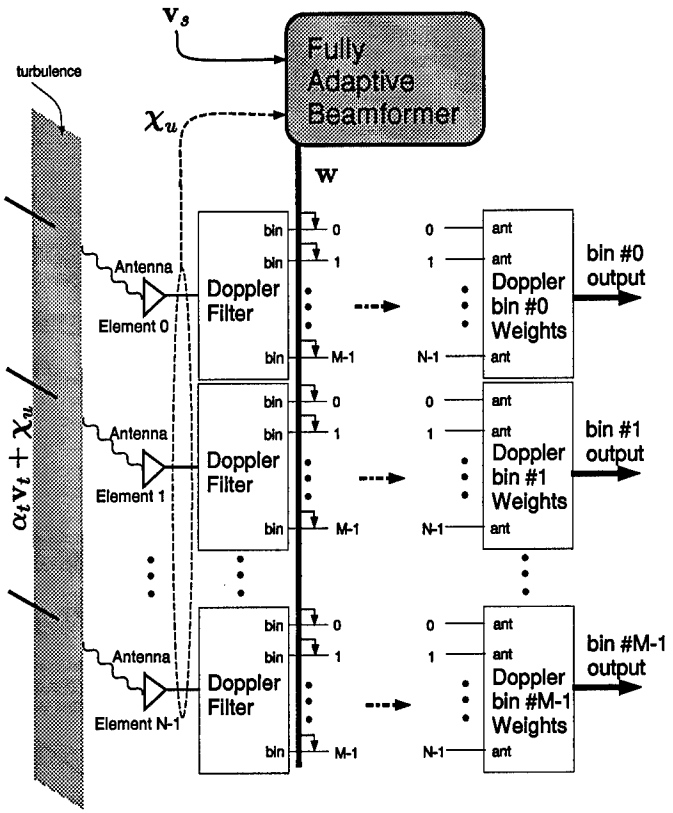

Figure 3.5 Joint Domain Optimum processor under case II turbulence: target return perturbed; interference perturbed. $\mathbf{v}_s$ is known.

perturbed. The modified expression for the SINR in Case II is

$$\text{SINR}''_{JDO} = \frac{\sigma^2\xi_t \mathbf{w}'^H(\mathbf{v}_t\mathbf{v}_t^H \odot E[\boldsymbol{\phi}_{st}\boldsymbol{\phi}_{st}^H])\mathbf{w}'}{\mathbf{w}'^H\mathbf{R}_u\mathbf{w}'}. \tag{3.42}$$

Calling on Eqn. (3.41) and substituting $\hat{\mathbf{R}}_u'^{-1}\mathbf{v}_t$ for $\mathbf{w}'$ in the expression for the SINR gives

$$\text{SINR}''_{JDO} = \frac{\sigma^2\xi_t \mathbf{v}_t^H\hat{\mathbf{R}}_u'^{-1}(\mathbf{v}_t\mathbf{v}_t^H \odot E[\boldsymbol{\phi}_{st}\boldsymbol{\phi}_{st}^H])\hat{\mathbf{R}}_u'^{-1}\mathbf{v}_t}{\mathbf{v}_t^H\hat{\mathbf{R}}_u'^{-1}\mathbf{R}_u\hat{\mathbf{R}}_u'^{-1}\mathbf{v}_t} \tag{3.43}$$

$$= \frac{\sigma^2\xi_t \mathbf{v}_t^H\hat{\mathbf{R}}_u'^{-1}(\mathbf{v}_t\mathbf{v}_t^H \odot \mathbf{D}_{st})\hat{\mathbf{R}}_u'^{-1}\mathbf{v}_t}{\mathbf{v}_t^H\hat{\mathbf{R}}_u'^{-1}\mathbf{R}_u\hat{\mathbf{R}}_u'^{-1}\mathbf{v}_t}. \tag{3.44}$$

Clearly, the relation

$$\hat{\mathbf{R}}_u'^{-1}\mathbf{R}_u \neq \mathbf{I} \tag{3.45}$$

is an overriding factor preventing minimization in the denominator of $SINR''_{JDO}$. For heavier turbulence conditions, the interelement phase variance represented by $\mathbf{D}_{st}$ grows. This additional perturbation on $\hat{\mathbf{R}}_u'^{-1}$ further complicates minimization of the denominator of $SINR''_{JDO}$.

The performance of $SINR''_{JDO}$ is driven further from $SINR_{opt}$ by the expression in the numerator,

$$num(SINR''_{JDO}) = \sigma^2 \xi_t \mathbf{v}_t^H \hat{\mathbf{R}}_u'^{-1} (\mathbf{v}_t \mathbf{v}_t^H \odot \mathbf{D}_{st}) \hat{\mathbf{R}}_u'^{-1} \mathbf{v}_t. \tag{3.46}$$

Including the expression for $\hat{\mathbf{R}}_u'^{-1}$ transforms the expression for the numerator into

$$num(SINR''_{JDO}) = \sigma^2 \xi_t \mathbf{v}_t^H \{(\mathbf{R}_c \odot \mathbf{D}_{st}) + \mathbf{R}_n\}^{-1} (\mathbf{v}_t \mathbf{v}_t^H \odot \mathbf{D}_{st}) \{(\mathbf{R}_c \odot \mathbf{D}_{st}) + \mathbf{R}_n\}^{-1} \mathbf{v}_t. \tag{3.47}$$

With heavier turbulence, the effect of $\mathbf{D}_{st}$ grows, thereby degrading the STAP performance.

JDO performance degrades under Case II turbulence effects. Similarly, FTS performance also experiences similar performance losses. In fact, this is worth investigating because the performance losses introduced by turbulence effects in partially adaptive methods such as FTS may be more significant than in fully adaptive methods. The following development introduces the effect of Case II atmospheric turbulence perturbations on the FTS processing scheme.

3.3.5 Case II turbulence effects on Factored Time-Space (FTS). Section 3.3.2 describes the effects of Case II turbulence on the statistical representation of the interference environment. Section 2.3.5.4 introduces the details behind FTS processing. Analyzing the effects of Case II turbulence on FTS processing is more complicated than the analysis of Case I turbulence effects on FTS. This greater complexity comes about from turbulence effects on both the target return and on the estimate of $\mathbf{R}_u$. These turbulence perturbations on the estimate of $\mathbf{R}_u$ affect the formation of the FTS weight vectors. Figure 3.6 depicts the FTS processor in the presence of Case II turbulence. As the diagram illustrates, the measure of the interference as well as the target return are perturbed by the turbulence

effects. These effects influence the system beamformer and are reflected in the Doppler bin outputs.

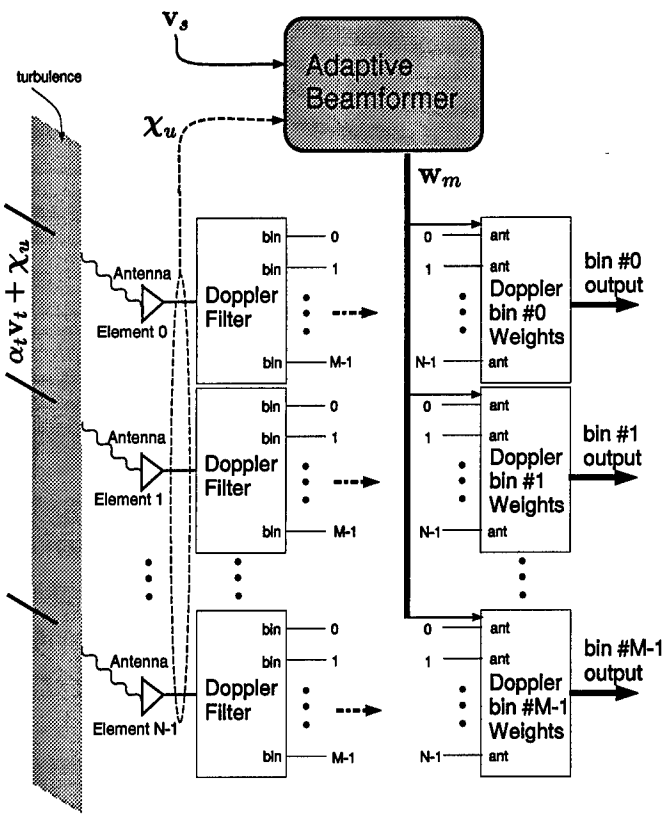

Figure 3.6 Factored Time-Space processor under case II turbulence: target return perturbed; interference perturbed. $\mathbf{v}_s$ is known.

The Case II turbulence effect is a specific concern in FTS processing because the weight vector, even under ideal conditions, is formed using the projection of $\mathbf{R}_u$ into a smaller signal space. Under Case II turbulence, the projection of $\hat{\mathbf{R}}'_u$ certainly leads to further performance losses. The following development examines the FTS algorithm with Case II turbulence effects added.

Equation (3.40) introduces the estimate of the undesired covariance matrix under case II turbulence as

$$\hat{\mathbf{R}}'_u = (\mathbf{R}_c \odot \mathbf{D}_{st}) + \mathbf{R}_n.$$

The expression for the FTS projection into the smaller dimension is given in Eqn. (2.88). The projection matrix for the m^{th} Doppler bin is given by $\mathbf{T}_m$. Applying this relation to $\hat{\mathbf{R}}'_u$ gives

$$\tilde{\hat{\mathbf{R}}}'_{um} = \mathbf{T}_m^H \hat{\mathbf{R}}'_u \mathbf{T}_m \tag{3.48}$$

$$= (\mathbf{f}_m \otimes \mathbf{I}_N)^H \hat{\mathbf{R}}'_u (\mathbf{f}_m \otimes \mathbf{I}_N) \tag{3.49}$$

$$= (\mathbf{f}_m \otimes \mathbf{I}_N)^H \{(\mathbf{R}_c \odot \mathbf{D}_{st}) + \mathbf{R}_n\} (\mathbf{f}_m \otimes \mathbf{I}_N). \tag{3.50}$$

From this expression, the adapted weight vector is formed as shown in Eqn. (2.89). The adapted weight vector is

$$\tilde{\mathbf{w}}'_m = \tilde{\hat{\mathbf{R}}}'^{-1}_{um} \tilde{\mathbf{g}}_t. \tag{3.51}$$

The SINR performance depends upon the composite weight vector. This is obtained by applying $\mathbf{T}_m$ to the adapted weight vector to project it back to the full dimension signal space. The composite weight vector under these conditions is

$$\mathbf{w}'_m = \mathbf{T}_m \tilde{\mathbf{w}}'_m. \tag{3.52}$$

$$= \mathbf{T}_m \tilde{\hat{\mathbf{R}}}'^{-1}_{um} \tilde{\mathbf{g}}_t. \tag{3.53}$$

Finally, inserting $\mathbf{w}'_m$ into the expression for the SINR gives a measure of performance. The SINR for FTS under Case II turbulence effects is

$$\text{SINR}''_{FTS} = \left[\frac{\sigma^2 \xi_t \mathbf{w}'^H_m E[(\mathbf{v}_t \mathbf{v}_t^H \odot \phi_{st} \phi_{st}^H)] \mathbf{w}'_m}{\mathbf{w}'^H_m \mathbf{R}_u \mathbf{w}'_m} \right]_{\text{max value of } m = 0, 1, \ldots, M-1} \tag{3.54}$$

$$= \left[\frac{\sigma^2 \xi_t \mathbf{w}'^H_m (\mathbf{v}_t \mathbf{v}_t^H \odot \mathbf{D}_{st}) \mathbf{w}'_m}{\mathbf{w}'^H_m \mathbf{R}_u \mathbf{w}'_m} \right]_{\text{max value of } m = 0, 1, \ldots, M-1}. \tag{3.55}$$

Once again, as in the JDO algorithm under Case II turbulence, the target return perturbation combined with the misformed weight vector affects performance. Combined with the implicit performance loss introduced by FTS processing, Case II turbulence produces the greatest performance degradation in FTS systems.

3.4 Summary

In this chapter, the effects of atmospheric turbulence are described analytically in terms of the SINR. The effects of two different situations involving atmospheric turbulence are examined. Case I turbulence involves an accurate statistic for the interference environment but a target return perturbed by turbulence effects. Case II turbulence involves a STAP processor faced with both a perturbed target return and a lower quality estimate of the interference environment due to turbulence induced perturbations. Both situations for the turbulence effect are examined under Joint Domain Optimum and Factored Time-Space processing. The analysis revealed performance degradations under both STAP methods for either Case I or Case II turbulence. The analysis also revealed that the heaviest performance loss is probably in a situation involving Case II turbulence induced perturbations on Factored Time-Space processing.

IV. Method

The goal of this study is to develop an understanding of the effects of atmospheric turbulence on Space-Time Adaptive Processing (STAP). This chapter describes the method used in simulation to focus on atmospheric effects on STAP.

To obtain statistically significant results, the effects of atmospheric turbulence are best studied in simulation. Following the developments presented in Chapter III, STAP processing may be simulated in the presence of turbulence effects. The simulations provide quantitative measurements of the effect which turbulence has on the statistics of the radar environment and on STAP performance. As Chapter III points out, some useful measures of STAP performance are the SINR and L_{SINR}. The SINR is the signal-to-interference-plus-noise ratio. The L_{SINR} is the SINR normalized by the optimum signal-to-noise ratio. In addition, the effect which turbulence perturbations have on measurements of the interference environment may be quantified by analyzing the interference covariance matrices. The perturbed interference covariance matrices are formed by sampling the interference signal in the presence of turbulence. The most telling statistic of the effect of turbulence on interference estimation is the eigenvalue distribution of the interference covariance matrix. The simulations outlined in this chapter are all geared to provide measurements of the SINR, L_{SINR}, and, where it is appropriate, the eigenvalue distribution under various turbulence conditions.

To meet the goals presented in Chapter I, STAP processing is simulated for different length arrays in varying turbulent environments. The simulations involve the following procedure:

- simulate Joint Domain Optimum (JDO) processing without turbulence effects to obtain baseline results
- simulate Factored Time-Space (FTS) processing without turbulence effects to obtain baseline results
- simulate JDO processing subject to uncorrelated, Gaussian distributed phase perturbations to obtain results under critical turbulence

- create phase structure function as a statistical representation of turbulence strength with respect to absolute distance. A phase structure function is created for each operating frequency f_0 and index of refraction structure constant C_n^2 value of interest.
- using realizations of turbulence-induced phase perturbations formed from the statistics of the phase structure function, simulate the JDO processing algorithm
  - Case I turbulence (target signal perturbed, interference covariance known)
  - Case II turbulence (target signal perturbed, interference covariance estimated through turbulence)
- using realizations of turbulence-induced phase perturbations formed from the statistics of the phase structure function, simulate the FTS processing algorithm
  - Case I turbulence
  - Case II turbulence

The simulations described above are performed for various array sizes, frequencies, and values of C_n^2. Table 4.1 provides details on the STAP geometries of the simulations as well as characteristics of the radar and of the atmospheric turbulence. This variety in simulation parameters ensures that turbulence effects are examined under many different conditions.

This chapter first presents details about the simulation tools used. Subsequent sections provide details on the parameters used in the experiment, methods for simulating the turbulent environment, and any unusual procedures or considerations which resulted.

4.1 Simulation tools

All simulations are run on a Sun workstation using MATLAB v5.0 by the MathWorks Co.

4.2 Simulation parameters

Examining the results of simulations conducted under various conditions, helps us to develop a description of the turbulence effects on STAP. Table 4.1 lists the varied parameters in this experiment and the values used in the simulations.

Table 4.1 Primary parameters for studying atmospheric turbulence effects on STAP processing. The STAP geometries, defined by the number of elements N and pulses M, simulate the dimensions of actual ground-based arrays. The operating frequencies also approximate radar frequencies of interest.

Category	Description	
STAP methods	Joint Domain Optimum (JDO)	Factored Time-Space (FTS)
Turbulence situations	**case I** Target return perturbed. Interference covariance known	**case II** Target return perturbed. Interference covariance estimated

Parameter	Values		
STAP Degs. of Freedom ($N \times M$)	200×3	64×5	32×10

Parameter	Values		
frequency (GHz)	3	10	30

Parameter	Values				
$\mathbf{C_n^2}$ ($\mathrm{m}^{-2/3}$)	5×10^{-14}	5×10^{-13}	5×10^{-12}	5×10^{-11}	5×10^{-10}

The antenna parameters: number of elements N, number of pulses M, and operating frequency f_o, closely approximate realistic ground-based radar systems. The C_n^2 values represent a wide range of turbulent conditions ranging from slight turbulence (5×10^{-14} $\mathrm{m}^{-2/3}$) to unrealistically heavy turbulence (5×10^{-10} $\mathrm{m}^{-2/3}$).

4.3 Phase structure function generation

The phase structure function is formed from phase screens created using a method developed by Welsh [14]. In this method, a Fourier Series based technique is used to produce screens of the size of the array. These screens incorporate the statistical properties of the turbulence to produce the phase structure function. The phase structure function $D_S(\rho)$ describes the variance of the turbulence induced phase difference as a function of the absolute distance between points along the array ρ.

The theoretical phase structure function is given by

$$D_{theo}(\boldsymbol{\rho}) = 3.089(2\pi)^{-5/3}\frac{6}{5}\left(\frac{L_0}{D_p}\right)^{5/3}\left(\frac{D_p}{r_0}\right)^{5/3} \times\left\{1-\frac{\Gamma[1/6]}{\pi^{1/6}}\left(\frac{|\boldsymbol{\rho}|}{D_p}\right)^{5/6}\left(\frac{L_0}{D_p}\right)^{-5/6}K_{5/6}\left[2\pi\frac{|\boldsymbol{\rho}|}{D_p}\frac{D_p}{L_0}\right]\right\}, \quad (4.1)$$

where L_0 is the outer scale of the turbulence, D_p is the periodic distance over which the Fourier Series represents the phase perturbation, $\Gamma[\cdot]$ is the Gamma-factorial function, $K_{5/6}[\cdot]$ is the 5/6 order Bessel function of the second kind, and r_0 represents the Fried parameter.

The statistical basis of the turbulence-induced index of refraction changes come from the index of refraction structure constant C_n^2 and the Fried parameter. With these quantities, the phase screens are formed. By specifying C_n^2, the propagation distance L, and the spatial wavenumber k, the Fried parameter is calculated. Assuming C_n^2 may be approximated by a constant, the Fried parameter is given by

$$\begin{aligned} r_0 &= 0.185\left[\frac{4\pi^2}{k^2\int C_n^2(z)dz}\right]^{3/5}, \\ &\approx 0.185\left[\frac{4\pi^2}{k^2LC_n^2}\right]^{3/5}. \end{aligned} \quad (4.2)$$

The shape of the phase structure function is dependent on the frequency f_0 and the value of C_n^2. Figure 4.1 shows a typical example of the phase structure function $D_S(\boldsymbol{\rho})$ and its theoretical value $D_{theo}(\boldsymbol{\rho})$. The phase structure function is formed by taking the expected value of the phase difference over many iterations of the Monte Carlo simulation. Reference Welsh's paper [14] for details.

The measured data presented by Hill *et al.* [11],[12] serves as a good reference for determining the accuracy of the phase screen generation algorithm. Under turbulent conditions of $C_n^2 = 5 \times 10^{-12}$ they measured the received phase difference of 173 GHz EM waves for antennas spaced 10 m apart. The resulting phase difference variance was 0.703 rad^2. Figure 4.2 depicts the phase structure function created by the phase screen

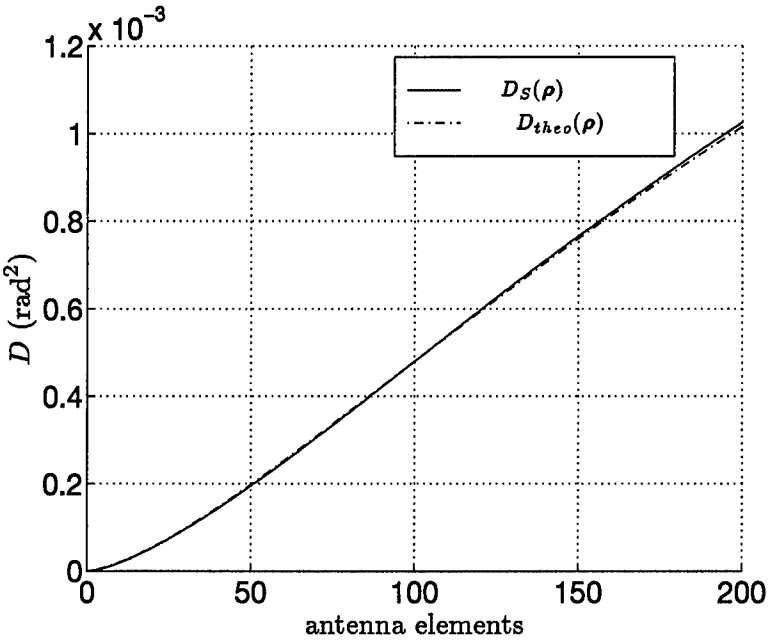

Figure 4.1 Examples of the simulated phase structure function $D_S(\rho)$ and the theoretical phase structure function $D_{theo}(\rho)$ are shown for $f_0 = 10$ GHz and $C_n^2 = 5 \times 10^{-13}$ m$^{-2/3}$. The functions are plotted against the absolute distance expressed in terms of the half-wavelength element spacing.

generation routine run with similar parameters. It is obvious that the 10 m phase difference variance depicted in the plot is very close to that measured by Hill.

Figures 4.3 through 4.7 show $D_S(\rho)$ and $D_{theo}(\rho)$ for the C_n^2 and f_0 parameters of interest in this study.

After forming $D_S(\rho)$, vectors of perturbed phase realizations corresponding to the statistics in $D_S(\rho)$ are created. The following section describes the procedure to create these realizations of the perturbed phases.

4.4 Spatial phase perturbation realizations

Once $D_S(\rho)$ is calculated for a certain frequency and C_n^2 value, realizations of the phase perturbation over the N antenna elements may be created. These realizations are created based upon the statistics of the phase perturbations described by $D_S(\rho)$ so they realistically model the effect of turbulence on the EM wave propagating near to the array.

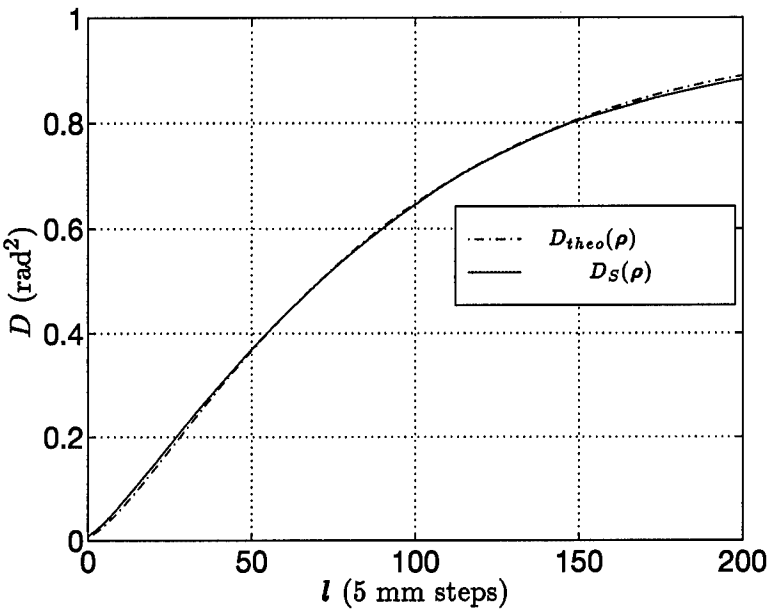

Figure 4.2 Simulated phase structure function $D_S(\rho)$ and the theoretical phase structure function $D_{theo}(\rho)$ are shown for $f_0 = 173$ GHz and $C_n^2 = 5 \times 10^{-12}$ m$^{-2/3}$. The functions are plotted against the absolute distance l, represented in steps of 5 mm. These statistics are in good agreement with measured values reported by Hill [11],[12].

If the variance of the element-to-element phase difference is known, then a realization of the phase perturbation may be created. Equation (2.11) draws a relationship between the phase structure function and the element-to-element phase perturbation covariance. This zero-mean relationship may be expressed as

$$\begin{aligned} D_S(\rho) &= E[(S(\vec{r}) - S(\vec{r} - \vec{r}'))^2] \\ &= 2E[S^2(0)] - 2E[S(\vec{r})S(\vec{r} - \vec{r}')], \end{aligned} \tag{4.3}$$

where $S(\vec{r})$ represents the phase at location $\vec{r}$ and $\rho = \vec{r} - \vec{r}'$. So the phase perturbation covariance is

$$E[S(\vec{r})S(\vec{r} - \vec{r}')] = E[S^2(0)] - \frac{1}{2}D_S(\rho). \tag{4.4}$$

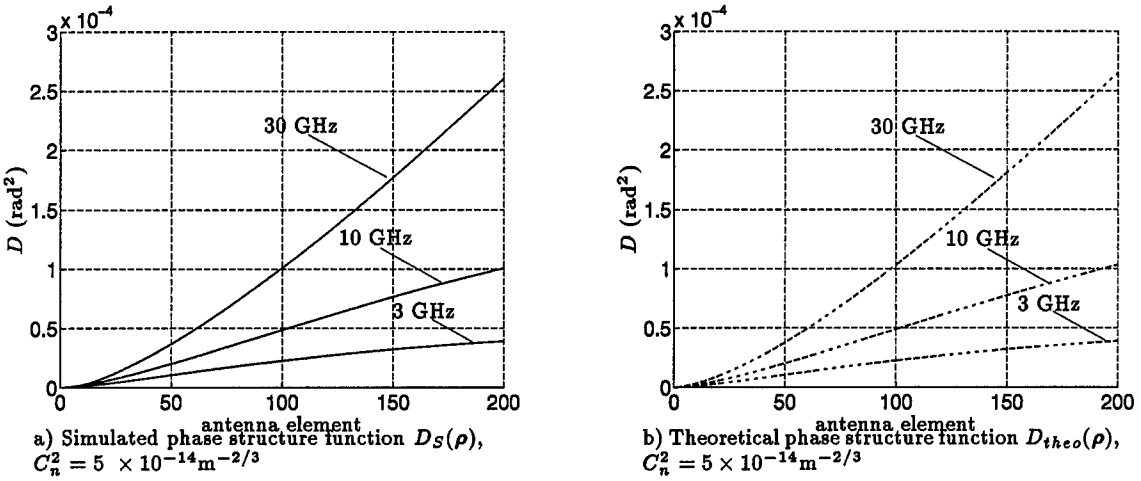

a) Simulated phase structure function $D_S(\rho)$, $C_n^2 = 5 \times 10^{-14}\mathrm{m}^{-2/3}$

b) Theoretical phase structure function $D_{theo}(\rho)$, $C_n^2 = 5 \times 10^{-14}\mathrm{m}^{-2/3}$

Figure 4.3 Plots of $D_S(\rho)$ and $D_{theo}(\rho)$ used in this atmospheric turbulence study. These plots depict the phase structure function over $N = 200$ antenna elements. The element spacing is half-wavelength. Therefore, the actual distance along the x-axis in the plots varies depending on the frequency of the EM wave described by the corresponding plot. Parameters used to generate these functions are listed in Table 4.2. These plots are for C_n^2 values of $5 \times 10^{-14}\mathrm{m}^{-2/3}$.

The phase perturbation covariance may also be written in the form of a covariance matrix

$$\mathbf{R}_{\psi_s} = \begin{bmatrix} 1 & \dots & 1 \\ \vdots & \ddots & \\ 1 & & 1 \end{bmatrix}_{N \times N} \times \left(MSV_{\psi_s} - \frac{1}{2}\mathrm{Toep}[\mathbf{d}_S] \right), \tag{4.5}$$

where the mean squared value of the phase is expressed as the constant $MSV_{\psi_s} = E[S^2(0)] = 0$ and the values of $D_S(\rho)$ over N antenna elements are held in the vector $\mathbf{d}_S$. The operation Toep[$\cdot$] creates a Toeplitz matrix from a vector. The Toeplitz matrix in Eqn. (4.5) has zero values along the diagonal with values increasing towards the edges of the matrix. The computations described by Equation (3.39) to calculate the perturbed clutter covariance matrix through statistical means may be performed by using the relation

$$\mathbf{D}_{st} = \exp\left(\mathbf{R}_{\psi_t} \otimes \mathbf{R}_{\psi_s}\right), \tag{4.6}$$

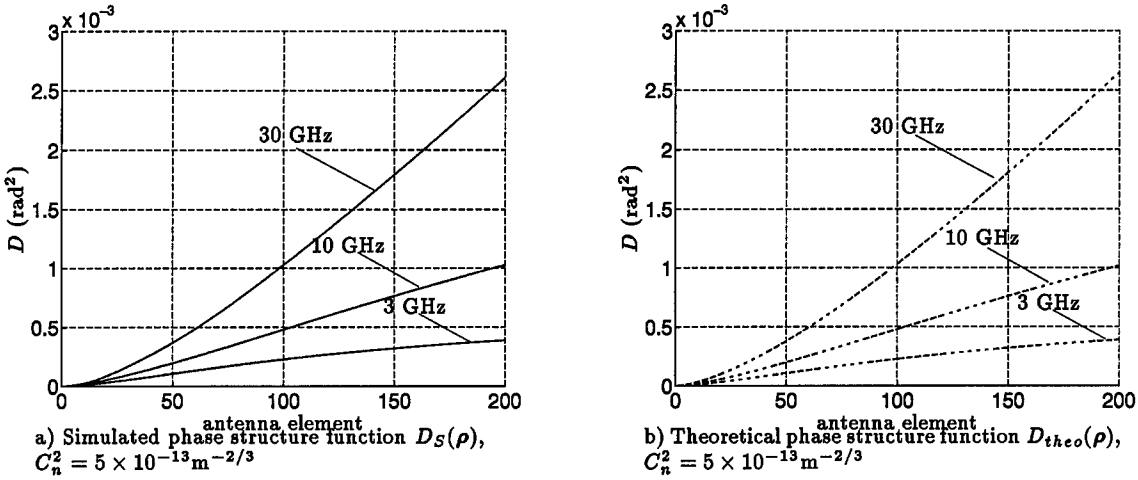

a) Simulated phase structure function $D_S(\rho)$, $C_n^2 = 5 \times 10^{-13}\mathrm{m}^{-2/3}$

b) Theoretical phase structure function $D_{theo}(\rho)$, $C_n^2 = 5 \times 10^{-13}\mathrm{m}^{-2/3}$

Figure 4.4 Plots of $D_S(\rho)$ and $D_{theo}(\rho)$ used in this atmospheric turbulence study. These plots depict the phase structure function over $N = 200$ antenna elements. The element spacing is half-wavelength. Therefore, the actual distance along the x-axis in the plots varies depending on the frequency of the EM wave described by the corresponding plot. Parameters used to generate these functions are listed in Table 4.2. These plots are for C_n^2 values of $5 \times 10^{-13}\mathrm{m}^{-2/3}$.

where

$$\mathbf{R}_{\psi_t} = \begin{bmatrix} 1 & \dots & 1 \\ \vdots & \ddots & \\ 1 & & 1 \end{bmatrix}_{M \times M}$$

provides for the zero temporal phase perturbation.

To create the perturbed covariance via the Monte Carlo simulation method presented in Sec. 3.3.1 and to compute the SINR under target return perturbation, individual realizations of the phase perturbations must be computed. These realizations may be computed by coloring the vector of uncorrelated, zero-mean, Gaussian distributed values $\mathbf{w} \sim \mathcal{N}(0,1)$. This coloring process is given by

$$\boldsymbol{\phi}_s = \exp(j\mathbf{C}_{\psi_s}^H \mathbf{w}), \tag{4.7}$$

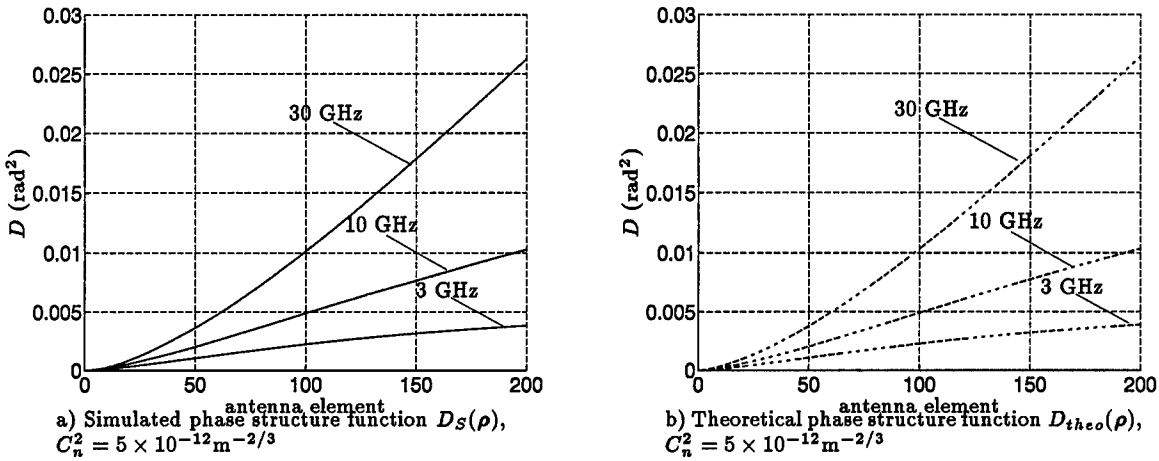

a) Simulated phase structure function $D_S(\rho)$, $C_n^2 = 5 \times 10^{-12}\text{m}^{-2/3}$

b) Theoretical phase structure function $D_{theo}(\rho)$, $C_n^2 = 5 \times 10^{-12}\text{m}^{-2/3}$

Figure 4.5 Plots of $D_S(\rho)$ and $D_{theo}(\rho)$ used in this atmospheric turbulence study. These plots depict the phase structure function over $N = 200$ antenna elements. The element spacing is half-wavelength. Therefore, the actual distance along the x-axis in the plots varies depending on the frequency of the EM wave described by the corresponding plot. Parameters used to generate these functions are listed in Table 4.2. These plots are for C_n^2 values of $5 \times 10^{-12}\text{m}^{-2/3}$.

where

$$\mathbf{C}_{\psi_s} = \text{Cholesky}[\mathbf{R}_{\psi_s}]. \tag{4.8}$$

The vector of complex values due to the phase perturbations is represented by $\boldsymbol{\phi_s}$. The Cholesky factorization operation on $\mathbf{R}_{\psi_s}$ gives $\mathbf{C}_{\psi_s}$ such that $\mathbf{R}_{\psi_s} = \mathbf{C}_{\psi_s}^H \mathbf{C}_{\psi_s}$ holds true. Figure 4.8 shows a set of individual realizations of the phase perturbation for the $\mathbf{D}_S(\boldsymbol{\rho})$ shown in Fig. 4.1. Once again, the space-time vector of complex values due to the perturbed phases is

$$\boldsymbol{\phi}_{st} = \boldsymbol{\phi}_t \otimes \boldsymbol{\phi}_s,$$

and in this study, the temporal vector of values due to the perturbed phases is

$$\boldsymbol{\phi}_t = \mathbf{1}_M, \tag{4.9}$$

a vector of M ones since turbulence effects on temporal phase variations are considered negligible.

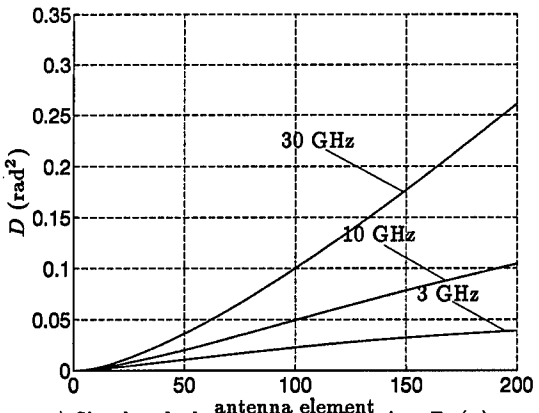

a) Simulated phase structure function $D_S(\rho)$, $C_n^2 = 5 \times 10^{-11}$ $mboxm^{-2/3}$

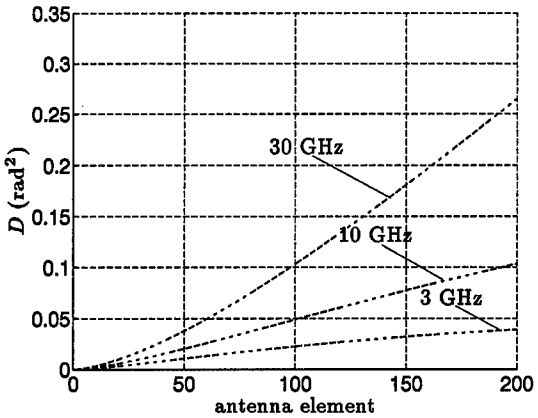

b) Theoretical phase structure function $D_{theo}(\rho)$, $C_n^2 = 5 \times 10^{-11}\mathrm{m}^{-2/3}$

Figure 4.6 Plots of $D_S(\boldsymbol{\rho})$ and $D_{theo}(\boldsymbol{\rho})$ used in this atmospheric turbulence study. These plots depict the phase structure function over $N = 200$ antenna elements. The element spacing is half-wavelength. Therefore, the actual distance along the x-axis in the plots varies depending on the frequency of the EM wave described by the corresponding plot. Parameters used to generate these functions are listed in Table 4.2. These plots are for C_n^2 values of $5 \times 10^{-11}\mathrm{m}^{-2/3}$.

4.4.1 Practical considerations. While performing the simulations described in this chapter, a few practical considerations present themselves. Many of the relationships presented in this thesis appear sound when written symbolically. However, when the mathematics in these equations are carried out on a computer, small deviations from theory are introduced by the limits of floating point computations.

A theoretically valid operation on a specific value or set of values may not be valid when calculated on a microprocessor. A good example of this is the practical differences between Equations (2.59) and (2.62). The two forms of the clutter covariance calculation given in these equations are

$$\begin{aligned} \mathbf{R}_c &= \sigma^2 \sum_{cp=1}^{N_c} \xi_{cp} (\mathbf{b}_{cp}\mathbf{b}_{cp}^H) \otimes (\mathbf{a}_{cp}\mathbf{a}_{cp}^H) \\ &= \mathbf{V}_c \boldsymbol{\Xi}_c \mathbf{V}_c^H. \end{aligned}$$

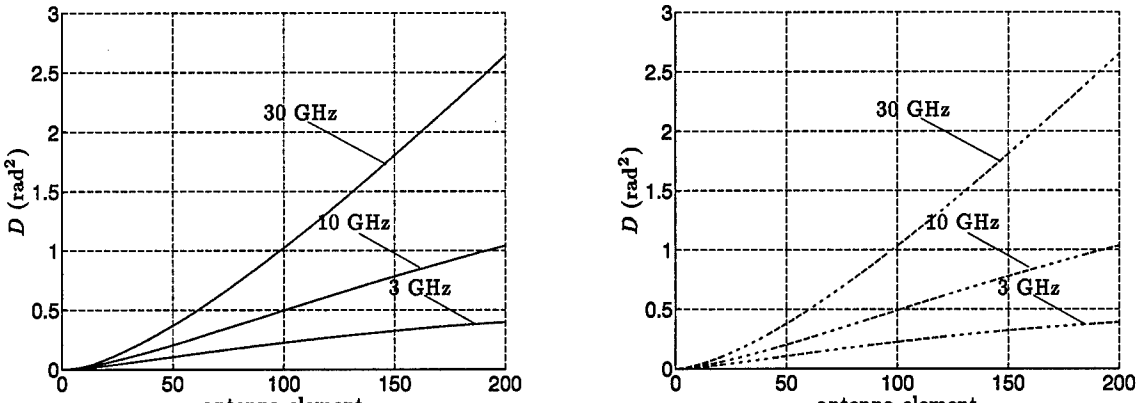

a) Simulated phase structure function $D_S(\rho)$, $C_n^2 = 5 \times 10^{-10}\text{m}^{-2/3}$

b) Theoretical phase structure function $D_{theo}(\rho)$, $C_n^2 = 5 \times 10^{-10}\text{m}^{-2/3}$

Figure 4.7 Plots of $D_S(\rho)$ and $D_{theo}(\rho)$ used in this atmospheric turbulence study. These plots depict the phase structure function over $N = 200$ antenna elements. The element spacing is half-wavelength. Therefore, the actual distance along the x-axis in the plots varies depending on the frequency of the EM wave described by the corresponding plot. Parameters used to generate these functions are listed in Table 4.2. These plots are for C_n^2 values of $5 \times 10^{-10}\text{m}^{-2/3}$.

One criteria which must be met by $\mathbf{R}_c$ is that this matrix must have Hermitian symmetry described by

$$\mathbf{R}_c = \mathbf{R}_c^H. \tag{4.10}$$

When Eqn. (2.62) is implemented on a computer, the output does not always meet the Hermetian symmetry criterion. Therefore, when using this form of covariance formation, Hermetian symmetry must be forced by creating a new covariance matrix. The new covariance matrix is guaranteed to be Hermetian if it is formed by

$$\mathbf{R}_{c_{new}} = \frac{1}{2}(\mathbf{R}_c + \mathbf{R}_c^H). \tag{4.11}$$

Under this method, $\mathbf{R}_{c_{new}}$ lacks the small numeric inconsistencies between its upper and lower triangle which prevent it from being perfectly Hermetian.

Another consideration involving calculated covariance matrices appears in performing the Cholesky factorization of the interference-plus-noise covariance matrix $\mathbf{R}_u$. In order to perform Cholesky on a matrix, the matrix must be positive definite. Being positive

Table 4.2 List of parameters used to create $D(\rho)$.

C_n^2 ($m^{-2/3}$)	5×10^{-14}			5×10^{-13}		
f (GHz)	3	10	30	3	10	30
L_0 (m)	35	20		35	20	
L (km)	10	10		10	10	
r_0 (m)	4.444×10^3	1.048×10^3	280.4	1.116×10^3	263.29	70.44

C_n^2 ($m^{-2/3}$)	5×10^{-12}			5×10^{-11}			5×10^{-10}		
f (GHz)	3	10	30	3	10	30	3	10	30
L_0 (m)	35	20		35	20		35	20	
L (km)	10	10		10	10		10	10	
r_0 (m)	280.4	66.14	17.69	70.44	16.61	4.444	17.69	4.173	1.116

definite means that for any vector $\mathbf{x}$, its inner product with a positive definite matrix $\mathbf{Y}$ follows is

$$\mathbf{x}^H \mathbf{Y} \mathbf{x} > 0. \tag{4.12}$$

Another criterion which a matrix must meet to be classified positive definite states that a positive definite matrix has only positive eigenvalues. However, in forming certain covariance matrices, a few small eigenvalues may have negative values.

A correction may be applied to a covariance matrix to assure positive definiteness. This correction is given by

$$\mathbf{R}_{u_{new}} = \mathbf{R}_u + \lambda_{small}\mathbf{I}, \tag{4.13}$$

where λ_{small} is one of the smallest of the negative eigenvalues. Appendix A contains a mathematical proof describing why Eqn. (4.13) can transform a covariance matrix into a positive definite covariance matrix.

4.5 White Gaussian phase perturbations

In order to gauge the varying effects of various scales of atmospheric turbulence, some well understood form of phase perturbation must be applied as a test case. The measure of the resulting performance degradation may be used to compare with the performance

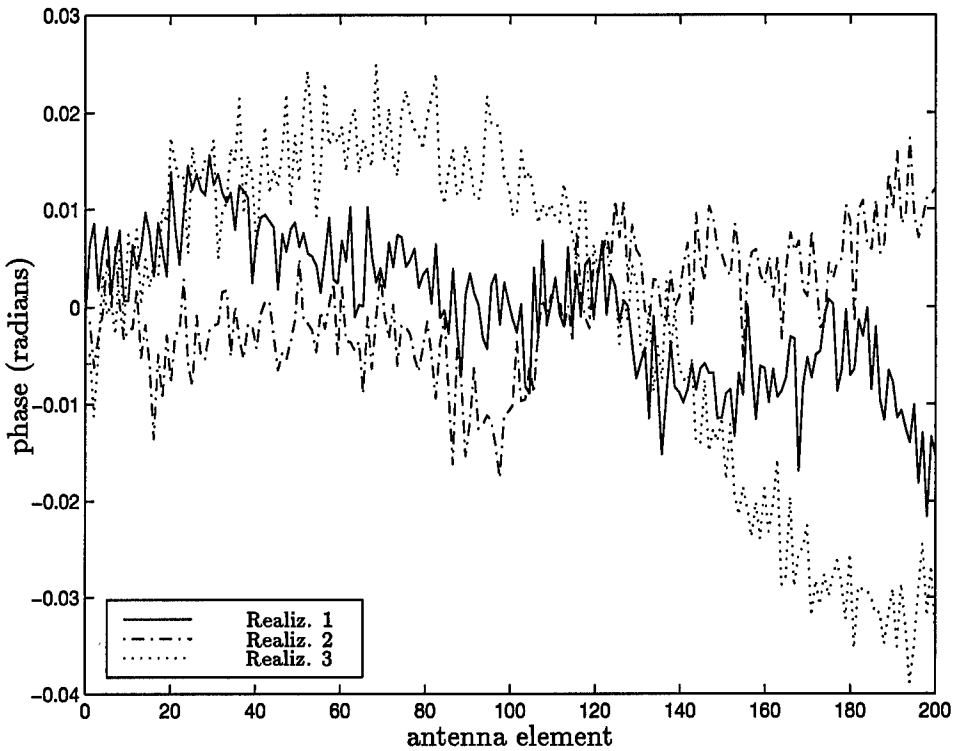

Figure 4.8 Three realizations of the phase perturbations over 200 antenna elements. The realizations are created using $D(\rho)$ calculated for $f_0 = 10$ GHz and $C_n^2 = 5 \times 10^{-13}$ m$^{-2/3}$. Each of the three realizations is shifted to zero-mean for display purposes.

degradation realized by applying simulated phase perturbations due to atmospheric turbulence.

Hill *et al.* [11] state that the phase perturbations caused by atmospheric turbulence effects follow a Gaussian distribution. The Gaussian distribution is therefore the best model for creating a test case. Using uncorrelated Gaussian random variables for the phase perturbations creates a type of critical scenario for STAP. The phase perturbations for the test cases were created using a zero-mean Gaussian random number generator. The

N element spatial phase perturbation vector for these test cases is

$$\phi_s \sim \exp\left(j\begin{bmatrix}\mathcal{N}(0,\sigma^2_{test})\\ \mathcal{N}(0,\sigma^2_{test})\\ \vdots \\ \mathcal{N}(0,\sigma^2_{test})\end{bmatrix}_N\right), \tag{4.14}$$

where σ^2_{test} is the element-to-element variance of the phase perturbations. The statistics of the white Gaussian phase perturbation are reflected in

$$\mathbf{D}_s = \begin{bmatrix} 1 & & & \\ & \ddots & e^{-\sigma^2_{test}} & \\ & 1 & & \\ e^{-\sigma^2_{test}} & & \ddots & \\ & & & 1 \end{bmatrix}. \tag{4.15}$$

In this thesis, the different values of σ^2_{test} used are (0.01, 0.03, 0.05, 0.07, 0.10, 0.13, and 0.16 rad^2). These values are used because the variance of the phase perturbations generated from the phase structure function range from 1×10^{-6} to 0.06 rad^2.

4.6 Environment parameters

The environment described in Ward's report [17] is recreated for this study. Table 4.3 displays the settings of the most important parameters for the target and interference in the simulations. Any other settings follow the environment depicted in Ward's report. Jammers are excluded in this study so a basic analysis of turbulence effects on STAP may be carried out with only clutter interferers.

4.7 Implementing the Joint Domain Optimum (JDO) algorithm

The JDO algorithm is implemented just as it is described in Chapter II. No taper is added to the desired space-time steering vector. The SINR is calculated by forming a new weight vector to match a target return for each frequency bin of the Doppler space.

Table 4.3 The basic environment used for the simulations in this study.

Object	Parameter	Setting
Target	Location (Az)	0°
	Elevation (Az)	5°
	Doppler freq (Hz)	50
	Range (km)	20
Clutter	No. of patches	360
	Range (km)	10
	reflectivity (dB)	-3
Jammers	None	

4.8 Implementing the Factored Time-Space (FTS) algorithm

The FTS algorithm is also implemented just as it is described in Chapter II. The Doppler filters incorporate an 80 dB taper to ensure good FTS performance.

4.9 Summary

This chapter summarizes the procedures used to simulate the effects of atmospheric turbulence on STAP processing. In Sec. 4.2, the details on the general simulation parameters are presented. Section 4.3 describes the method used to calcuate a statistical representation of the various level phase screens. The statistical representation is known as the phase structure function. Section 4.4 reviews the methods used to create perturbed phase realizations as well as the methods to calculate, from the phase structure function, the statistical quantities describing the phase perturbations. The last three sections describe the environment under which the simulations are run and the parameters used in the JDO and FTS algorithms.

V. Results

This chapter presents the results of the simulations described in Chapter IV. The simulation results show the performance of the various STAP algorithms with varying geometries and turbulent environments. These results are shown referenced against the baseline performance, or the performance with no turbulence induced perturbations, for each configuration. The signal-to-interference-plus-noise ratio (SINR) loss, also known as the L_{SINR} is used as the primary measure of performance. Comparing the L_{SINR} resulting from each simulation to the L_{SINR} for the optimal case gives a quantitative measure of the STAP performance loss under the conditions simulated.

Both Case I turbulence and Case II turbulence simulation results are given in this chapter. Case I turbulence describes the situation in which the STAP system has a precise estimate of the interference covariance matrix but the target signal is perturbed by turbulence effects. Case II turbulence describes the situation in which both the covariance estimate and the target signal received by the STAP system are perturbed by turbulence. Differentiating the effects of turbulence between these cases allows us to recognize which effects degrades performance the most. For Case II turbulence, it is useful to examine changes in the eigenvalue distribution of the perturbed clutter covariance matrix estimates with different turbulence effects. The eigenvalue distribution of the perturbed clutter covariance matrix estimates are also compared to a baseline provided by the eigenvalue distribution of the unperturbed version of these matrices.

The results in this chapter are presented in the following order:

- baseline (unperturbed) Joint Domain Optimum (JDO) performance
  - baseline (unperturbed) L_{SINR}
  - baseline (unperturbed) eigenspectra for $\mathbf{R}_c$
- Case I turbulence effects on JDO performance
  - L_{SINR}
- Case II turbulence effects on JDO performance

  - eigenspectra for $\mathbf{R}_c'$
  - L_{SINR}
- white Gaussian distributed phase perturbations
  - JDO performance effects of Case I turbulence simulated by uncorrelated Gaussian distributed phase perturbations
    * L_{SINR}
- baseline (unperturbed) Factored Time-Space (FTS) performance (32 antenna elements $\times$ 10 pulses)
  - (unperturbed) L_{SINR}
- Case I turbulence effects on FTS performance (32 antenna elements $\times$ 10 pulses)
  - L_{SINR}
- Case II turbulence effects on FTS performance (32 antenna elements $\times$ 10 pulses)
  - L_{SINR}

The results in each of the sections of this chapter are presented as

- plots of the L_{SINR} across the Doppler space
- plots of the distribution of energy among the eigenvalues

FTS performance is presented for the 32 antenna element $\times$ 10 pulses configuration only because other configurations do not include enough pulses to ensure reliable FTS performance. White Gaussian distributed phase perturbation effects are not considered for Case II turbulence because this form of perturbation is highly similar to including additional receiver noise.

This chapter uses the metrics listed above to present simulation results which highlight turbulence effects on STAP.

5.1 *Joint Domain Optimum (JDO) Baseline Performance*

Analyzing the JDO algorithm performance under turbulent conditions requires a standard for comparison. The standard used for comparison in this study is the signal-to-interference-plus-noise ratio loss (L_{SINR}) without any turbulence effects. This metric is referred to as the algorithm's baseline performance. The L_{SINR} plots representing baseline performance are shown in Figs. 5.1 through 5.3. The ripples in the L_{SINR} across the

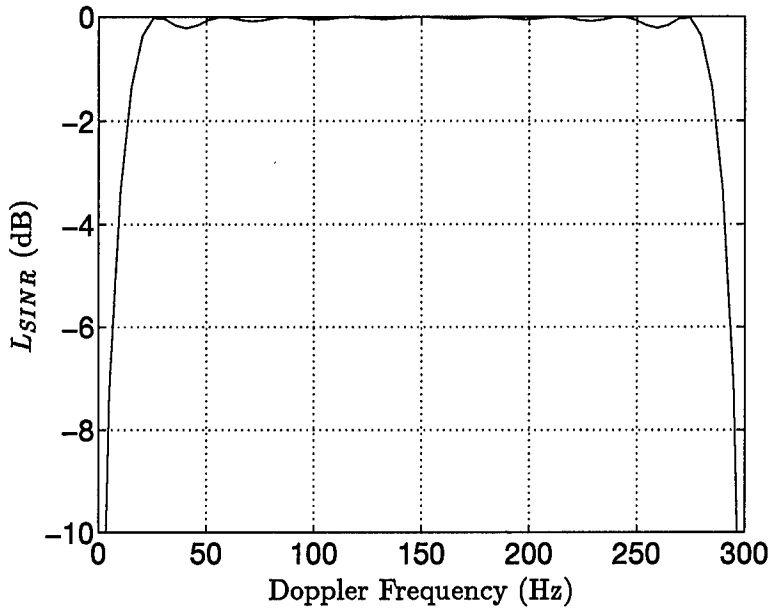

Figure 5.1 Baseline L_{SINR} for JDO. Processing performed on 32 antenna elements and 10 pulses.

doppler space are a result of the small number of pulses used in these simulations. The L_{SINR} is much smoother in Fig. 5.1 than in Fig. 5.2 and a similar relationship is true between Fig. 5.2 and Fig. 5.3. As the number of pulses falls from 10 to 5 to 3, the effect on the performance is evident as some shifting or rippling of the L_{SINR} across the Doppler space. This shifting effect is caused by the poor Doppler resolution available to the steering vector. The Doppler resolution is directly related to the number of elements in the temporal steering vector. With so few pulses defining the size of the temporal steering vector, the Doppler resolution suffers. Nonetheless, each of the optimal JDO plots achieve

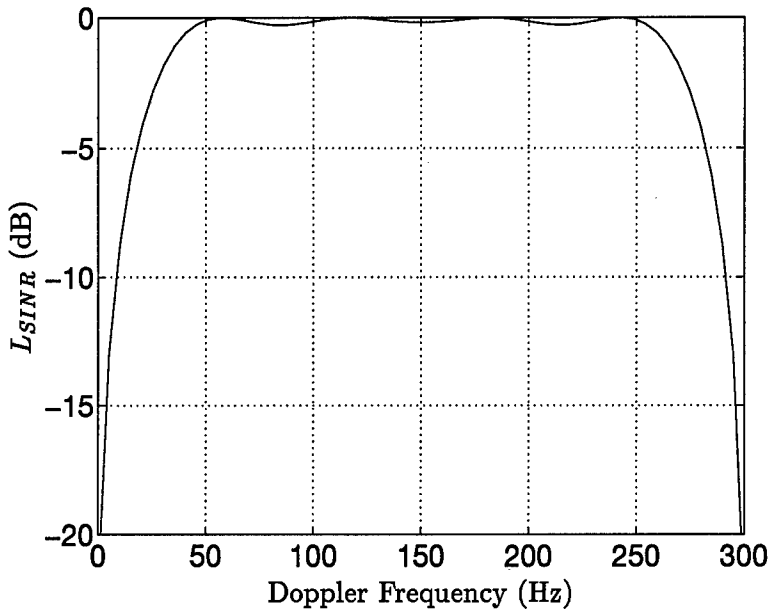

Figure 5.2 Baseline L_{SINR} for JDO. Processing performed on 64 antenna elements and 5 pulses.

0 dB performance within the Doppler space. These results are used as the baseline or the standard for comparison for the other simulations in this study.

Under Case II turbulence, the estimate of the interference is perturbed by turbulence. The eigenvalue spectrum of the interference covariance matrix ($\mathbf{R}_c'$) is a useful tool for analyzing the effects of turbulence on the estimation of these matrices. To use these tools, another baseline must be drawn. Figures 5.4 through 5.6 show the eigenspectra for the unperturbed clutter covariance $\mathbf{R}_c$.

Brennan's rule [17] states that the rank of the clutter covariance estimate is

$$r_c \sim \text{round}[N + (M-1)\beta]. \tag{5.1}$$

The operation of rounding a non-integer to an integer value is represented by the round[·] function. The velocity of the radar platform is represented by β. Since the radar platform is ground-based in this study, $\beta = 0$. So the rank is a function of the number of antenna elements N. Examining the eigenvalue number at which the eigenvalues drop significiantly, it is obvious that each of the baseline covariance matrix estimates follows Brennan's rule.

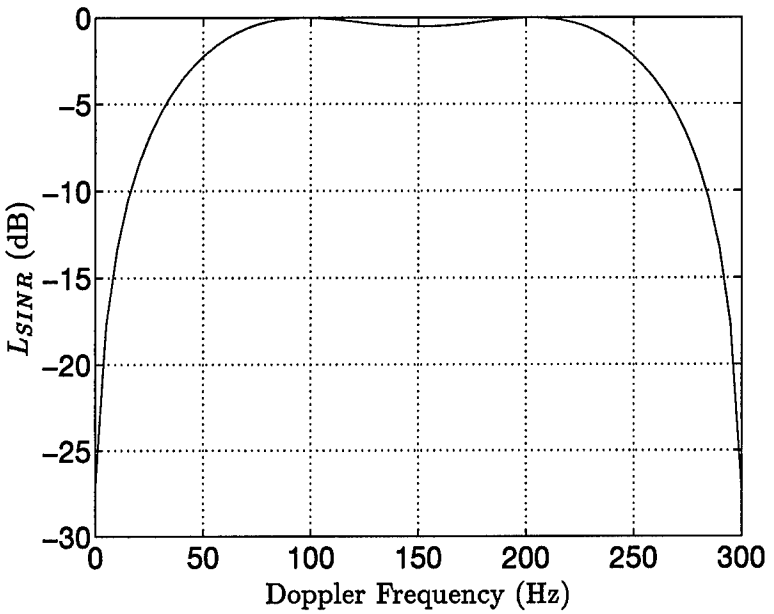

Figure 5.3 Baseline L_{SINR} for JDO. Processing performed on 200 antenna elements and 3 pulses.

The eigenvalue number at which this drop occurs is the rank of the matrix and the rank matches the number of antenna elements precisely.

The next two sections examine JDO performance under Case I and Case II turbulence conditions. Case I turbulence implies the system already has an accurate estimate of the interference covariance matrix but turbulence perturbs the reception of the target return. On the other hand, Case II turbulence implies that the system's interference covariance matrix estimate as well as the reception of the target return are perturbed by the turbulence effects.

5.2 JDO Performance with Case I Turbulence

The Case I turbulence effects are reached by using the same procedures used to produce the plots shown in Sec. 5.1 while adding the turbulence perturbations to the target return. These results reflect effects found in using the frequencies, element and pulse sizes, and index of refraction structure constant C_n^2 values listed in Table 4.1. The various C_n^2 values represent light to heavy turbulence. Combined with the trio of frequencies,

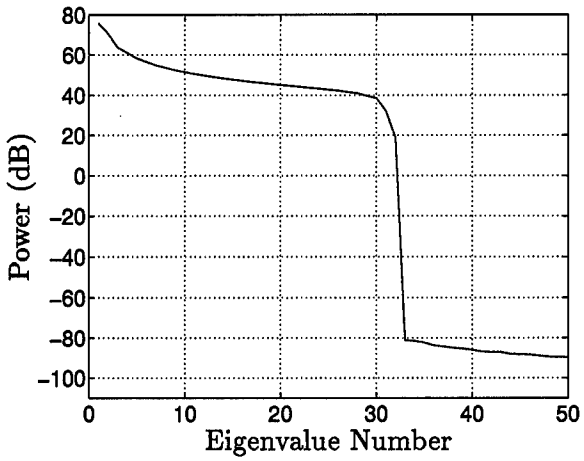

Figure 5.4 Eigenvalue distribution plots for $\mathbf{R}_c$ with no turbulence effects. Covariance matrices formed from signals on 32 antenna elements and 10 pulses.

turbulence effects which vary with turbulence strength and frequency may be examined. The following sections each examine the variety of turbulence effects for each element-pulse combination.

5.2.1 32 antenna elements, 10 pulses. The JDO performance is expressed as the L_{SINR} in Figs. 5.7a through 5.7c. Figure 5.7a shows the performance for an operating frequency f_0 of 3 GHz. Figure 5.7b represents the performance at 10 GHz and Fig. 5.7c represents the performance at 30 GHz. These plots focus on the L_{SINR} range between 0 dB and -10 dB. It is evident from these plots that there is little effect due to turbulence. The L_{SINR} plots for situations involving typical turbulence (C_n^2 of 5×10^{-13} to $5 \times 10^{-11} \mathrm{m}^{-2/3}$) are so close in performance to the optimal L_{SINR}, the broken line representing optimal performance is not even evident. The only plot showing significant performance loss is the $C_n^2 = 5 \times 10^{-10}$ $\mathrm{m}^{-2/3}$ case. Even under this extremely heavy turbulence case, the L_{SINR} falls by only 2 dB and 6 dB for 3 and 30 GHz respectively.

5.2.2 64 antenna elements, 5 pulses. Just as in the previous section, this section examines JDO performance effects for Case I turbulence in a 64 element $\times$ 5 pulse STAP system. Figures 5.8a through 5.8c also demonstrate a minimal effect due to Case I turbulence. However, the turbulence effects over 64 antenna elements appear to be greater

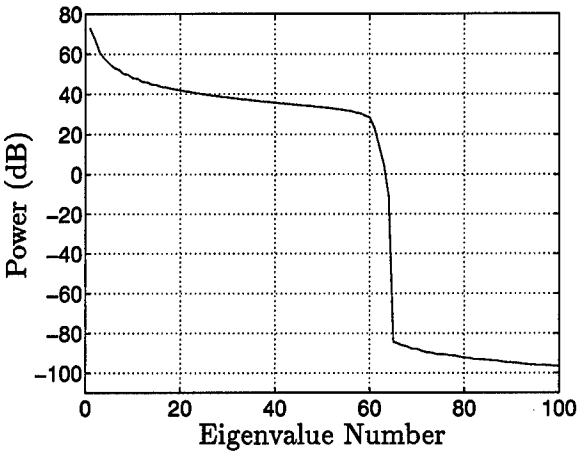

Figure 5.5 Eigenvalue distribution plots for $\mathbf{R}_c$ with no turbulence effects. Covariance matrices formed from signals on 64 antenna elements and 5 pulses.

than the effects seen over 32 antenna elements. In this case the L_{SINR} plots demonstrate evidence of a performance degradation for C_n^2 values of 5×10^{-10} and 5×10^{-11} $\mathrm{m}^{-2/3}$. These 64 element performance losses are greater than those seen in the 32 element case.

5.2.3 200 antenna elements, 3 pulses. Once again, the same JDO simulations are run under case I turbulence. In this set of simulations, the antenna parameters are 200 antenna elements and 3 pulses. Figures 5.9a through 5.9c show a greater performance loss than in either of the smaller antenna arrays. Figs. 5.9a through 5.9c also contain further evidence that turbulence effects are dependent on frequency. In the 200 element system, the performance loss at 30 GHz is noticably larger than that at 10 GHz and the loss at 10 GHz is more significant than at 3 GHz. It is also evident that the performance losses reach a threshold at -23 dB. The plot for $C_n^2 = 5 \times 10^{-10}\mathrm{m}^{-2/3}$ is at -23 dB for all frequencies while plots for other C_n^2 values fall towards that level with increasing frequency.

5.2.4 Explanation. The larger performance losses with increasing C_n^2, array size, and frequence correspond directly with the phase structure function plots in Figs. 4.3 through 4.7. As the element-to-element phase difference variance increases, the weight vector mismatch with the perturbed target steering vector also increases. This mismatch is caused by the turbulence-induced phase errors at each antenna element.

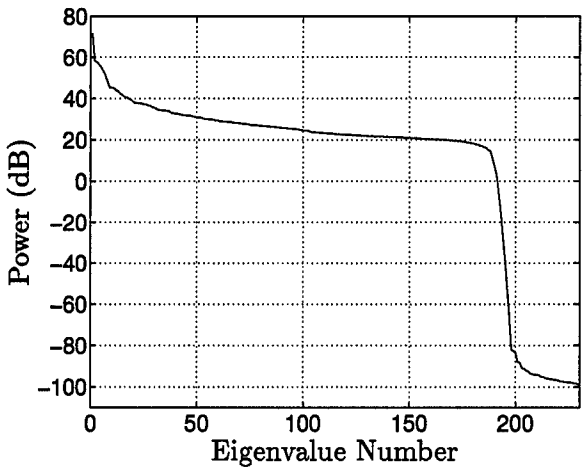

Figure 5.6 Eigenvalue distribution plots for $\mathbf{R}_c$ with no turbulence effects. Covariance matrices formed from signals on 200 antenna elements and 3 pulses.

The plots in this chapter are shown relative to JDO baseline performance. It is also useful to examine the data relative to data from some well-established perturbation method. The next section discusses simulation results for JDO performance losses where Case I turbulence phase perturbations are simulated with white Gaussian noise.

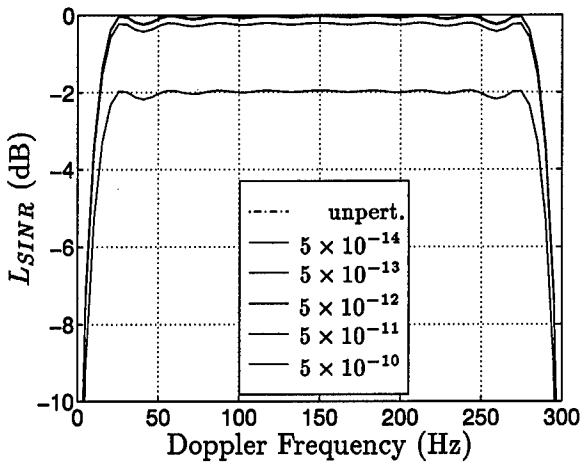

a) $f_0 = 3$ GHz

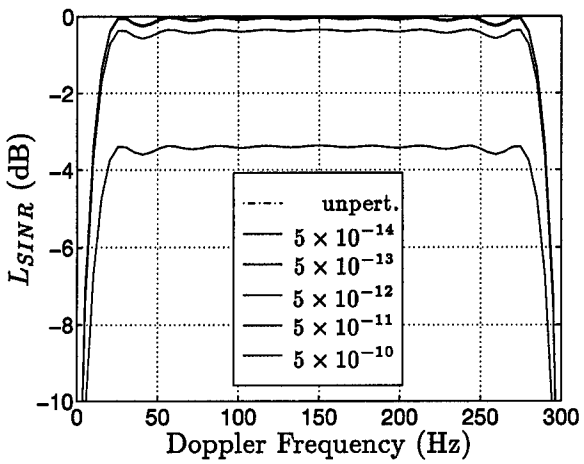

b) $f_0 = 10$ GHz

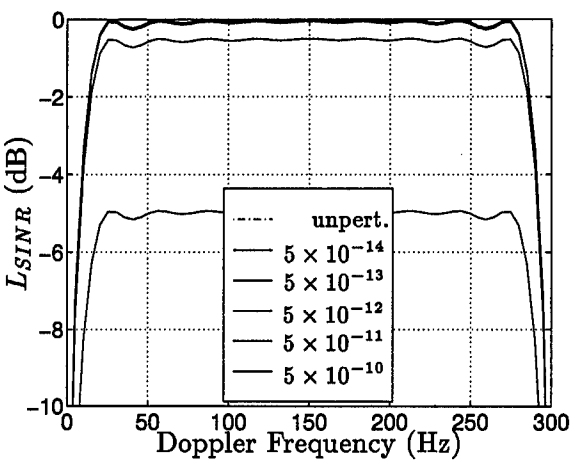

c) $f_0 = 30$ GHz

Figure 5.7 L_{SINR} plots for JDO under Case I turbulence. Processing performed on 32 antenna elements and 10 pulses.

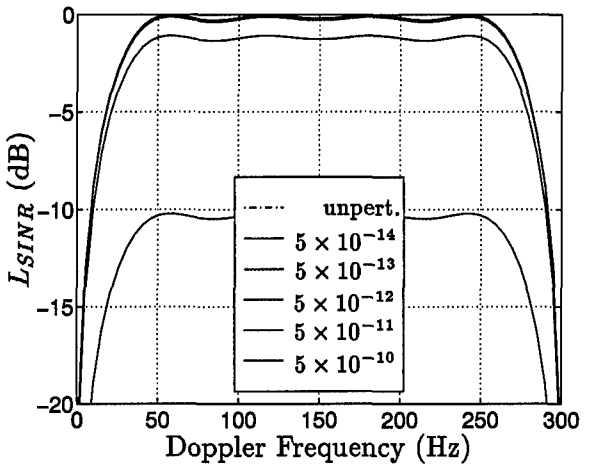

a) $f_0 = 3$ GHz

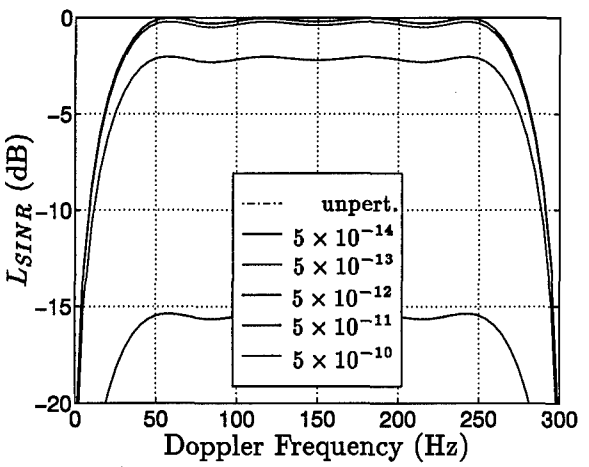

b) $f_0 = 10$ GHz

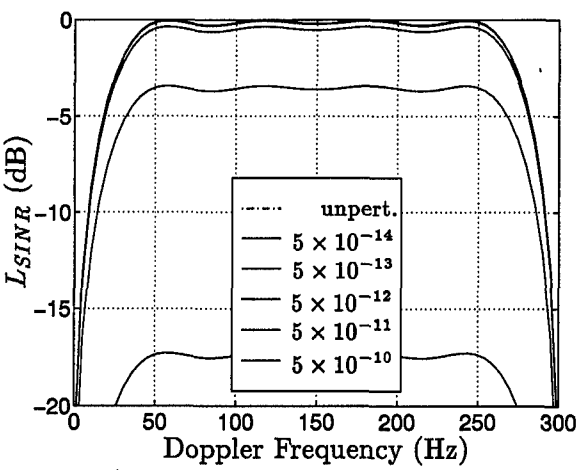

c) $f_0 = 30$ GHz

Figure 5.8 L_{SINR} for JDO under Case I turbulence. Processing performed on 64 antenna elements and 5 pulses.

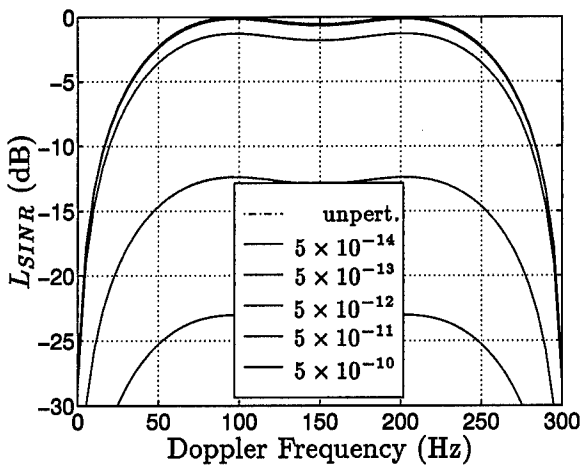

a) $f_0 = 3$ GHz

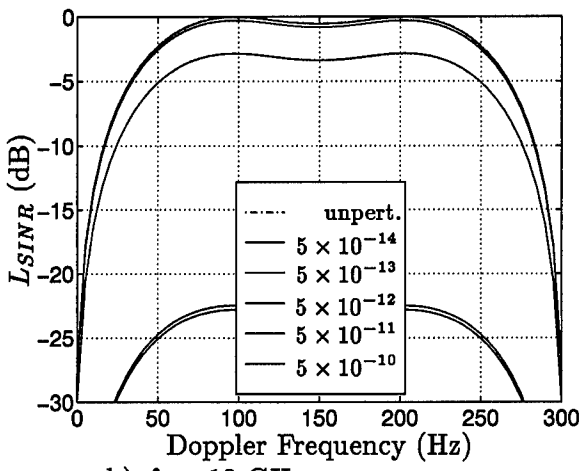

b) $f_0 = 10$ GHz

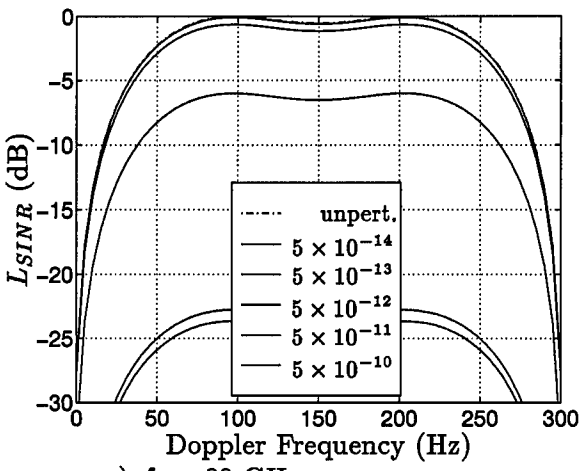

c) $f_0 = 30$ GHz

Figure 5.9 L_{SINR} for JDO under Case I turbulence. Processing performed on 200 antenna elements and 3 pulses.

5.2.5 White Gaussian phase perturbations. The reasoning behind measuring the performance loss for phase perturbations which are spatially uncorrelated and which follow a Gaussian distribution is explained in Sec. 4.5. Some performance losses occur in this case. Figures 5.10a through 5.10c demonstrate the performance losses incurred if the phase perturbations are drawn from uncorrelated Gaussian random variables. The variance of these phase perturbations range from 0.01 to 0.16 rad^2 to approximate the range of variances seen in phase realizations taken from the phase structure function.

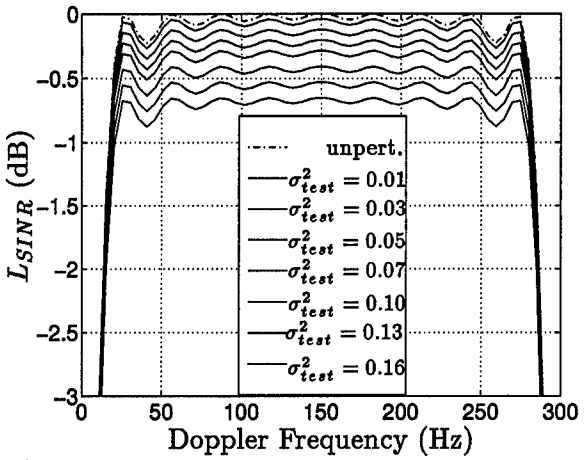

a) 32 antenna elements, 10 pulses

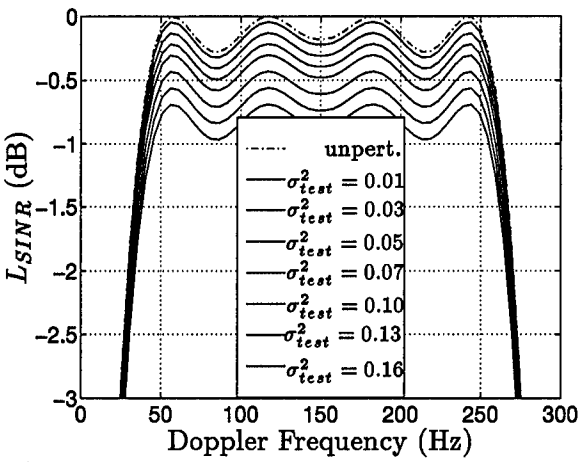

b) 64 antenna elements, 5 pulses

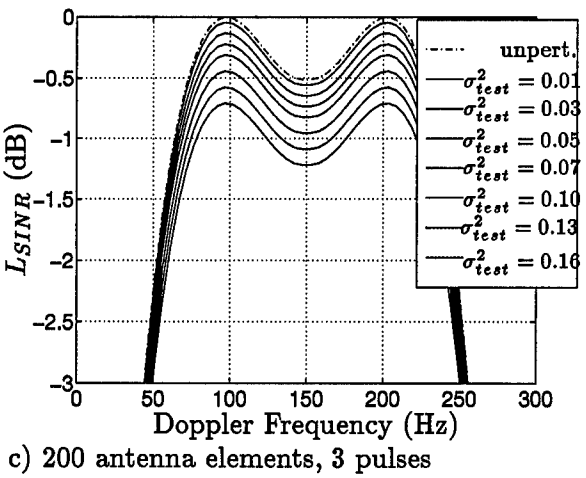

c) 200 antenna elements, 3 pulses

Figure 5.10 L_{SINR} for JDO under case I turbulence simulated by phase perturbations taken from uncorrelated Gaussian random variables having variance σ^2_{test}.

5.2.5.1 Numerical results. Table 5.1 displays the values gathered from the white Gaussian phase perturbation simulations described in this section.

Table 5.1 JDO performance losses with phase perturbations represented by uncorrelated Gaussian random variables. All values are in dB.

no. elements × no. pulses	32 × 10	64 × 5	200 × 3
Variance (rad^2)	(dB)	(dB)	(dB)
$\sigma^2_{test} = 0.01$	-0.0408	-0.0431	-0.0443
$\sigma^2_{test} = 0.03$	-0.1224	-0.1293	-0.1330
$\sigma^2_{test} = 0.05$	-0.2039	-0.2155	-0.2215
$\sigma^2_{test} = 0.07$	-0.2854	-0.3016	-0.3101
$\sigma^2_{test} = 0.10$	-0.4075	-0.4308	-0.4428
$\sigma^2_{test} = 0.13$	-0.5295	-0.5599	-0.5755
$\sigma^2_{test} = 0.16$	-0.6514	-0.6889	-0.7081

The losses attributable to the white Gaussian phase perturbation are clearly dependent on the variance of the Gaussian random variable. However, in these simulations, the length of the antenna array has little effect on the L_{SINR}. Since the phase perturbations are uncorrelated from element to element, the performance loss due to the phase perturbation for a small antenna array is nearly equal to the performance loss for a large array. Since the phases taken from the Gaussian distributed phase perturbation are uncorrelated from element-to-element, the greater propagation distances associated with the larger arrays do not further degrade the performance. So little additional loss is seen in the larger arrays compared to the smaller arrays.

The notch created for clutter nulling at 0 and 300 Hz Doppler is significantly larger in the larger array cases however. This larger notch follows the trend established in the turbulence-induced perturbation simulations. In all simulations, the clutter nulling notch increases as the number of pulses falls. The larger width null is another indication that the minimal number of available pulses affects the Doppler resolution of the STAP system.

A comparison between the performance losses for the Gaussian phase perturbations and the plots for simulated turbulence effects reveals some information about the nature of the turbulence induced phase perturbations. The strongest levels of turbulence, $C_n^2 >$

1×10^{-11} $m^{-2/3}$, surpass the performance losses listed in Table 5.1. This relationship highlights an important property of the turbulence induced phase perturbations.

The turbulence induced phase perturbations have variances which are generally smaller than the σ^2_{test} values used to form the Gaussian perturbation. The variances of the turbulence induced phase perturbations range in size from 5×10^{-6} to 6×10^{-2} rad^2. While the higher values of variance for the turbulence induced phase perturbations are on the order of the first four values listed for σ^2_{test} in Table 5.1, the performance loss in the uncorrelated Gaussian case is noticeable but limited in each of these cases. So, although the turbulence induced phase perturbation may have smaller size and variance than the uncorrelated Gaussian phase perturbations, the actual phase errors resulting from turbulence-induced perturbations lead to larger performance losses.

5.2.6 Wrapup: case I turbulence effects on JDO performance. The data provided in this section shows quantitative effects of Case I turbulence on the performance of the JDO algorithm. These effects are summarized by the quantity L_{SINR}. While these effects are minimal, mainly causing negligible losses for C_n^2 values of greatest interest, there are recognizable trends in this data. As the frequency, C_n^2 value, or array size increases, the SINR loss also increases. Losses of 6 dB are shown for 200 element arrays at 30 GHz and $C_n^2 = 5 \times 10^{-12}$ $m^{-2/3}$. Conditions such as these do occur quite often. These results indicate that turbulence effects should be kept in mind for large, high frequency arrays operating under mild to strong turbulent conditions.

5.3 JDO Performance with Case II Turbulence

In this section the performance of a system using the JDO algorithm in Case II turbulence is examined. In Case II turbulence, both the target signal return and the returns used to form the interference covariance matrix estimate are perturbed by turbulence. Just as in the Case I analysis, the frequencies, C_n^2 values, and antenna sizes listed in Table 4.1 are used to obtain the results given in this section.

5.3.1 Turbulence effects on estimates of $\mathbf{R}_c$. The effects of turbulence on the formation of $\mathbf{R}_c$ are best described in terms of the eigenvalue distribution. Figures 5.11 through 5.13 show the eigenvalue distribution of the perturbed interference covariance matrices ($\mathbf{R}_c'$).

These plots consistently show some distribution of power among eigenvalues due to turbulence effects. The rank of the clutter covariance matrix estimate does not deviate from Brennan's rule but the shift of the values of all the eigenvalues is evident at the higher frequencies. This shift increases with increasing frequency. In addition, the strongest turbulence levels cause the greatest deviance of the eigenvalue distribution from the unperturbed case. These plots show that some change is evident in the structure of the interference covariance matrix estimate. This change is caused by the spatial phase perturbations introduced by atmospheric turbulence.

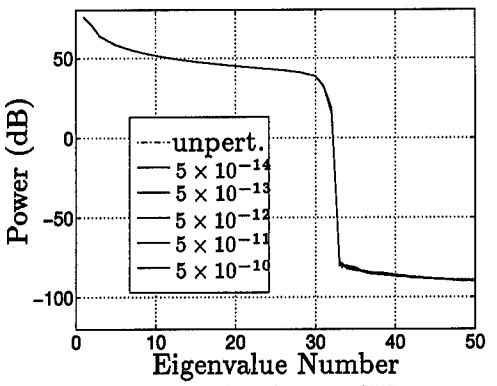

a) interference only for $f_0 = 3$ GHz

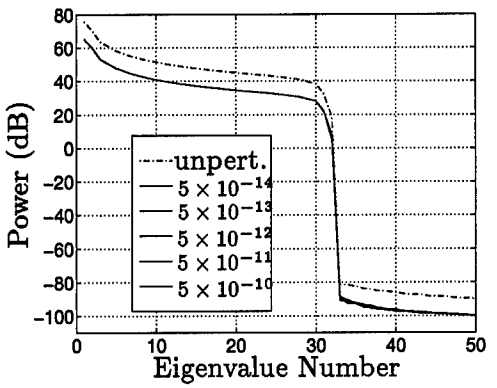

b) interference only for $f_0 = 10$ GHz

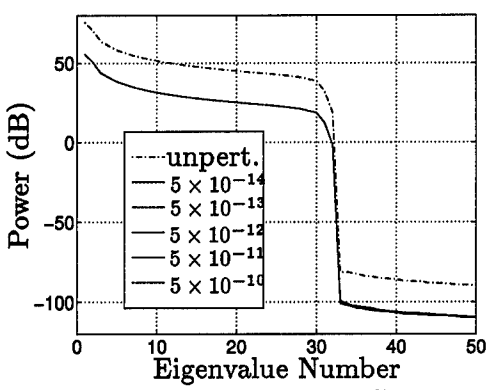

c) interference only for $f_0 = 30$ GHz

Figure 5.11 Eigenvalue distribution plots for $\mathbf{R}_c'$. Covariance matrices formed from signals on 32 antenna elements and 10 pulses. Broken line plot represents eigenvalue distribution of $\mathbf{R}_c$. Solid line plots represent simulation results for C_n^2 values of 5×10^{-14} through 5×10^{-10} $\mathrm{m}^{-2/3}$.

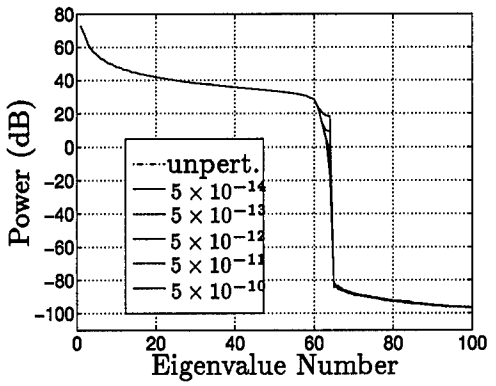

a) interference only for $f_0 = 3$ GHz

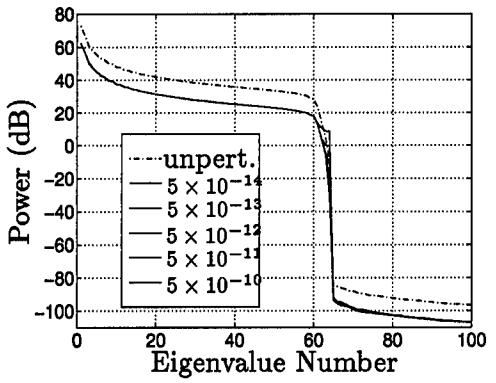

b) interference only for $f_0 = 10$ GHz

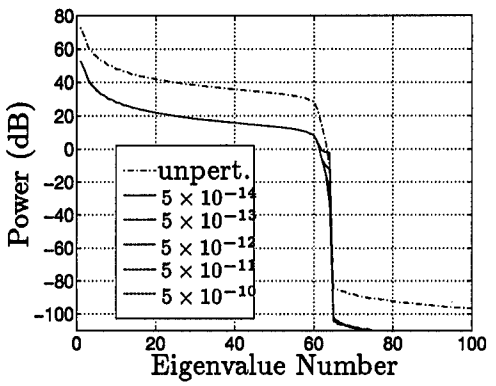

c) interference only for $f_0 = 30$ GHz

Figure 5.12 Eigenvalue distribution plots for $\mathbf{R}_c'$. Covariance matrices formed from signals on 64 antenna elements and 5 pulses. Broken line plot represents eigenvalue distribution of $\mathbf{R}_c$. Solid line plots represent simulation results for C_n^2 values of 5×10^{-14} through 5×10^{-10} $\mathrm{m}^{-2/3}$.

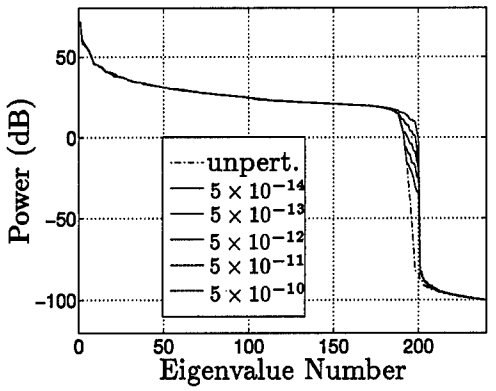

a) interference only for $f_0 = 3$ GHz

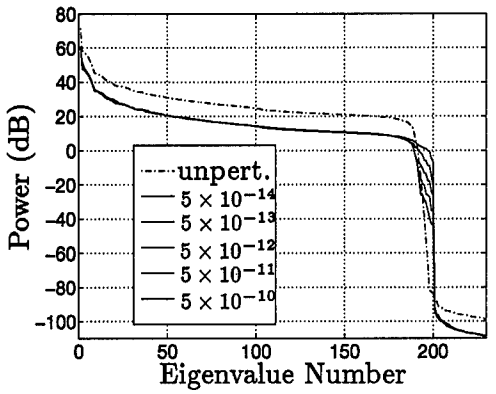

b) interference only for $f_0 = 10$ GHz

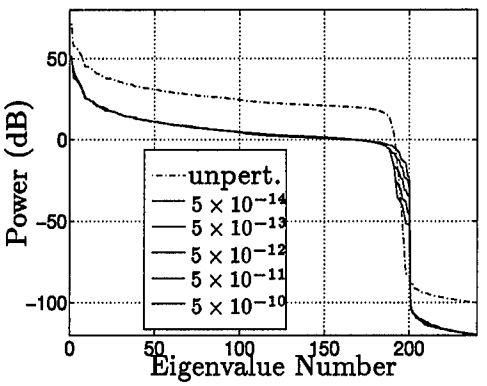

c) interference only for $f_0 = 30$ GHz

Figure 5.13 Eigenvalue distribution plots for $\mathbf{R}'_c$. Covariance matrices formed from signals on 200 antenna elements and 3 pulses. Broken line plot represents eigenvalue distribution of $\mathbf{R}_c$. Solid line plots represent simulation results for C_n^2 values of 5×10^{-14} through 5×10^{-10} $\mathrm{m}^{-2/3}$.

Developing an understanding of the effects of turbulence on the form of $\mathbf{R}_c'$ ensures an even better understanding of the L_{SINR} data for Case II turbulence. The following section examines the Case II turbulence performance loss in L_{SINR} for the various configurations discussed.

5.3.2 32 antenna elements, 10 pulses. This section presents the Case II turbulence performance for antennas using 32 antenna elements, 10 pulses, and the JDO algorithm. The format is similar to the format used to convey the results for JDO Case I turbulence effects in Section 5.2.1 and Fig. 5.7. Figures 5.14a, 5.14b, and 5.14c contain plots relating the performance at 3, 10, and 30 GHz respectively. The plots appearing in Fig. 5.14 are exactly the same as those presented for Case I turbulence in Fig. 5.7. The previous section described the effects of turbulence on the interference covariance matrix estimates in terms of the eigenstructure characteristics. Although some turbulence effect is observed in the characteristics of $\mathbf{R}_c'$, these effects have no perceivable impact on the performance of the system. Since the rank of these covariance matrices have not changed from the unperturbed cases, the lack of impact on Case II performance over Case I is not surprising. The weight vector $\mathbf{w}'$ resulting from the perturbation of the interference covariance estimate does not change appreciable in any of the cases investigated.

5.3.3 64 antenna elements, 5 pulses. Using the same metrics as the previous sections, this section includes L_{SINR} plots produced from simulations of the JDO algorithm applied to Case II turbulence. Figures 5.15a through 5.15c display the L_{SINR} performance for all C_n^2 values of interest at 3, 10, and 30 GHz. Once again, the performance loss is greater over 64 elements than over 32 elements. The same trends with respect to C_n^2 value and frequency are seen here as were seen in the smaller array case. However, there is no difference between the Case II turbulence plots of Fig. 5.15 and the Case I turbulence plots of Fig. 5.8. Once again, the perturbation of the interference has no perceivable affect.

5.3.4 200 antenna elements, 3 pulses. This section contains the simulation results for 200 antenna elements. The format is the same as that seen in previous sections. Figures

5.16a through 5.16c include L_{SINR} plots for JDO performance under Case II turbulence at 3, 10, and 30 GHz. All C_n^2 values of interest are considered.

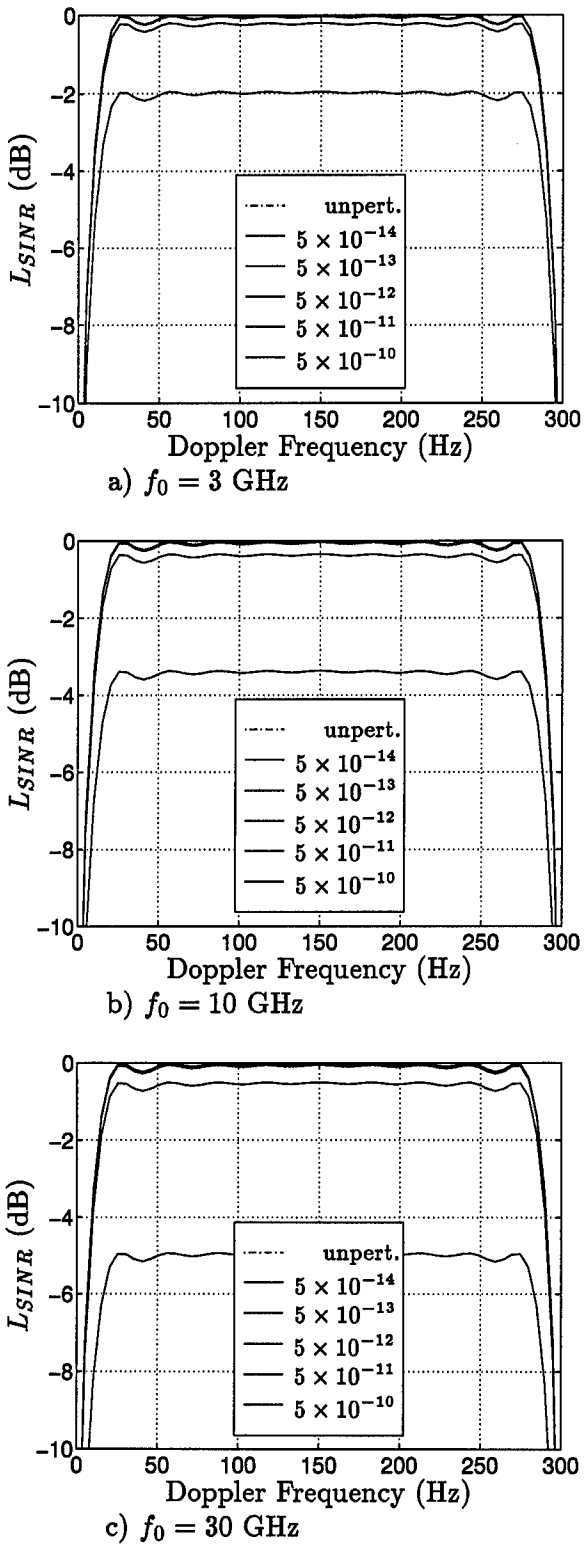

Figure 5.14 L_{SINR} plots for JDO under case II turbulence. Processing performed on 32 antenna elements and 10 pulses.

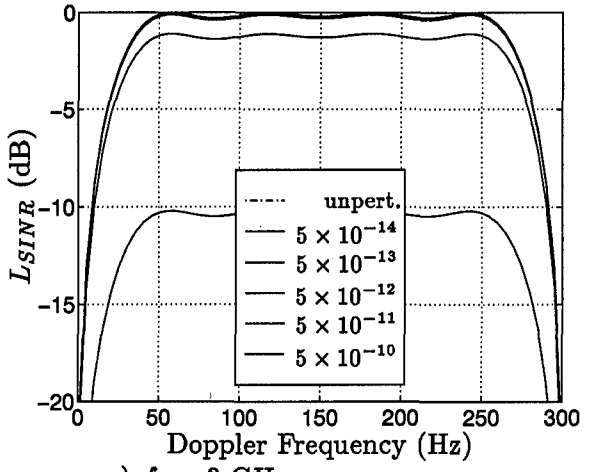

a) $f_0 = 3$ GHz

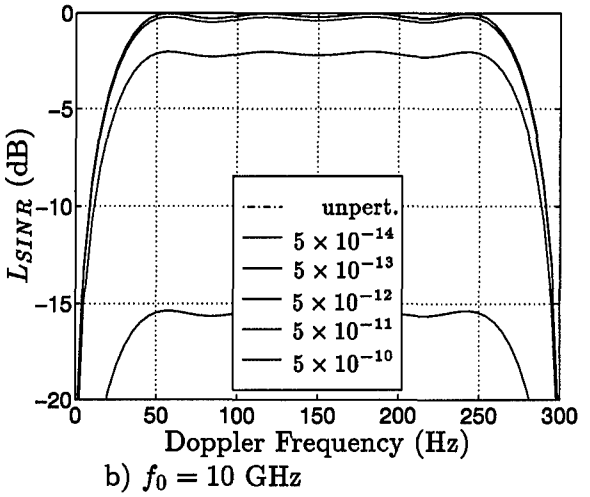

b) $f_0 = 10$ GHz

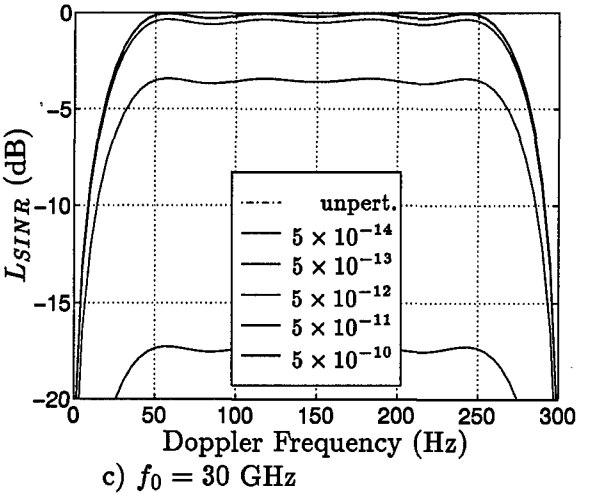

c) $f_0 = 30$ GHz

Figure 5.15 L_{SINR} for JDO under case II turbulence. Processing performed on 64 antenna elements and 5 pulses.

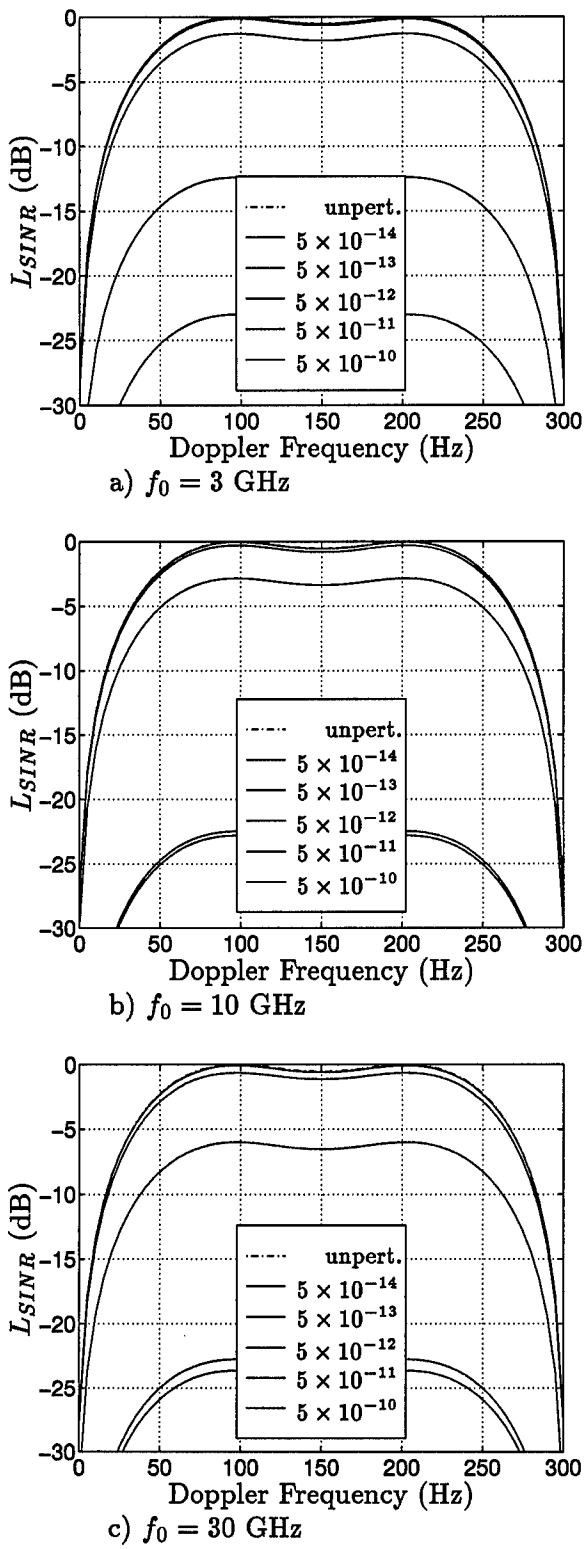

Figure 5.16 L_{SINR} for JDO under case II turbulence. Processing performed on 200 antenna elements and 3 pulses.

Again, the loss is greater over 200 antenna elements than over smaller arrays. Performance losses also increase with increasing frequency or increasing C_n^2. Once again, the Case II turbulence effects are no different than in Case I.

The following section contains results from simulations under which atmospheric turbulence induced performance losses in FTS processing are measured.

5.4 Factored Time-Space (FTS) Baseline Performance

Just as standards exists for measuring performance losses in JDO algorithms, separate standards exist for the FTS algorithm. This section contains plots which represent these standards for comparison. These standards are known as L_{SINR} baseline performance for FTS. The plots denoting baseline performance are shown in Figs. 5.17 through 5.20. Only the 32 element $\times$ 10 pulse geometry is considered here since the other geometries do not include enough pulses to ensure reliable FTS performance. Figure 5.17 provides a large scale perspective of the L_{SINR} for unperturbed FTS performance and Fig. 5.18 depicts the same plot in the range of L_{SINR} values of interest. The additional 1 dB

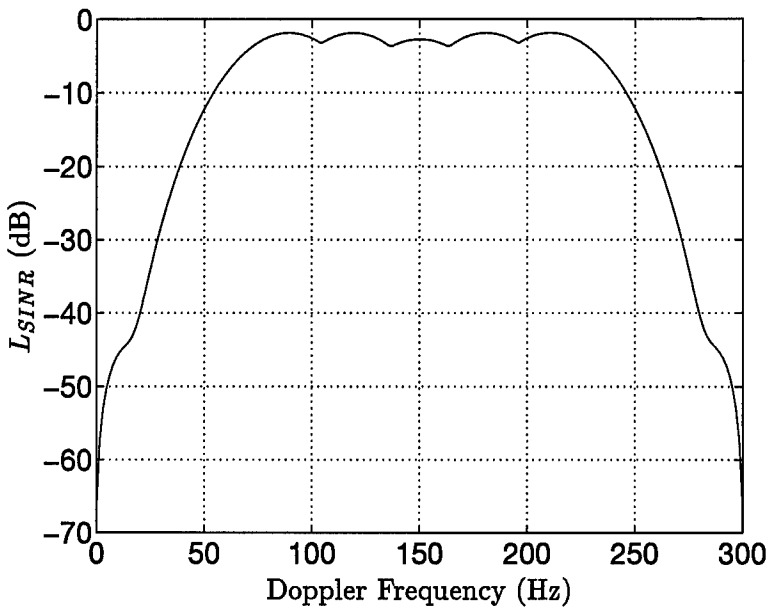

Figure 5.17 Baseline L_{SINR} for FTS. Processing performed on 32 antenna elements and 10 pulses.

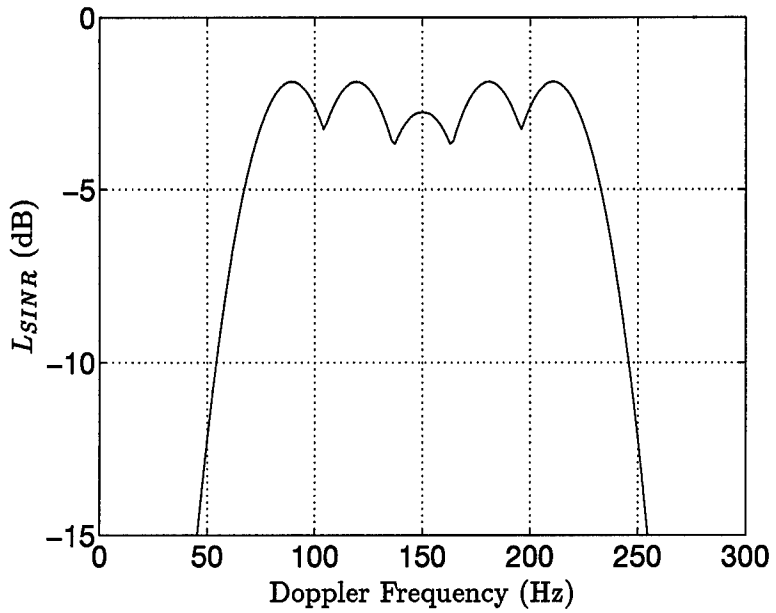

Figure 5.18 Baseline L_{SINR} for FTS (zoomed). Processing performed on 32 antenna elements and 10 pulses.

drop in the L_{SINR} at 150 Hz Doppler in Fig. 5.17 is probably due to the impact of the 80 dB Doppler taper at that frequency. Ward [17] states that a heavy Doppler sidelobe taper is central to the success of FTS. When applying such a taper to the Doppler filters, the frequency least impacted by the taper will be the frequency at 1/2 the pulse repetition frequency (PRF). Without the focus provided by this Doppler taper, heavy performance losses become apparent.

Notice that none of the plots achieve 0 dB performance. Since FTS is a partially-adaptive method, performance on par with JDO is not possible. In addition, the performance of the FTS algorithm for 200 elements × 3 pulses or 64 elements × 5 pulses is very poor. Ward [17] also points out that reliable FTS processing requires many degrees of freedom in both space and time. Clearly, the 3 or 5 pulses used in these simulations is not adequate to meet the Doppler resolution requirements of FTS. The next section presents a discussion about the need for an adequate temporal dimension for FTS processing.

5.4.1 Performance in FTS processing with turbulence perturbations. It is also evident that FTS performance is related to the sizes of N and M. The L_{SINR} for simulations

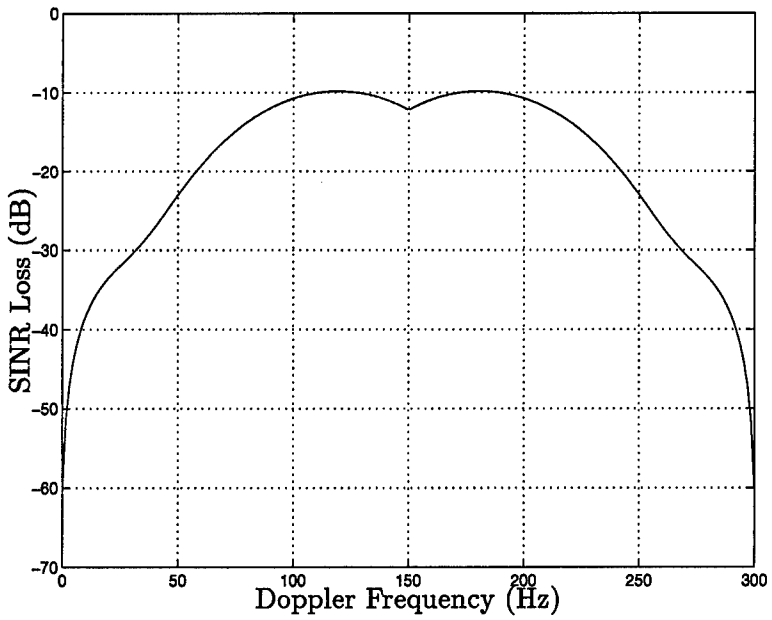

Figure 5.19 Optimal L_{SINR} for FTS. Processing performed on 64 antenna elements and 5 pulses.

with $N = 32$ is higher than for those simulations with $N = 64$. Similarly, the performance of $N = 64$ systems surpasses that of $N = 200$ systems. The key behind these performance levels is not in the size of N but in the size of M. The FTS algorithm employs Doppler filtering prior to adaptation. The number of Doppler filters, hence the resolution of the algorithm in the Doppler space, is defined by the size of M. A larger M denotes much finer Doppler resolution than a smaller M. Figures 5.21 and 5.22 depict the untapered Doppler filters in the Doppler space for two different values of M. Figure 5.21a represents an FTS Doppler filter bank with $M = 3$ pulses defining the Doppler resolution, such as that found in the $N = 200$ element simulations. Here, the Doppler space is divided into three portions and Fig. 5.21a depicts the shape of the L_{SINR} plots presented for the $N = 200$ simulations in Fig. 5.20. Figure 5.21b highlights the same three-component Doppler filter bank but in this plot, the output of the first filter is neglected as in the case of nulling for the 0 Hz Doppler clutter. In FTS processing, the m^{th} composite weight vector $\mathbf{w}_m$ is formed from

$$\mathbf{w}_m = \mathbf{T}_m \mathbf{T}_m^H \hat{\mathbf{R}}_u \mathbf{T}_m \tilde{\mathbf{g}}_s$$

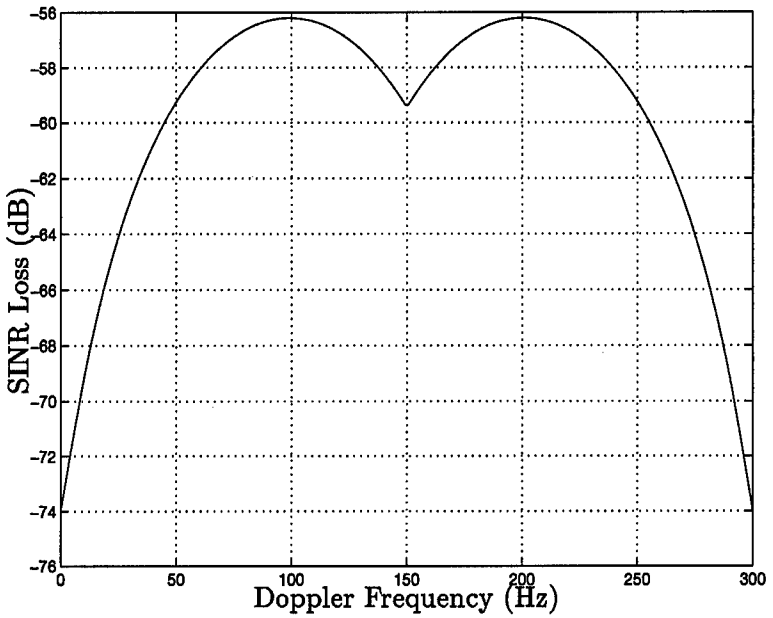

Figure 5.20 Optimal L_{SINR} for FTS. Processing performed on 200 antenna elements and 3 pulses.

as shown in Eqn. (2.90). The estimate of the interference-plus-noise covariance matrix $\hat{\mathbf{R}}_u$ is projected to a lower dimension space by

$$\mathbf{T}_m = (\mathbf{f}_m \otimes \mathbf{I}_N).$$

The m^{th} Doppler filter is given by $\mathbf{f}_m$. Forming the vector $\mathbf{w}_m$ precisely to steer the beam and nulls is more difficult when M is small. The effect of having coarse Doppler resolution among the Doppler filters is that the resulting $\mathbf{w}_m$ causes some nulling across the entire Doppler space in order to achieve the deep nulling at 0 Hz Doppler. Consequently, the overall performance of the $N = 200$ element algorithm is poor and implementations with more pulses exhibit better performance. To highlight the better flexibility available with a larger M, Fig. 5.22 depicts the filter bank used when $M = 10$. Figure 5.22a shows the full set of Doppler filters and Figure 5.22b shows the gap left in the space when clutter nulling occurs. The size of the 0 Hz gap caused by the nulling is reduced while the improved resolution of the filter promotes higher L_{SINR} values.

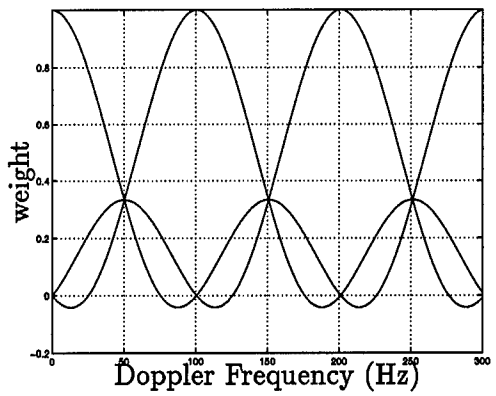

a) Doppler filters spanning the full Doppler space

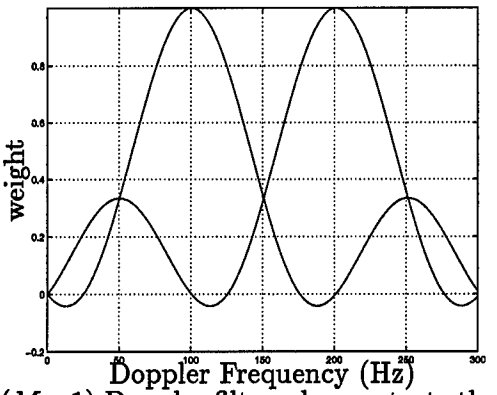

b) $(M-1)$ Doppler filters demonstrate the effect on low frequency performance of adaptive nulling with poor Doppler resolution.

Figure 5.21 Doppler filter passbands plotted in the Doppler space divided among 3 filters. These plots highlight the poor resolution in Doppler afforded by FTS algorithms using only 3 pulses.

The next two sections contain the results and analysis of simulations designed to examine the effects of Case I and Case II turbulence on FTS processing.

5.5 FTS Performance with Case I Turbulence

Section 5.2 contains data and explanations about the effects of Case I turbulence on JDO processing. The data consists of L_{SINR} values which represent the loss in performance due to the turbulence effects. This section uses a similar approach to examine Case I turbulence effects on the FTS processing algorithm. The baseline values for FTS processing presented in Sec. 5.4 are used here as a standard for comparison. Each element-pulse combination is considered seperately in the following sections.

5.5.1 32 antenna elements, 10 pulses. The degradation in the L_{SINR} due to case I turbulence effects are shown in Fig. 5.7. The plots show a minimal effect at all frequencies and all but the strongest turbulence simulations. There is an increase in the L_{SINR} evident at the center of the Doppler space for the higher frequencies. This increase is probably due, once again, to the effects of the Doppler taper. Generally, performance losses are on par with those seen under JDO processing methods. Similarly, increased turbulence perturbation effects are seen at higher operating frequencies.

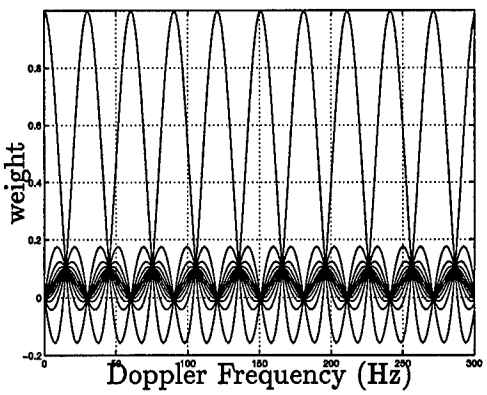

a) Doppler filters spanning the full Doppler space

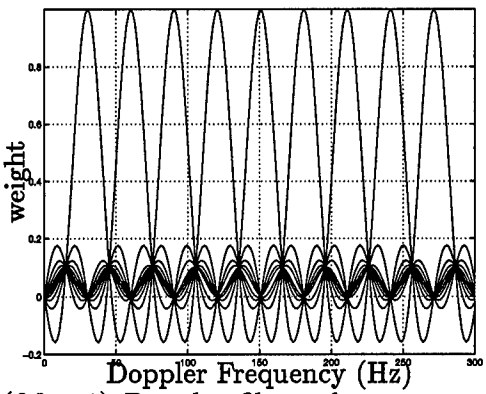

b) $(M-1)$ Doppler filters demonstrate the improvement in low frequency performance of adaptive nulling with finer Doppler resolution.

Figure 5.22 Doppler filter passbands plotted in the Doppler space divided among 10 filters. These plots demonstrate the improvement in Doppler resolution resulting from FTS algorithms using as many as 10 pulses.

The next section examines the FTS performance consequences of operating in a Case II turbulence environment.

5.6 FTS Performance with Case II Turbulence

Just as in the JDO simulations, the performance results for FTS processing under Case II turbulence are the same as those presented for the Case I turbulence simulations. The additional effect due to the perturbation of the weight vector through perturbations of the interference covariance estimates has a negligible effect on the results already presented in the previous section. Under Case II turbulence effects, the changes in the weight vector from Case I are probably insignificant.

The FTS performance under Case II turbulence is summarized by the L_{SINR} plots in Figure 5.24. The plots shown in these figures confirm that there is little change between Case I turbulence and Case II turbulence effects for $N = 32$ elements. For the strongest turbulence simulation, there is an increased effect for Case II turbulence over Case I turbulence at the highest frequency. Because this change only appears in the strongest turbulence simulation (an unrealistic strength of turbulence) it is difficult to draw general conclusions from this result.

5.7 Summary

The effects of atmospheric turbulence on STAP performance are presented in this chapter. The results presented include effects at different frequencies and turbulence C_n^2 values on three different STAP geometries. Both JDO and FTS performance is examined in this chapter.

Case II turbulence effects in $\mathbf{R}_c'$ are evident in the matrices' eigenvalues.. With increasing frequency and C_n^2 values, the energy in the matrices appears more distributed among the eigenvalues. This eigenvalue spreading with increased turbulence is evident in the eigenspectra plots of all the simulations.

The results show that JDO performance is affected by turbulence but the effect is minimal under realistic turbulence environments. The observed effects are greater with increasing frequency, C_n^2 value, and array size but no significant additional degradation is seen in Case II effects over Case I. Simulations using Gaussian distributed phase perturbations show similar results but on a smaller scale.

FTS performance is similar to that seen for JDO. Case I and Case II effects on FTS performance are virtually similar.

Overall, turbulence effects on STAP performance are minimal for typical turbulence strengths at radar frequencies. However, turbulence effects may become significant for large enough arrays at higher frequencies.

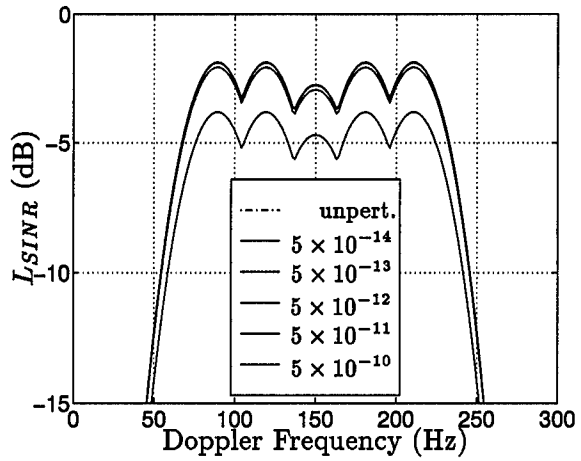

a) $f_0 = 3$ GHz

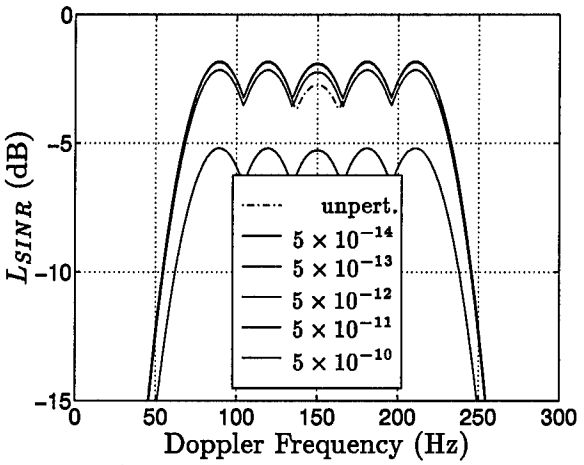

b) $f_0 = 10$ GHz

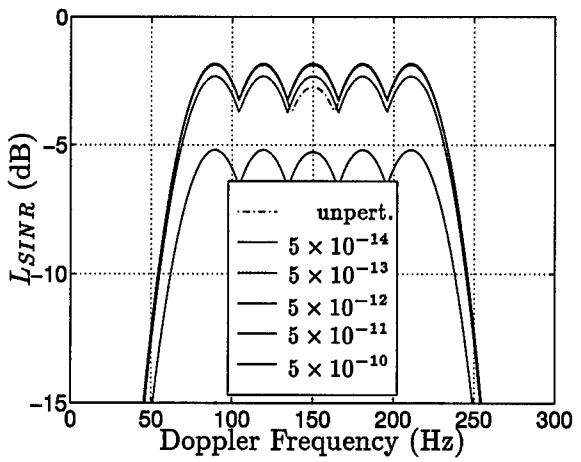

c) $f_0 = 30$ GHz

Figure 5.23 L_{SINR} plots for FTS under Case I turbulence. Processing performed on 32 antenna elements and 10 pulses.

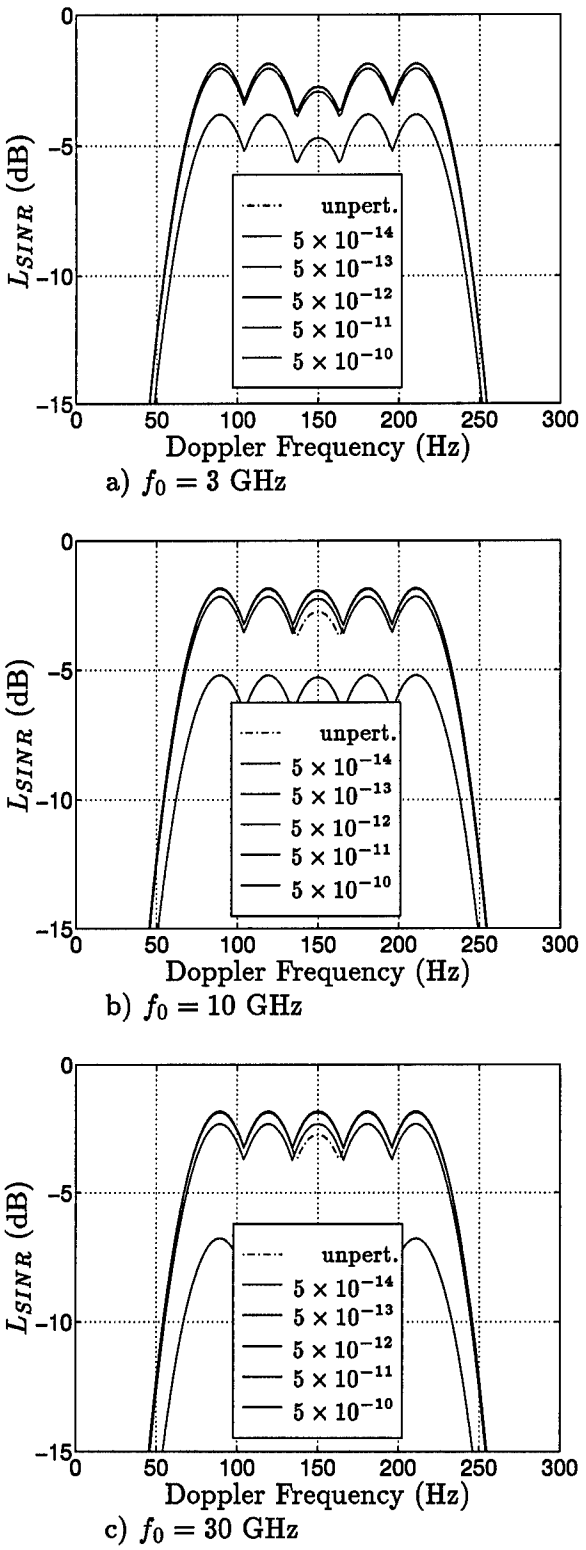

Figure 5.24 L_{SINR} plots for FTS under Case II turbulence. Processing performed on 32 antenna elements and 10 pulses.

VI. Conclusions and Recommendations

In this thesis, the effects of atmospheric turbulence on a ground-based, linear antenna array using Space-Time Adaptive Processing (STAP) are studied. Due to the spectrum of interest (3 to 30 GHz), these effects are restricted to phase perturbations in reference to the spatial dimension. Effects on Fully Adaptive STAP or Joint Domain Optimum (JDO) and Factored Time-Space (FTS) STAP methods are investigated for arrays of size 32, 64, and 200 antenna elements operating in an evironment having one target and clutter interference.

6.1 Summary of Procedure

The index of refraction structure constant (C_n^2) quantitatively describes the strength of the turbulence and is used to develop the phase structure function ($D_S(\boldsymbol{\rho})$) in terms of the distance in space $\boldsymbol{\rho} = \vec{r}' - \vec{r}$. The statistics of the spatial phase variations due to turbulence, summarized in $D_S(\boldsymbol{\rho})$, are used to develop realizations of the phase errors on the elements of the antenna array. The spatial phase perturbation statistics may also be re-oriented into a covariance matrix to modify the clutter covariance matrix ($\mathbf{R}_c$) for the turbulence effects. These phase error realizations and perturbed clutter covariance matrices ($\mathbf{R}_c'$) may be used in Monte Carlo simulation to form the signal-to-interference-plus-noise-ratio (SINR) and subsequently the SINR loss (L_{SINR}).

6.2 Results

6.2.1 JDO performance. In this thesis, the effects of atmospheric turbulence of typical strengths (C_n^2: 10^{-14} to 10^{-12} $\mathrm{m}^{-2/3}$) yield unremarkable losses for all but the highest frequencies and largest arrays. Generally, although the effects are negligible for radar frequencies, performance losses due to atmospheric turbulence effects increase with

- increasing array size
- increasing frequency
- increasing C_n^2 value.

This trend in performance loss may yield significant losses in the right combination of STAP characteristics. For JDO STAP systems operating at 30 GHz with 200 antenna elements, SINR losses of -6 dB are measured for $C_n^2 = 5 \times 10^{-12}$ m$^{-2/3}$. In this particular case, a significant loss occurs under vary common strength turbulence.

6.2.2 FTS performance. Performance losses for FTS are measured for small antenna arrays only and these losses are on a similar scale to JDO performance losses. Therefore, FTS processing may be used for its computational advantage with no disadvantage in terms of turbulence effects.

6.2.3 Case I turbulence vs. Case II turbulence. Examination of two different forms of turbulence effect are summarized as Case I turbulence and Case II turbulence. Case I involves turbulence-induced phase perturbations on the target signal return while the the interference covariance is known. Case II involves a perturbation of the target signal return as well as perturbations disrupting the system estimate of the interference covariance matrix. Both Case I and Case II yield similar losses for JDO and FTS. From this, it may be assumed that the interference may be confidently estimated by sampling within a turbulent environment without any serious consequence in performance.

6.3 Recommendations for Future Work

This thesis turns up some significant performance consequences for operating at higher frequencies and/or with larger arrays in a turbulent environment. It would prove useful to further examine the effects at frequencies higher than 30 GHz and arrays larger than 200 antenna elements.

At the frequencies used in this study, turbulence-induced temporal phase perturbations are of insignificant magnitude and frequency. Studies investigating higher frequencies may not necessarily make the same assumption. In addition, some temporal effect is introduced by movement of turbulent eddies by wind velocity. Taylor's Frozen Flow hypothesis may be used to approximate these wind effects and to quantify the effect on STAP performance.

This study, for the purposes of focusing on the atmospheric turbulence effects, considered clutter interferers only. Research examining the effects of turbulence on nulling of jammers would prove most useful to the STAP community.

The FTS results presented in this thesis only touch the tip of the research needed to understand turbulence effects. There are many other Partially Adaptive STAP methods which may be significantly affected by atmospheric turbulence effects. This may become more evident if any sort of turbulence-induced temporal phase perturbations are also introduced.

McMillan [12] alludes to a STAP version of the Beacon Guide Star adaptive method. This method, already used in adaptive optics, combats atmospheric turbulence effects by shifting the weights on the antenna adaptively to counter turbulence effects. The Case II turbulence development and results provide a good lead into the possibility of using a clutter beacon as a model for developing the turbulence-countering adaptive weights. Some difficulties will occur in applying this technique because STAP is a method anchored in using statistics and statistical quantities while the Beacon Guide Star concept involves sampling and compensation of individual instances of turbulence.

Appendix A. Transforming a matrix into one that is positive definite

If the matrix $\mathbf{A}$ is not positive definite then the relationship

$$\mathbf{x}^H\mathbf{A}\mathbf{x} > 0 \tag{A.1}$$

does not hold true for some $\mathbf{x}$. Instead, for this $\mathbf{x}$, the relationship is

$$\mathbf{x}^H\mathbf{A}\mathbf{x} = h, \tag{A.2}$$

where $h \leq 0$. Shifting the inner product by h along the number line yields

$$\mathbf{x}^H\mathbf{A}\mathbf{x} + h > 0. \tag{A.3}$$

If h is replaced by $g\mathbf{x}^H\mathbf{x}$, the test for positive definiteness may be rewritten as

$$\begin{aligned} \mathbf{x}^H\mathbf{A}\mathbf{x} + g\mathbf{x}^H\mathbf{x} &> 0 \\ \mathbf{x}^H\mathbf{A}\mathbf{x} + \mathbf{x}^H g\mathbf{x} &> 0 \\ \mathbf{x}^H(\mathbf{A}\mathbf{x} + g\mathbf{x}) &> 0 \end{aligned} \tag{A.4}$$

If g and $\mathbf{x}$ are eigenvalue-eigenvector pairs such that $g = -\lambda_{\mathbf{A}_i}$ and $\mathbf{x} = \mathbf{v}_{\mathbf{A}_i}$ then a threshold is met. This threshold is described by

$$\mathbf{x}^H(\mathbf{A}\mathbf{x} + g\mathbf{x}) = \mathbf{v}_{\mathbf{A}_i}^H(\mathbf{A}\mathbf{v}_{\mathbf{A}_i} - \lambda_{\mathbf{A}_i}\mathbf{v}_{\mathbf{A}_i}) \tag{A.5}$$

$$= \mathbf{v}_{\mathbf{A}_i}^H\mathbf{0} \tag{A.6}$$

$$= 0. \tag{A.7}$$

Here, $\lambda_{\mathbf{A}_i}$ is the i^{th} eigenvalue of $\mathbf{A}$ and $\mathbf{v}_{\mathbf{A}_i}$ is the corresponding eigenvector. Since the eigenvalue-eigenvector relationship is

$$\mathbf{A}\mathbf{v}_{\mathbf{A}_i} = \lambda_{\mathbf{A}_i}\mathbf{v}_{\mathbf{A}_i}, \tag{A.8}$$

then the relationship may be rewritten to form

$$\mathbf{A}\mathbf{v}_{\mathbf{A}_i} - \lambda_{\mathbf{A}_i}\mathbf{v}_{\mathbf{A}_i} = 0. \tag{A.9}$$

So, a matrix which is not positive definite, but is theoretically meant to be, may be transformed into one that is positive definite. This transformation involves subtracting a diagonal matrix whose elements are formed from a significant negative eigenvalue from $\mathbf{A}$. The transformation produces a positive definite matrix given by

$$\begin{aligned} \mathbf{B} &= \mathbf{A} - \lambda_{\mathbf{A}_i}\mathbf{I} \\ &= \mathbf{A} + g\mathbf{I}. \end{aligned} \tag{A.10}$$

Now, the resulting matrix $\mathbf{B}$ has the same form as $\mathbf{A}$ and meets the criteria for being positive definite

$$\mathbf{x}^H\mathbf{B}\mathbf{x} = \mathbf{x}^H(\mathbf{A} + g\mathbf{I})\mathbf{x} \tag{A.11}$$

$$> 0. \tag{A.12}$$

Bibliography

1. Balanis, Constantine A. *Antenna Theory: Analysis and Design*. New York, NY: John Wiley & Sons, Inc., 1997.
2. Blake, Bernard, editor. *Jane's Weapon Systems, Nineteenth Edition*. Coulsdon, UK: Jane's Information Group, 1988.
3. Clifford, Steven F. and Richard J. Lataitis. "Mutual Coherence Function for Line-of-Sight Microwave Propagation Through Atmospheric Turbulence," *Radio Science*, *20*(11):221–227 (March-April 1985).
4. Clifford, Steven F. and John W. Strohbehn. "The Theory of Microwave Line-of-Sight Propagation Through a Turbulent Atmosphere," *IEEE Transactions on Antennas and Propagation*, *18*(2):264–274 (March 1970).
5. Dudgeon, Dan E. and Russell M. Mersereau. *Multidimensional Digital Signal Processing*. Englewood Cliffs, NJ: Prentice-Hall, Inc., 1984.
6. Fante, Ronald L. "Electromagnetic Beam Propagation in Turbulent Media," *Proceedings of the IEEE*, *63*(12):1669–1692 (December 1975).
7. Fante, Ronald L. "Electromagnetic Beam Propagation in Turbulent Media: An Update," *Proceedings of the IEEE*, *69*(11):1424–1443 (November 1980).
8. Hill, R. J. and S. F. Clifford. "Contribution of Water Vapor Monomer Resonances to Fluctuations of Refraction and Absorption for Submillimeter Through Centimeter Wavelengths," *Radio Science*, *16*(1):77–82 (January-February 1981).
9. Hill, R. J., et al. *Computed Refraction and Abosorption Fluctuations Caused By Temperature, Humidity, and Pressure Fluctuations - Radio Waves to 5 μm.* Technical Report ERL WPL-59, National Oceanic and Atmospheric Administration, June 1980.
10. Hill, R. J., et al. "Refractive-Index and Absorption Fluctuations in the Infrared Caused by Temperature, Humidity, and Pressure Fluctuations," *Journal of the Optical Society of America*, *70*(10):1192–1205 (October 1980).
11. Hill, Reginald J., et al. "Turbulence-Induced Millimeter-Wave Scintillation Compared with Micrometeorological Measurements," *IEEE Transactions on Geoscience and Remote Sensing*, *26*(3):330–342 (May 1988).
12. McMillan, R. W., et al. "Millimeter-Wave Atmospheric Turbulence Measurements: Instrumentation, Selected Results, and System Effects," *International Journal of Infrared and Millimete Waves*, *18*(1) (January 1997).
13. McMillan, R. W., et al. "Millimeter Wave Atmospheric Turbulence Measurements: Preliminary Results." *Proceedings of the SPIE: Millimeter Wave Technology337*. 1982.
14. Roggemann, Michael C. and Byron Welsh. *Imaging Through Turbulence*. Boca Raton, FL: CRC Press, 1996.
15. Skolnik, Merrill I. *Introduction to Radar Systems*. New York, NY: McGraw-Hill, Inc., 1980.

16. Strohbehn, John W. "Line-of-Sight Wave Propagation Through the Turbulent Atmosphere," *Proceedings of the IEEE*, *56*(8):1301–1318 (August 1968).

17. Ward, J. *Space-Time Adaptive Processing for Airborne Radar*. Technical Report 1015, Ft. Belvoir, VA: Lincoln Laboratory, Massachusetts Institute of Technology, December 1994.

18. Welsh, Byron M. "A Fourier Series Based Atmospheric Phase Screen Generator for Simulating Anisoplanatic Geometrics and Temporal Evolution." *Proceedings of the SPIE: Propagation and Imaging through the Atmosphere3125*. July 1997.

Vita

Second Lieutenant Vinod D. Naga was born on 3 August 1974 in Oak Lawn, Illinois. After graduating from Okemos High School of Okemos, Michigan in 1992, he entered the College of Engineering at the Illinois Insitute of Technology in Chicago, Illinois. He graduated with a Bachelor of Science degree in Electrical Engineering in May of 1996. Having completed the Air Force Reserve Officer Training Corps program at the Illinois Institute of Technology, he also received received his commission in May of 1996.

Lieutenant Naga's first assignment was to Wright-Patterson AFB in Dayton, Ohio. There he entered the Department of Electrical Engineering at the Air Force Institute of Technology. At the Air Force Institute of Technology, he began study towards a Master of Science degree in Electrical Engineering.

Permanent address: 4595 Comanche Dr.
Okemos, MI 48864

REPORT DOCUMENTATION PAGE

Form Approved
OMB No. 0704-0188

1. AGENCY USE ONLY *(Leave blank)*	2. REPORT DATE	3. REPORT TYPE AND DATES COVERED
	December 1997	Master's Thesis

4. TITLE AND SUBTITLE
ATMOSPHERIC INDUCED ERRORS IN SPACE-TIME ADAPTIVE PROCESSING

5. FUNDING NUMBERS

6. AUTHOR(S)
Vinod D. Naga, 2LT, USAF

7. PERFORMING ORGANIZATION NAME(S) AND ADDRESS(ES)
Air Force Institute of Technology
2750 P Street
WPAFB OH 45433-7765

8. PERFORMING ORGANIZATION REPORT NUMBER
AFIT/GE/ENG/97D-09

9. SPONSORING/MONITORING AGENCY NAME(S) AND ADDRESS(ES)
Robert W. McMillan
Surveillance and Photonics Directorate
Rome Laboratory
26 Electronic Parkway
Rome, NY 13441-4514

10. SPONSORING/MONITORING AGENCY REPORT NUMBER

11. SUPPLEMENTARY NOTES

12a. DISTRIBUTION AVAILABILITY STATEMENT
Distribution Unlimited

12b. DISTRIBUTION CODE

13. ABSTRACT *(Maximum 200 words)*

This thesis examines the effects of atmospheric turbulence-induced phase perturbations on the performance of ground-based Space-Time Adaptive Processing (STAP) systems. Both Fully Adaptive Joint Domain Optimum and Partially Adaptive Factored-Time Space processing methods are examined.

This thesis concentrates on the turbulence effects on STAP applied to ground-based arrays. This thesis further focuses on the capability of STAP to resolve targets at low elevation angles in the presence of turbulence. Only clutter interference and receiver noise are considered. Turbulence effects on the EM phase-front are calculated for turbulence strength C_n^2 values ranging from 5.0×10^{-14} $m^{-2/3}$ to 5.0×10^{-10} $m^{-2/3}$ in the S, X, and Ka frequency bands. The analysis is carried out for array lengths of 32, 64, and 200 antenna elements at each frequency. The performance losses are summarized in terms of the signal-to-interference-plus-noise ratio (SINR) and the SINR Loss (L_{SINR}).

Fully adaptive performance losses due to atmospheric turbulence are less than 1 dB for typical turbulence strengths. The 200 element array faces a 6 dB performance loss at 30 GHz under turbulence of $C_n^2 = 5 \times 10^{-12}$ $m^{-2/3}$. Similar losses are recorded for Factored Time-Space and for all experiments where sampling of the interference through turbulence is simulated.

14. SUBJECT TERMS	15. NUMBER OF PAGES
radar, STAP, atmospheric turbulence, adaptive processing, array antenna	137
	16. PRICE CODE

17. SECURITY CLASSIFICATION OF REPORT	18. SECURITY CLASSIFICATION OF THIS PAGE	19. SECURITY CLASSIFICATION OF ABSTRACT	20. LIMITATION OF ABSTRACT
UNCLASSIFIED	UNCLASSIFIED	UNCLASSIFIED	UL